QATAR UNIVERSITY

COLLEGE OF ENGINEERING

TOWARDS AN EFFICIENT HEALTH CONDITION MONITORING STRATEGY APPLIED FOR GEARING MECHANICAL SYSTEMS

BY

OMRAN KHALDOUN MOHAMED YAQUB ISMAIL ABDALLAH

A Thesis Submitted to
the College of Engineering
in Partial Fulfillment of the Requirements for the Degree of
Master of Science in Mechanical Engineering

January 2023

COMMITTEE PAGE

The members of the Committee approve the Thesis of
Omran Abdallah defended on 28/12/2022.

Prof. Sadok Sassi
Thesis/Dissertation Supervisor

Prof. Asan Abdul Muthalif
Committee Member

Dr. Jamil Renno
Committee Member

Dr. Hassen Ouakad
Committee Member

Approved:

Khalid Kamal Naji, Dean, College of Engineering

ABSTRACT

ABDALLAH, OMRAN, K, Masters: January : 2023,
Masters of Science in Mechanical Engineering
Title: Towards an Efficient Health Condition Monitoring Strategy Applied for Gearing Mechanical Systems
Supervisor of Thesis: Sadok Sassi.

Cracked teeth are a common phenomenon for gears. The dynamic behavior of gears in the presence of cracks and poor lubrication conditions that lead to rubbing between teeth are not well understood, which limits the development of precision and reliability of gear transmission. In this research, a comprehensive model is proposed to study the dynamic behavior of a one-stage spur gearbox with cracked teeth in a condition of poor lubrication. The inter-teeth rubbing generated from the sliding of one surface relative to another is caused by the variation of curvature radii of both mating teeth when the contact point is moving along the line of contact. Under the transmitted loading between mating teeth, the common elastic deformed area, computed by Hertz theory, keeps varying, generating a combination of modulated and constant amplitudes noises. Adding this friction-induced vibration to the impulsive periodic response is found to realistically mimic the actual behavior experimentally measured on a test rig specially developed for this investigation. Based on time-domain statistical indicators, the study concluded that the combination of both components of friction-induced noise with the primary impacting response was found to accurately and realistically simulate the dynamic behavior of the gearbox. Afterward, the experimental setup utilized in this investigation was modeled numerically in the initial part of the research to get a variety of operating circumstances. Those results are included in the dataset used in this work.

Getting an adequate generalization capability by training traditional, deep 2-dimensional (2D) CNNs is a time-consuming operation, and this often requires massive datasets, exponentially increasing the processing challenges. Conversely, 1D CNNs have been suggested for use in various 1D signal processing tasks, such as gear condition monitoring. Recently developed methods aim to eliminate these drawbacks by focusing just on 1D signals, where they perform much better.

This research addresses the challenge of failure identification in gears. It provides a solution based on combining raw and residual vibration data with a convolutional neural network (CNN) and recurrent neural network (LSTM). The described technique begins by training a one-dimensional convolutional neural network (CNN) using the raw vibration signals and then a long short-term memory (LSTM) network with the remaining vibration signals. Next, a deep learning structure for gear teeth fault identification is built by combining the two networks' findings on gear teeth fault characteristics. The provided approach is put through its paces by being applied to 41 unique gear fracture circumstances. The gear crack fault diagnostic result demonstrates that the provided technique achieves an accuracy of over 93% with little training data. The suggested approach provides more precise diagnostic outcomes than either the CNN or LSTM network alone. The reliability of the provided technique for gear fracture defect identification is shown by contrasting the results obtained using different sample sizes and methods.

Further, a novel method for gear defect classification that integrates time-frequency analysis with image processing is proposed. This method may identify and categorize gear defects using the vibrating signals induced by cracked gear teeth. Empirical Mode Decomposition (EMD) and Principal Components Analysis (PCA) are used to deconstruct the signals into their principal components. To visualize the time-frequency connection of the primary components of the studied signal, the Short-Time Fourier Transform (STFT) is used to create the spectrogram for each element. Further, spectrogram pictures of primary components are converted into an array of features for each signal by extracting Image Moments. Then, a deep machine learning approach called a 2-dimensional convolutional neural network is used to achieve the classification (2-D CNN) utilizing image processing. As shown by the findings, the established method provides reliable classification, and the given deep structure can be readily expanded to include more sensor input signals for future gear crack failure diagnostics.

DEDICATION

To my heaven on earth, my beloved mother,

My late grandfather,

My siblings,

And my dearest friend, Motasem.

ACKNOWLEDGMENTS

This thesis was made possible by an Award from Qatar National Research Fund (a member of Qatar Foundation) [GSRA7-2-0512-20054]. I would like to acknowledge the support of Qatar University for providing all the needs to achieve the requirements of this study.

I would like to express my deepest gratitude to my advisor, Professor. Sadok Sassi, whose sincerity and encouragement I will never forget, as this thesis would not have been possible without his guidance.

TABLE OF CONTENTS

LIST OF TABLES

LIST OF FIGURES

CHAPTER 1: INTRODUCTION

This chapter gives a background about gears, including their importance, leading failure causes, and their different monitoring techniques. In addition, details on artificial intelligence and its applications in the contemporary world and the subject of condition monitoring are presented. Afterward, the motivation and the study's aim and objectives will be stated. Finally, the layout of this research will be described at the end.

1.1 Background

There is no doubt that gears have existed for at least as long as humanity has existed. Despite this, the manufacturing industry's reliance on gears isn't waning but instead expanding. For this definition, "gear" refers to a piece of a machine that is used to transfer motion and power between rotating shafts by the progressive engagement of projections known as teeth [1]. This seemingly simple engineering component has become so crucial in today's technology that engineers are constantly working on gear systems, mechanisms, and arrangements that are novel, highly efficient, and unconventional to meet the needs of contemporary technology and the challenges that confront engineers in every field [2].

Gears work in pairs, as shown in Figure 1, with the smaller of the two being referred to as the "pinion" and the bigger as the "gear." The pinion usually drives the gear, and the system serves as a speed reduction and torque converter. The center distance between the spinning shafts in a gear drive is typically not too great. Various power transmission technologies, such as belt drive, chain drive, and so on, are used when the distance is rather long. [3].

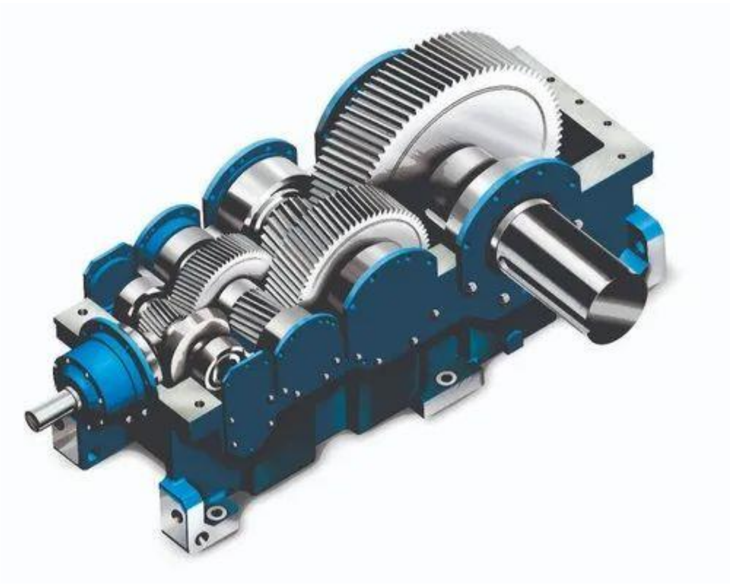

Figure 1: Gearbox [1]

Gears may be divided into three types based on their shape: involute, cycloidal, and trochoidal. In addition, they may be classed according to the location of the shafts as parallel shaft gears, intersecting shaft gears, and non-parallel and non-intersecting shaft gears, among other classifications. Even though the kinds and modalities of gear vary significantly, one of the most prevalent types of gear found in industries is the spur gears, as seen in Figure 2, which have teeth that are straight and parallel to the shaft axis. They transfer power and motion between two parallel rotating shafts.

Figure 2: Spur gear [2]

1.2 Gear Failure Causes

Gears may fail in various ways, except for increased noise and vibration, unless there is an issue. There are no warning signs up until ultimate failure happens [3]. Fatigue, fracture, wear, as well as stress rupture are examples of general malfunction mechanisms (from least to most often) [4-5]. Failures of gear teeth occur twice as often as expected in discrete areas: the root fillet and the tooth's lateral surface [6]. Bending stress for gears with narrow rims might vary according to rim and web thickness [7-9]. A gear's outer rim frequently breaks among teeth close to one other in a thin-rimmed casing. Cracks began appearing on the rim and spreading into the web, as shown in Figure 3. [9]. At the rim-web intersection, cracks may form in the web, but the rim is unaffected. A gear that has been harmed may bring a machine's whole functioning to a halt. Consequently, gear tooth breakage is the most critical issue, then in the worst-case scenario, it may lead to the machine's extermination.

Figure 3: Crack in gear tooth

The root of a gear tooth that has developed a fracture results in gear tooth failure due to bending fatigue. Under cyclic stress, in many cases, several instances of the break that leads to fracture were documented to have a fatigue focal point. Severe loading may also cause fractures in teeth. Short-cycle tooth breakage produced by an excess load that surpasses the tensile has a more refined, stringier appearance, notwithstanding the indications of being quickly ripped apart [10]. Understanding how a gear might fail is critical before engineers can develop safe and efficient gears.

Discussed in [10] methodologies used in several studies to better understand gear bending strength. Design engineers may benefit from gear testing by better understanding and forecasting various sorts of gear failures and the service life of gears [11]. Understanding the specific kind of the first failure and devising a technique to prevent such shortcomings is beneficial to the designer. The American Gear Manufacturers Association (AGMA) and the International Organization for Standardization (ISO) publishes numerical gear design standards that contain complex equations and calculations. FEM is also used to predict gears' failure and estimate gears' service life [12]. Experimental testing on bending strength is then used to verify the theory. Besides numerical computations and FEM, gear bending strength may be determined by actual gear experiments. To distinguish the most probable source of failure, gear design calculations and experimental testing are necessary [13].

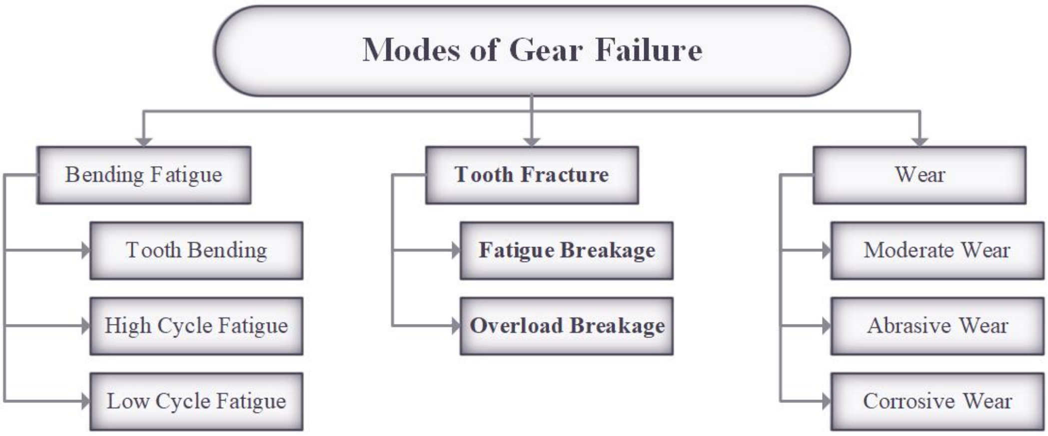

Figure 4: Failure modes of gears [10, 13]

In general, tooth wear, tooth-bending fatigue, and tooth-bending impact are all examples of cyclic stress failure in a pair of gear teeth [14]. Failures of gear teeth occur in two discrete areas the root fillet and the tooth's lateral surface. As seen in Figure 4, the gear may fail in various ways.

A fractured tooth is the most concerning reason since broken gear may halt a machine's functioning and, in the worst-case scenario, lead to the machine's destruction. In thin-rimmed cases, fractures in the web around the rim and web junction might occur devoid of damaging the rim in its entirety. The gear rim can fail between two teeth, and cracks began to appear on the rim and spread into the web. When a gear tooth fails from bending fatigue, a fracture commonly starts in the root region of the gear tooth [3]. Excessive and cyclic loading, which push the gear tooth beyond its endurance limits, are other causes of bending fatigue failures.

The gearing system tends to wear down due to the way the gears engage with one another. Moderate wear is the most prevalent kind of wear failure. This wear occurs over many cycles and may be caused by insufficient lubrication or fine particles in the system. Abrasive wear occurs when gear lubricant contains metal particles, such as weld spatters or scale, together with rust or sand. [10]. Meanwhile, corrosive wear occurs due to corrosive impact on gear teeth. This wear failure is seen as patchy spots dispersed across the tooth of the gear [15].

1.3 Gearbox Health Monitoring

Early identification of premature failure in mechanical systems is critical for operators since it allows for planned shutdown and system repair rather than unanticipated disastrous collapse. Vibration analysis is one of the most important approaches for early failure detection. One must understand how changes in a system's mechanical condition might affect the vibration it produces, which is considered a core principle. The entire vibration may increase in amplitude due to a whole system, which may be easily measured with simple instrumentation. Changes in overall vibration caused by the degradation of a single piece of machinery will have less impact in increasingly complex systems, and more advanced approaches may be required to identify the damage.

Spectral analysis, which calculates and shows the spectral amplitude of the detected vibration time signal, has been a prominent vibration analysis approach throughout the previous decade. Because distinct parts of a mechanical system produce vibrations of various frequencies, spectral analysis is a robust approach. There are fundamental and harmonic frequencies of the gear tooth meshing frequencies in gearboxes, which are typically different for each set of gears. Changes in the spectrum, for example, a rise in the vibratory amplitude at a particular frequency or, in many cases, the formation of modulation sidebands at or around that frequency, may be traced back to a single component in a more complicated system. However, this classification may be problematic in more complex systems such as turbine gearboxes, which can contain up to 30 gears and 50 bearings. This is due to the large number of spectral lines produced by these components during operation. To determine the cause of change in the spectrum, it is necessary to compare the spectrum of the same system in excellent condition with the spectrum of the same system in a state of normal operation.

There are primarily two ways for gear defect diagnostics: data-driven-based methods and physical model-based methods. Methods that are data-driven depend only on the examination of previously gathered data in order to diagnose and forecast the health of gearboxes.

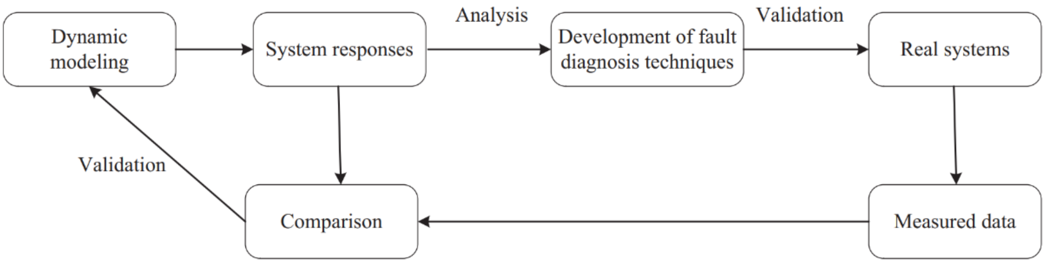

Figure 5: Diagnostics for faulty components based on motion dynamics [14]

Vibration signals, motor voltage/current signals, torque load signals, acoustic signals, metal scan data, gear weight loss data, gearbox strain signals, gear damage photos, and so on are all examples of the types of data that may be monitored. In order to diagnose problems with gearboxes, a number of data-driven techniques have been created [15].

Methods that rely on physical models make a digital representation of a real-world item, using that thing's known properties as a starting point. Modulation-based models and dynamics-based models are two categories that describe the underlying physics of gearboxes. By learning how vibration signals exhibit AM, FM, and PM modulation, more accurate models can be created. By first analyzing the mechanism and dynamics of gear meshes, dynamic characteristics under different health situations can be simulated, and the symptoms of any faults may be discovered and summarized in order to aid in the fault identification and diagnostic process.

By examining the behavior of gearboxes, methods for detecting problems can be created. Meanwhile, validating the dynamic models and the fault identification procedures is an essential operation. The experimental system or other models may be used for validation. The whole process is broken down and detailed in Figure 5.

1.3.1 Time Domain Analysis

Averaging over a period of time is an alternate vibration analysis approach that is increasingly being utilized for gear failure as it helps with spotting the problem early on. It has been shown that after several averages, any vibration that is not synchronized with the vibration of that gear tends to balance out with each turn, leaving a rough approximation if a second signal is acquired that is synchronized with that gear's rotation. This approach is especially beneficial for complicated systems like gearboxes because it removes vibration from various components of the system, focusing on a smaller, more manageable problem. The amplitude spectrum is given in the frequency domain, whereas the time domain average, as the title implies, is presented in the time domain, enabling the comparison between the signals generated by different gear teeth.

Because numerous failure types include the degradation of just a portion of a gear, identifying the damaged section by comparing it to the remaining vibration portion of the gear should be easy, as based on a single vibration measurement allows the identification of numerous failure types. This would be a considerable advance over spectrum analysis, which often includes comparing the suspicious spectra to the spectrum of the same or a similar system in great operating condition due to the complicated nature of the spectrum. When enough averages are achieved, the time domain average roughly estimates a signal that is periodic, with the essential conclusion of the time domain average's Fourier transform being a straight-line spectrum. As a result, it allows for the modification of the time domain average in the frequency domain, which includes strong processes like ideal filtering. Such processes are not feasible using traditional spectrum analysis techniques since the incoming signal contains many frequency components that, in general, are not quite cyclical inside the sampled data set. In order to enforce periodicity, it is necessary to utilize a window function that reduces values at the block's ends to 0.

Statistical scalar indicators like kurtosis and crest have shown great potential in various research [16,17] in the time domain. When a healthy tooth comes into touch with a damaged one, the effect on the signal is amplified, making these indicators very sensitive. Many investigations have demonstrated that the kurtosis factor is more responsive than the crest factor for detecting gear tooth flaws in relation to operation hours [18].

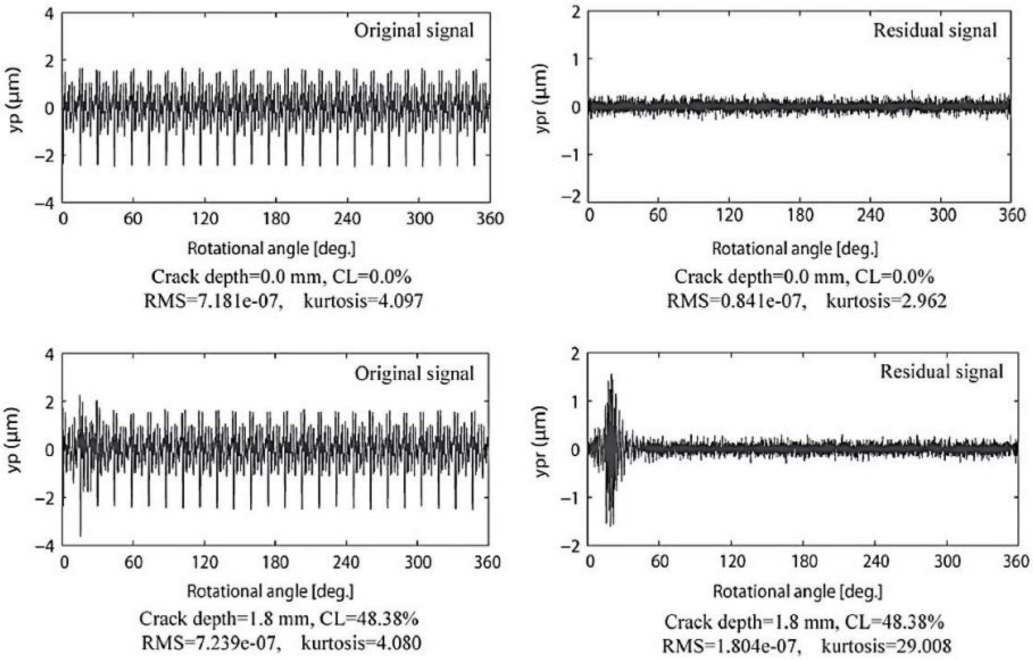

Figure 6: Signals for healthy and damaged gear, both original and residual [16]

1.3.2 Residual Signal Modulation Method

Normal signal content obscures the amplification caused by the tooth defect. The residual signal may be created to improve fault impact detection. In order to analyze the fault effect independently of the typical signal components, the concept of producing a residual signal relies on eliminating these components. It's important to note that several methods have been devised and used to produce the residual signal. Stewart [19], who invented a variety of defect-detecting features, is largely responsible for the initial method. One of the useful indications he offered was the measure FM4, which is the kurtosis of the residual signal. By subtracting the gear mesh harmonics from the spectrum and then converting them back to the time domain [20], Stewart's defect detection enhancement approach obtains a residual signal [21].

1.3.3 Frequency Domain Analysis

Spectrum analysis is the most traditional technique for studying signals in the frequency domain. Increases in crack size lead to an increase in the meshing frequency. Sidebands form around the meshing frequency in chipped gears, as seen in Figure 7, and the spacing of these bands corresponds to the rotational frequency of the shaft that carries this particular piece of equipment. These sidebands may not be seen on the spectrum in certain circumstances. Using a cepstrum analysis is required due to the obscurity of the sidebands. Similar lines may be distinguished using cepstrum analysis. The cepstrum is a vector that represents the inverse Fourier transform of the logarithm of the spectrum and is defined by Equation (1)

$$x(f) = \int_{-\infty}^{\infty} x(t)e^{-j2\pi ft}dt \tag{1}$$

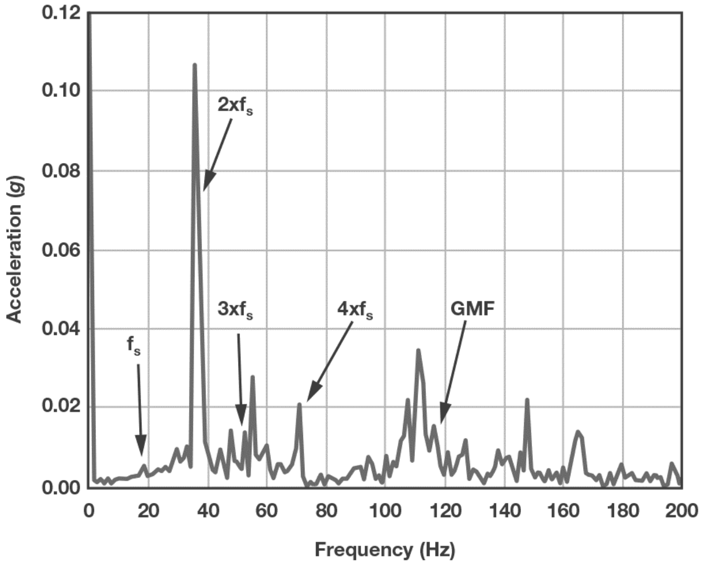

Figure 7: Frequency domain analysis of gearbox [22]

1.3.4 Time-Frequency Analysis

The amplitude and frequency content of the signal will fluctuate throughout the time in which the cracked tooth is in mesh for the majority of tooth faults. The nature of these short-term fluctuations would be anticipated to provide information about the kind and magnitude of the fault present. Investigating the use of time-frequency analysis of the signal average to overcome the shortcomings of existing enhancement strategies is essential. This type of analysis provides a representation of the signal in both the time and frequency domains, as well as a description of how the spectral content of the signal changes over time. The basic goal of a joint time-frequency distribution is to provide a representation of a signal's energy or intensity in both time and frequency [23].

The instantaneous energy (intensity per unit of time) of a time-based signal $s(t)$ Equals the absolute value of the signal squared as shown in Equation (2):

$$|s(t)|^2 = intensity\ per\ unit\ time\ at\ time\ t \tag{2}$$

The absolute value of the Fourier transform squared gives the energy density spectrum (intensity per unit frequency) as shown in Equation (3)

$$|S(f)|^2 = intensity\ per\ unit\ frequnecy\ at\ frequnecy\ f \tag{3}$$

Where $S(f)$ Is the Fourier transform of $s(t)$, which is defined as:

$$S(f) = \int_{-\infty}^{+\infty} s(t)e^{-j2\pi ft}dt \tag{4}$$

The intensity per unit time and per unit frequency at time t and frequency f should be represented by a combined time-frequency distribution $\mathrm{P}(t, f)$,

$$\mathrm{P}(t, f) = intensity\ at\ time\ t\ and\ frequnecy\ f \tag{5}$$

Preferably, adding $\mathrm{P}(t, f)$ for all frequencies at a given time would get the instantaneous energy, and adding $\mathrm{P}(t, f)$ for all times at a given frequency would yield the energy density spectrum, as seen in Figure 8.

$$\int_{-\infty}^{+\infty} \mathrm{P}(t, f) dt = |s(t)|^2 \tag{6}$$

$$\int_{-\infty}^{+\infty} \mathrm{P}(t, f) df = |S(f)|^2 \tag{7}$$

The 'marginals' or Equations (6) and (7) are the requirements that must be satisfied by a time-frequency distribution to be considered valid.

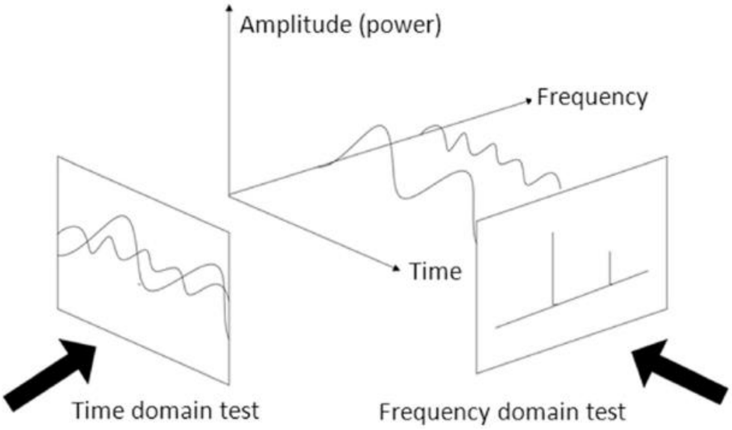

Figure 8: illustration of time-frequency domain analysis [23]

1.3.4.1 Empirical Mode Decomposition

To breakdown a signal, Empirical Mode Decomposition [24] relies on the direct identification of local extrema at different intrinsic time scales. Since the decomposition relies on localized timescales, it may be used for nonlinear and non-stationary signals, and the resultant Intrinsic Mode Functions (IMFs) are often regarded as the most salient features of the signal. When two criteria are met, an EMD signal may be represented by an IMF: First, it's local mean is zero; second, the difference between the number of extrema and the number of zero crossings is less than 1. Specifically, given a signal $x(t)$, the constituent IMFs, $c_i(t)$, can be obtained and summed using Equation (8):

$$x(t) = \sum_{i=1}^{K} c_i(t) + r_k(t) \tag{8}$$

Where K is the total number of IMFs, $r_k(t)$ is the final residue, which reflects the mean trend of the signal, and $c_i(t)$ is the subset of IMFs that is roughly orthogonal to one another and has a mean that is very close to 0.

1.3.4.2 Principal Components Analysis

Principal Components Analysis is a feature extraction technique that projects data into a lower dimensional subspace that contains most of the variance of the original data, thereby reducing the dimensionality J of data X_{IxJ} where I is the number of observations and J the number of features, with a minimum loss of information [25].

$$X = TP^T = \sum_{j=1}^{n} t_j p_j^T \tag{9}$$

With $n < J$.

According to Equation (9), PCA encodes data as the product of mutually orthogonal data, denoted by scores $T_{ixn} = [t_1, t_2, \dots, t_n]$, and a transposed linear transformation matrix, denoted by the principal component matrix $P_{jxn} = [t_1, t_2, \dots, t_n]$.

It is essential to find the correct number of main components n to pick in order to produce the optimal subspace for the signals. This may be done by analyzing the data. As a result of the significance of this component, a wealth of research has been published in the relevant literature, presenting a variety of approaches.

1.4 Artificial Intelligence

It is now possible for computers to learn from data and make predictions without explicit programming by using machine learning, which is now one of the most popular research fields. To train a machine learning model, input/output pairings are employed, with the objective of producing a function that is approximate enough so that it can predict outputs for new inputs when they are given to the model, as well. Regression and classification issues are two types of supervised learning tasks, as shown in Figure 9. Classification vs. regression are two different types of problems that arise when the outputs are categorical rather than continuous

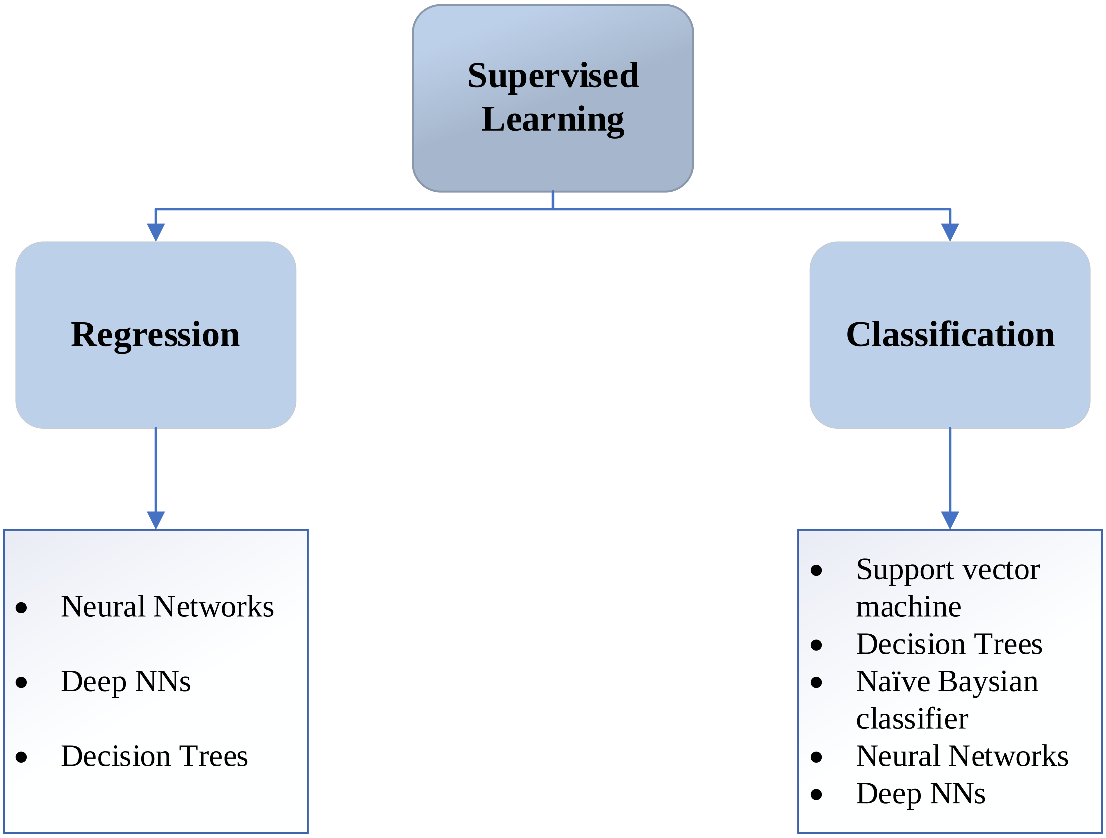

Figure 9: Types of supervised machine learning and their corresponding networks/algorithm

1.4.1 Machine Learning

As computing power continues to increase at an exponential rate, more and more systems rely on Artificial Intelligence (AI) methods to aid with data processing. However, the assessment of health is difficult in the existing model-based investigations on mechanical gearing devices and rotary machinery [26].

In recent years, Deep Neural Networks (DNN), Convolutional Neural Networks (CNN), and Recurrent Neural Networks (RNN) have emerged as the most widely used machine learning systems for defect identification and diagnosis. Machine element condition monitoring, including gears, may be seen as a pattern recognition problem that has been successfully handled by smart diagnostic techniques. Literature suggests that there are four main phases of condition monitoring: data gathering, feature extraction and selection, feature categorization, and finally, feature classification.

Most often, RNN is used for dynamic information processing, such as time series prediction and process control. [27] In computer vision, speech recognition, and defect detection, CNNs are popular active learning models [28]. AI-enabled neural networks (ANN) have changed the landscape of machine learning dramatically in recent years. In typical machine learning tasks, these biologically inspired computer models outperform prior types of artificial intelligence. When it comes to artificial neural networks, the Convolutional Neural Network (CNN) stands out as one of the best Artificial Neural Networks. Because of their exact but basic design, CNNs are a great way to get started with ANNs for tough classification problems.

Systems that mimic the way organic nervous systems (such as the human brain) function are known as Artificial Neural Networks (ANN). There are many linked nodes (called neurons) in an ANN that work together in a distributed way to learn from the input and maximize the final output.

Figure 10 depicts the fundamental construction of an ANN. Multidimensional vectors, which are basically the input data, are typically entered into the input layer, which then distributes them to the hidden layers. The process of learning is carried out by the hidden layers, which use the judgments made at the preceding layer to determine whether a stochastic change inside itself has a negative or positive impact on the final output. Additionally, when several hidden layers are piled one on top of the other, it is widely known as "deep learning."

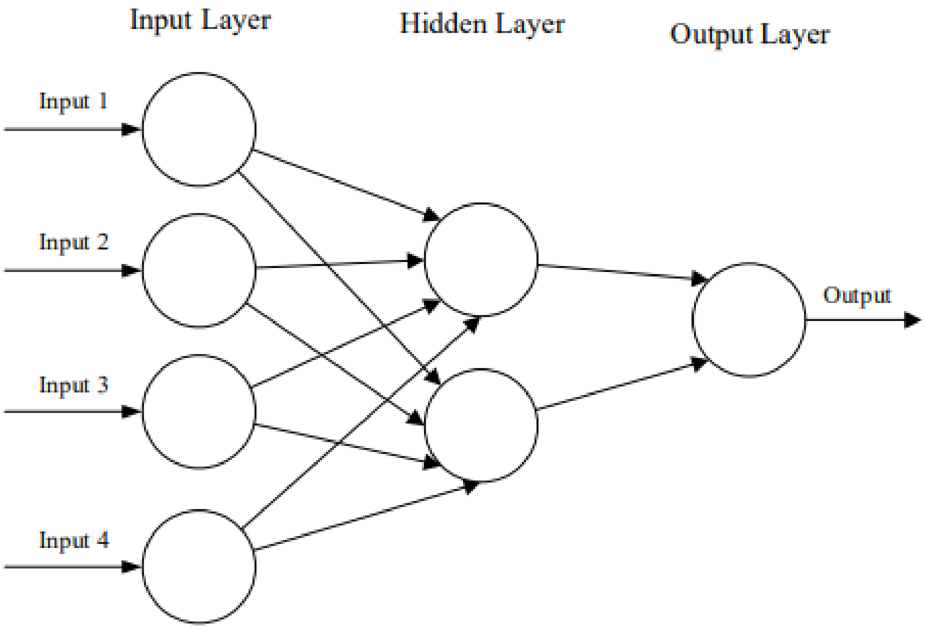

Figure 10: A simple three-layered feedforward neural network

1.4.1.1 Convolutional Neural Networks (CNNs)

With their precise but simple design, CNNs are generally employed to handle challenging image-driven pattern identification problems. Furthermore, unsupervised and supervised learning are the primary methods for learning in image processing. Learning using pre-labeled inputs serves as supervised learning. Input values and one or more predefined output values for each training example will be provided.

To improve overall classification accuracy, this method involves calculating the model's output value correctly for each training case, and this is the sole purpose of this method. On the other hand, there are no labels in the training set for unsupervised

learning. The network's ability to lower or enhance an associated cost function is typically what determines its success. To be clear, the vast majority of image-based pattern recognition tasks depend on supervised learning to classify input images [28].
As with classic ANNs, Convolutional Neural Networks (CNNs) are composed of neurons that learn and self-optimize. Many ANNs have their roots in the fact that each neuron still receives input and performs a function (a scalar product followed by a non-linear function, for example). The network as a whole will still express a single perceptual scoring function with respect to the input raw image vectors and end with a class score that is called ‘the weight.’ In the final layer, the loss functions in conjunction with the classes will be used, and the entirety of ANN instructions and techniques will still be applicable [29].

Pattern recognition in pictures is where CNNs vary from regular ANNs in that they are mainly used to identify patterns inside images. The structure of the network, as seen in Figure 11, may include these characteristics, making it more suited to image-oriented activities while also lowering the number of factors needed to build up a model, which serves the purpose of this research of building a model that classifies gear cracks from preprocessed figures.

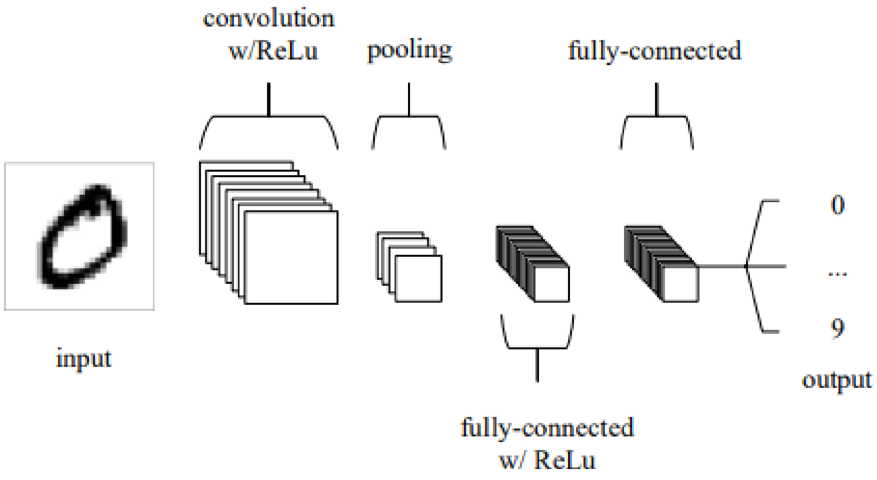

Figure 11: A basic CNN design with only five layers [29]

1.4.1.2 Recurrent Neural Networks (RNNs)

Recurrent neural networks (RNNs) are feed-forward neural networks that focus on modeling in the temporal domain. RNNs are unique because of their capacity to transmit data in discrete increments of time. In order to facilitate training in the temporal domain and make use of the sequential character of the input, RNNs are designed with an extra parameter matrix for connections between time steps. Recurrent neural networks (RNNs) are taught to produce results in which predictions at each time step are derived from both the current input and data from earlier time steps. When analyzing data in the time series domain, RNNs may be useful. Elements in one timestep are connected to elements in earlier timesteps, and the data in this domain are ordered and context-sensitive [30]. In Figure 12, the distinctions between a regular neural network and an RNN can be seen.

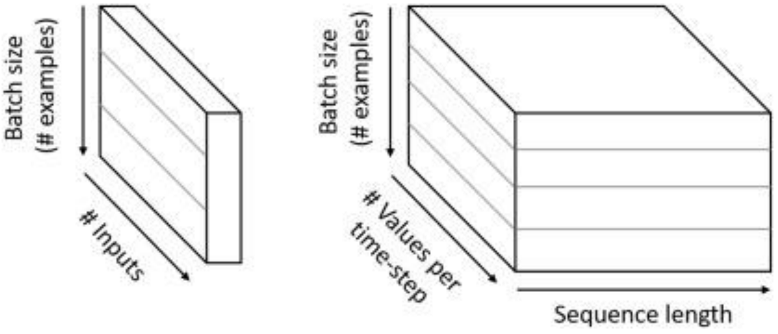

Figure 12: Comparison between normal and RNNs input vectors [30]

RNNs are the first to use the concept of recurrent connections, as was previously noted. In this configuration, the output of a hidden-layer neuron serves as a feed stream to another instance of the same neuron in the same layer. Figure 13 depicts the RNN's recurrent connections as well as the information flow between its nodes.

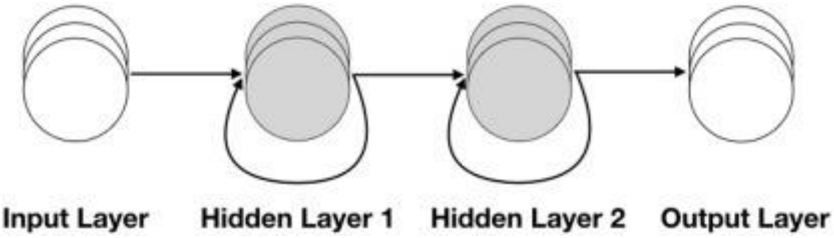

Figure 13: Feedforward flow for recurrent neural network

Each neuron in the hidden layer is activated by both the current input vector and the hidden states of the preceding time step. Therefore, prior input vectors have an effect on the present time step's output which is called unrolling in RNN. Figure 14 shows how an RNN does term unrolling for time steps.

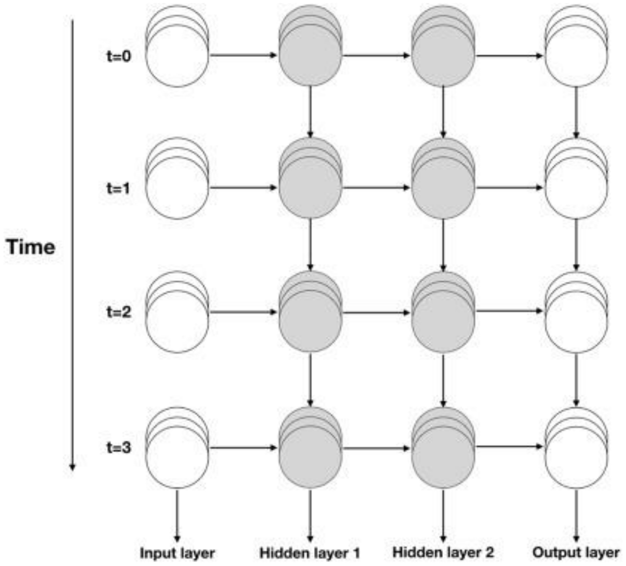

Figure 14: Unrolling for recurrent neural networks.

1.4.1.2.1 Classification Using RNNs.

Since recurrent neural networks (RNNs) are optimized for collecting contextual information by establishing the relationships between different time stamps, they are often utilized to carry out the sequence analysis procedure [31,32]. In order to map one sequence onto another, an RNN uses a series of recurrent layers that are modeled in order. An RNN's strong suit is its ability to pick up on sequence context. However, the network structure's contextual cues are reliable and may be leveraged to complete the data categorization process successfully. The length of the sequences doesn't matter while using RNN [33]. The RNN classifier's architecture is shown in Figure 15.

.

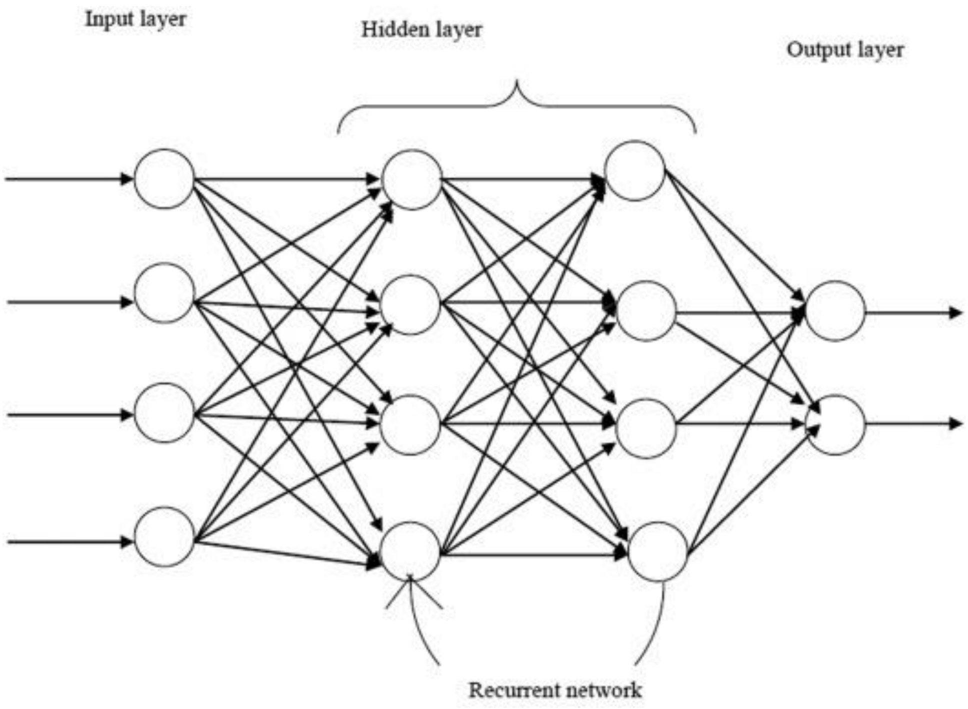

Figure 15: Architecture of RNN classifier. RNN, recurrent neural networks.

Feedforward NN may be expanded into RNN by adding loops in the hidden layers. In order to determine how time affects the input sequence of samples, RNN analyzes the data. By augmenting the network parameters with the hidden node and releasing the state depending on the input values, the Long short-term memory (LSTM) resolves classification problems [32]. In comparison to LSTM, RNN performs better since its states may be activated in response to actual network activity. Common RNN nodes have only one bias and weight. Gated recurrent unit and LSTM are used to test the RNN. By adjusting the network parameters, a one-to-one connection is made, where input data at a certain time step yields an output at the same time step. As opposed to only one in a standard RNN node, each LSTM node has four biases or weights to the extent detailed below:

- Forget gate layer

- Input gate layer
- Output gate layer
- State gate layer

The current input state and the cell's state are both influenced by the input and the forget gates. However, the sigmoid function is used to scale the input, the output, and the forget gate activation, and the hyperbolic function is used to filter the output of the hidden state. Optimization of network parameters through stochastic gradient is performed on the basis of an input data sequence. To be more specific, the hyperparameters are the network's topology (number of layers and size), as well as the sequence length, batch size, momentum, and learning rate. Stochastic or human-guided search is used to determine values for the hyperparameters. The RNN takes a vector sequence as input shaped as $\{y_1, y_2, y_3, \dots, y_m\}$, the sequence of hidden states as $\{z_1, z_2, z_3, \dots, z_m\}$ and the output unit as $\{v_1, v_2, v_3, \dots, v_m\}$, respectively. The hidden state is generated by the recurrent function d in the recurrent layer, which receives as input the input vector y_x and the hidden unit of the previous state z_x.

$$z_x = d(y_x, z_{x-1}) = \tanh\,(P.y_x + Q.z_{x-1}) \tag{10}$$

In addition, the output units are determined by the formula,

$$v_x = softmax(R.z_x) \tag{11}$$

Where the activation function **tanh** denotes the hyperbolic tangent function, and the weight matrices are represented by the letters **P**, **Q**, and **R**. For the purpose of capturing long-term dependencies, RNNs utilize a very complex function for learning and controlling the flow of information in the recurrent layer. An illustration of RNN's construction may be seen in Figure 16. In the case of multilabel classification, the output function is changed from SoftMax to sigmoid.

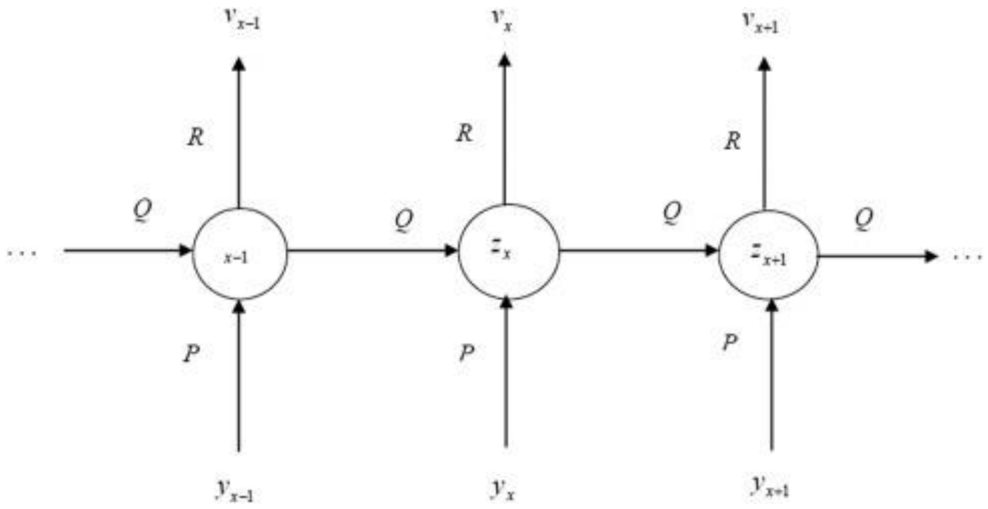

Figure 16: Structure of RNN. RNN, recurrent neural networks

1.5 Research Objectives

The aim of this research is to study the vibrations induced by the dry friction between meshing teeth and the mechanics of the friction force in relation to surface deformation and its effect on the gear vibration signal to develop a numerical model that generates a signal similar to the real-life machines. To then utilize both modeling methods and onsite tests, providing a new benchmarking data collection representing the normal/abnormal features of the different types of machinery and geared systems, that will be used as a data generation model to develop a robust machine learning algorithm that excels in fault detection of gear defects.

1.6 Thesis Layout

Chapter 2 is a literature review on numerical dynamic gear models and modeling techniques—some relevant background on gear teeth and cracks geometries. In particular, more details are provided about the calculation of gear mesh stiffness in the presence of cracks and about the 6-dof numerical model. And modern machine learning approaches for detecting equipment failures, with an emphasis on gear issues and deep learning.

In Chapter 3, Theoretical and numerical development of the numerical model and the methodology of how friction-induced vibration is calculated. The main variables are the curvature radii between teeth, their relative velocity of slipping, and their mutual elastic deformation area estimated by Hertz's theory of contact, and then three different types of vibration noises are developed; modulated, constant and a ratio of both modulated and constant noises combined.

In Chapter 4, The experimental setup is described, with information on the test rig, data acquisition system, cracked gears, and experimental vibration findings retrieved and checked for reliability.

In Chapter 5, the results of the developed numerical model with the different types of noises are validated and compared to the results in section 4 of the test rig, and the conclusion is drawn on which type of error is the most realistic.

In Chapter 6, two different machine learning approaches based on the type of data input, where one takes a time-series signal, and the other uses images to process and train, utilizing 1D – 2D Convolutional neural networks CNNs and Recurrent neural network LSTM, the results are discussed and compared at the end.

In Chapter 7, In this chapter, the results that were noteworthy are emphasized, the conclusions are presented, and suggestions are made for more studies that should be done for future work.

CHAPTER 2: LITERATURE REVIEW

A complete review of the relevant previous research will be carried out in this chapter. The chapter begins with a discussion of the dynamic gear fault modeling methodologies that have been used in the past, as well as any prior research that has been conducted on friction-induced vibration in meshed gears and machine learning for the detection of machinery faults. In the end, a review will be given on dynamic gear models as well as the experimental setups.

2.1 Dynamic Gear Fault Detection Models and Techniques

Machine health may be evaluated with the use of vibration signals; hence this method of defect detection has found widespread use across various industries. Studying the dynamic response of a mechanical system, determining its state by detecting any change in the vibration signal owing to deterioration, and providing an early warning are all made possible via vibration analysis. Detecting problems early on enables the whole system to be shut down at the appropriate time, avoiding an unscheduled and potentially disastrous outage [34]. Identifying a malfunctioning part or component is the essence of fault detection in machines and other systems. When a failure event occurs, and an item enters a fault state, the system as a whole may continue to operate but with reduced functionality. So, no system-wide failure has happened, and the system as a whole is not in an error condition.

The gear tooth may be thought of as a component of the gear itself when dealing with problem detection in gears. A tooth is regarded to be defective if it contains a problem, such as a tooth crack, that causes the specified dynamic qualities to drop below a predetermined limit. The gear as a whole, however, may still function, although at a diminished capacity.

The following sections detail the first three phases of vibration-based defect detection [35-38]:

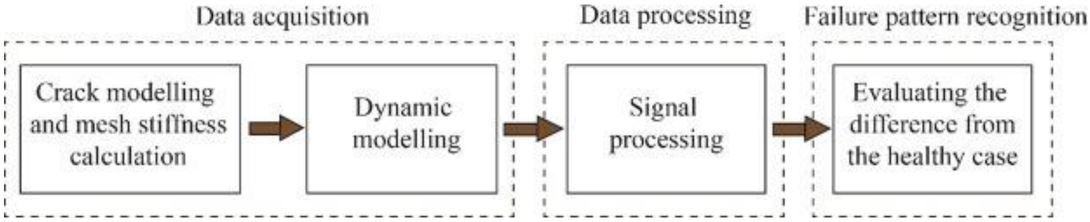

Figure 17: The main stages of the vibration-based fault detection process [36]

- Experiments and theoretical modeling and simulation with dynamical systems provide the "data acquisition" (data space) for vibration signal data gathering.
- Data processing (feature space)—feature extraction from vibration signal data.
- Fault space analysis (failure pattern detection) to evaluate the health of a machine using its retrieved characteristics.

2.1.1 Experimental Fault Detection Models

The dynamic response may be determined either via experimental data-driven approaches or through theoretical modeling-based simulation. Numerous studies have analyzed the vibration signal recorded experimentally for gear problem detection [39–43]. Although experimental measures have the benefit of being representative of real-world systems, they are not without drawbacks, as the measuring nodes may be inconvenient or impossible to reach in certain cases, and it takes a lot of time to conduct an experiment and then measure it many times to account for varying fault conditions. In other circumstances, such as those where new fault sizes need to be manufactured, the expenses associated with investing in and maintaining measurement equipment might much outweigh the available funds for the study. Additionally, it may be difficult to generate genuine flaws of the required size. Furthermore, Studying the impact of altering a parameter, such as inertia, stiffness, damping, etc., may be challenging. Also, there is a possible danger in using experimental measurement.

These issues with experimental measurements may sometimes be resolved, allowing for the collection of genuine, high-quality data, but in many other circumstances, there are hurdles in this relationship that are very tough to overcome. Many of these issues may be addressed with the help of modeling and simulation, which can also serve as a viable alternative to more complex methods of studying the dynamic behavior of the gear system in question. However, information on the system's dynamics, the system's excitation, and the degrading qualities of the system's components through time, rotation, and load, for example, must be provided as input for the simulation technique. Creating a model that strikes a good balance between clarity and accuracy is the primary objective of modeling. [44]

2.1.2 Numerical Fault Detection Models

The models used in model-based approaches are divided into two categories: those based on modulation and those based on dynamics [45]. By studying how the signal qualities under study are modulated, useful models may be developed. Modulation techniques include amplitude modulation, frequency modulation, and phase modulation. Tooth engagement, fault modeling, and gear dynamics are all left out of modulation-based models. Components of the response signal are provided to represent the response, and any planned modification is introduced directly as a modulation of the signal. Models based on modulation are explored in [46–52]. However, in order to acquire the dynamic system response reflecting the system state, dynamics-based models are built based on the tooth mesh mechanism, fault modeling, and gear system dynamic modeling. By dynamically replicating the system in varying states of health, signs of failure may be researched for use in fault detection. Dynamic response simulation research has focused on a number of models based on gear dynamics [53–66].

2.1.2.1 Finite Element Modeling

For decades, gear dynamic modeling has been recognized as an important challenge that needs ongoing study. Among other research, [67-70] used an FE-based deformable body gear dynamic modeling to investigate the dynamic behavior of gear systems. In addition to obviating the necessity to model the TVMS, this method of modeling also includes the primary excitations of the system—a good depiction of tooth contact, the dynamic force components, and the transmission error calculation. However, FE-based gear dynamic modeling uses many nodes and fine meshes in the contact zones, which increases the calculation time. As a result, lumped-parameter gear dynamic models have been widely used because of the greater computational efficiency they give. But lumped-parameter gear dynamic modeling relies on predetermined parameters to derive the system's dynamic response, with just the modeled parameters' contributions being shown.

2.1.2.2 Lamped Parameter Modeling

Many different dynamic models of gears with lumped parameters have been created and used. In [71], a 4-degree-of-freedom (DOF) gear dynamic model was used for clarity's sake, whereas in [53], Bartelmus analyzed a variety of gear models. Considering the inter-tooth friction and disregarding the rotation of the load and motor, the 6 DOF gear dynamic model proposed by Bartelmus [53] has been utilized in [56-62,65,72,73]. Considering both torsional and translational vibration, the 8 DOF gear model was utilized in [57,65,74] to provide a more realistic simulation of the gear train's behavior under load. In [58,65,75], a 6 DOF model was used (an 8 reduced to 6 DOF model) by disregarding the inter-tooth friction and just taking into account the rotation of the load and the motor. Mohammed et al. [65,66] constructed a 12 DOF gear dynamic model, shown in Figure 20, to describe the gyroscopic DOF and to investigate the dynamic response from a defect detection viewpoint. With the help of the created model and certain alternative models, the dynamic response was derived. The authors find that the 6 DOF model (the 8 reduced to 6 DOF model) is sufficient for a symmetric disc but that the proposed 12 DOF model provides better accuracy in all other cases. In [75], the authors provided a 14 DOF model, which takes into account six translations, six rotations for both the pinion and the gear, and two additional rotations for the rotation of the load and the motor. Although the proposed 14 DOF model yielded empirically verifiable findings, it has not been compared to other models in the literature to determine whether all the included DOF are indeed essential. Moreover, Howard et al. [63] created a 16 DOF gear dynamic model, which was then utilized by Zhou et al [64] to analyze the dynamic behavior of a single-stage gear system.

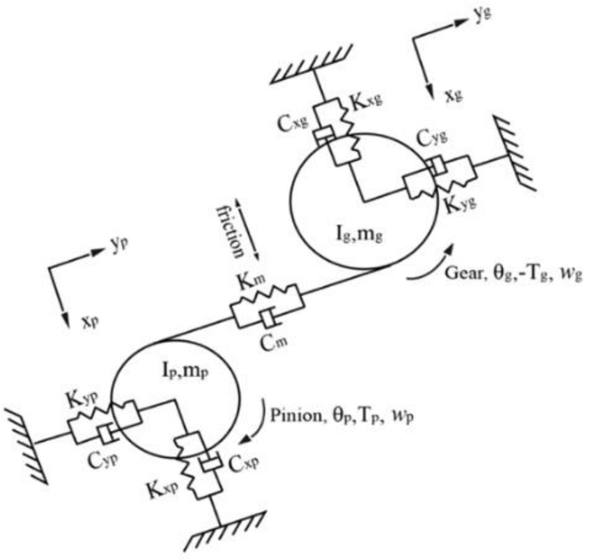

Figure 18: reduction gear dynamic model with 8 DOF [65].

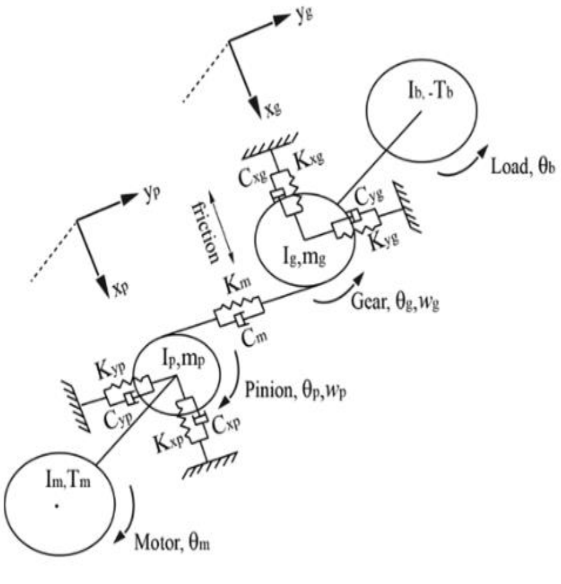

Figure 19: A reduction gear dynamic model with 8 DOF [65].

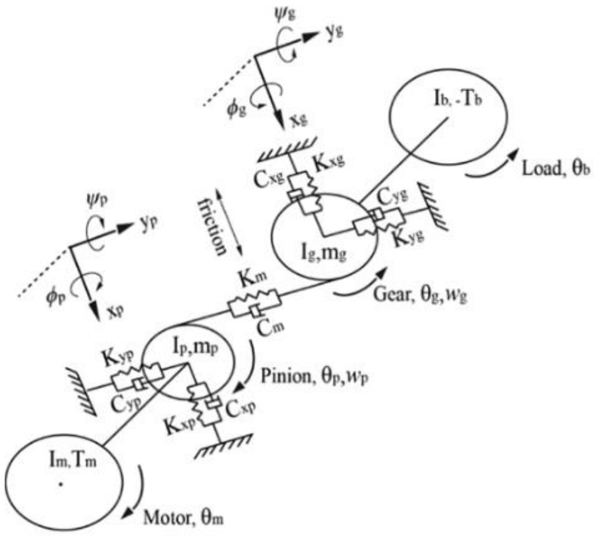

Figure 20: A reduction gear dynamic model with 12 DOF [65].

"gear" refers to the bigger gear, which is the driven gear attached to the output shaft. The "gear" that is smaller is the driver gear, and it is connected to the input shaft.

2.2 Gear Fault Diagnostic

Many vibration signal analysis-based techniques have been developed for gear crack defect diagnosis. Diagnostic success has been achieved using tried-and-true techniques [76], such as root-mean-square, kurtosis, and power-spectrum analyses. However, their primary weakness is that they assume the signal-generating process is stationary and linear [77]. Several novel approaches have been developed and widely used for non-stationary processing signals, including time-frequency distributions [78], wavelets, higher-order statistics [79], and empirical mode decomposition (EMD) [80]. Loutridis [81] introduced an approach for tracking the development of gear defects using an empirical mode decomposition strategy. He also introduced energy-based characteristics for gear failure detection and prediction, using the instantaneous energy density to achieve high values when faulty teeth are engaged.

2.3 Friction-Based Induced Vibration

Usually, the point of contact between meshing teeth is constrained to stay along the line of action between two extreme points, as seen in Figure 21. The point where the two pitch diameters intersect is the only location where there is pure rolling. In all the rest of the locations, the relative motion between the teeth is a combination of rolling and sliding.

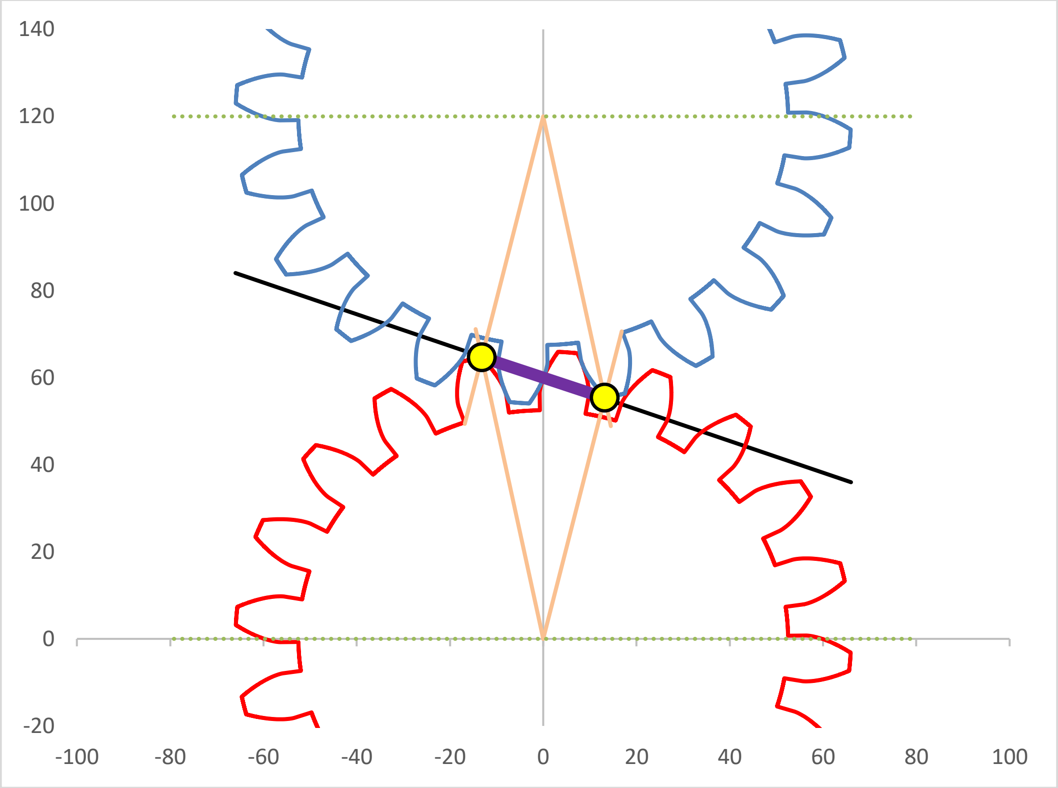

Figure 21: Path of contact engulfed by the starting and ending points of contact

As a result of the tribological conditions associated with sliding contact, there is surface deformation and even material fracture. The interaction of two media in relative motion generates elastic waves that produce acoustic emission (AE) and random mechanical vibrations. Dry friction and its relation to mechanical vibrations have been the subject of many studies. A vastly studied mechanism of dry friction has been the stick-slip motion of the sliding contact interfaces. Classically, dry friction is assumed to manifest itself as a tangential force that is directly proportional only to the normal interface force. Finding out how much friction there is when gears mesh was the primary subject of the first studies of friction's effects. It was unknown, however, how friction significantly impacted gear static and dynamic performance. The 1990s saw the beginning of friction being included in certain gear tooth contact assessments. Significant advancements were achieved in the study of gear performance, and more precise and dependable methodologies for predicting linear and nonlinear reactions to gear tooth contact were presented. Using the finite element approach and the Lagrangian multiplier methodology, Vijayarangan and Ganesan [82] assessed the static contact stress of the spur gear tooth, taking into account the influence of friction. The discrepancy between the observed and predicted contact times was a topic of discussion. They showed the contact stress gradient along the contact surface perpendicular to the mating surfaces. Rebbechi et al. [83] measured strain at the root fillets of two consecutive teeth during their investigation of the dynamic friction condition in 1996. The values of the coefficient of friction determined are consistent with those commonly used, and the results of their investigation showed that the friction coefficient does not seem to be much impacted by the sliding reversal at the pitch point. A higher coefficient of friction was observed at slower sliding speeds. When compared to the previous decade, the findings of current investigations may be relied upon more confidently. For error-free spur and helical gears, Velex and Sainsot [84] provided an analytical characterization of tooth friction excitations using the Coulomb model in 2002. With a mixed lubrication model, Mihalidis et al [85] determined the coefficient of friction at many contact locations along the path of contact for typical spur gear. The state of the frictional effects and the nonlinear performances generated by such sliding friction has recently received increasing attention from gear designers. Considering sliding contacts between meshing gear teeth, Kim and Singh [86] published a novel gear surface roughness-induced noise source model in 2007. They also addressed a dynamic condition for estimating transmission noise. The model presented by He et al [87] is extremely accurate and important for gear performance analysis since it takes into account sliding friction. Research into gears is hindered by issues like nonlinear dynamic responses and frictional effects and the connection between individual dynamic responses (noise and vibration) and frictional effects in particular.

On the other hand, the signals that are produced by malfunctioning rotating components in many mechanical applications, such as gearing systems, combine impulsiveness with a recurrent energy release of a random kind. The end result is a mixture of periodic impulsive vibration and random vibration caused by friction, which is commonly mixed with AE. The link between surface roughness and AE signals produced in sliding contact has been the subject of some investigation, both theoretically [88] and empirically [89]. These studies have looked at the relationship between the two in different ways. Due to the fact that non-linearities of contact and friction need to be taken into consideration, the acoustic response that is connected with squeal noise radiations is a challenging problem.

In some studies, vibration kurtosis has been utilized to identify tribological changes (for example, in surface roughness), but notable outcomes have not been discovered [90]. This is because vibration kurtosis has the potential to detect defects. In the diagnosis of bearing problems, kurtosis has also been effectively used for acoustic emissions, which are often more impulsive (non-Gaussian) than vibration signals [91]. However, there has been relatively little study done on the use of AE kurtosis to evaluate tribological conditions. Hamel et al. used kurtosis to measure the peaked-ness of AE signals obtained from a pair of helical gears under different lubrication regimes [92], but the results only showed that the oil film thickness could influence the impulsiveness (Gaussianity) of AE signals, and no clear relationship was proposed.

By their very nature, the AE signals that are utilized for assessing the tribological characteristics of machine components (such as gears and bearings) while they are operating are random [93]. AE signals that are measured in rotating and alternating machines are seldom steady because of the peculiar cyclic kinematics of these machines. This means that the statistical features of the AE signals change throughout the course of time [94]. A common manifestation of non-stationarity is a change (also known as "pulsation") in the amount of energy carried by a signal at a moment that is simultaneous with the angular rotation of a reference shaft. Cyclo-stationary is the term that's used to describe this kind of non-stationarity [95]. Within each cycle, the distribution of the signal samples varies in time (non-stationary), but the same distribution is found for samples that are separated by multiples of the cyclic period [96]. Every cyclization signal is characterized by a fundamental cyclic period (in machines linked to the rotating speeds of the shafts).

2.4 Machine Learning Techniques for Gear Faults Detection

In the realm of machine fault diagnosis, a great deal of attention has been paid to the extraction of defect characteristics using various signal processing methods [97].

Artificial Neural Network (ANN) signal processing methods are being used with the intention of reducing background noise prior to defect characterization identification. Taking use of signal noise to recover features and, by extension, flaws set Stochastic Resonance (SR) apart from more conventional signal processing methods. As a result, both fault-specific extraction and system fault diagnosis have seen heavy deployment. Since transmission problems reside primarily at the microstructure or perhaps the material stage, but their effects may only be noticed indirectly at the machine, rapid detection of gear failures has become a serious challenge. As a result, the effectiveness of the gear defect diagnosis tool is reliant on the characteristics of the classifier [98]. Recent methods centering on DNNs with adaptive feature extractions have received a lot of interest from researchers. However, they often need a large dataset in order to train. As a result, problems with planetary gearboxes may cause serious harm and costly downtime and maintenance needs. Motor Current Signal Analysis (MCSA) is a non-destructive technique for finding mechanical flaws in moving parts, and it has been developed as a response to such problems. Numerous DNN-based diagnostic algorithms have been described, providing rapid, accurate analysis of massive datasets and diagnostic results. Most cutting-edge methods, however, are devoted to defect detection using vibrational signals. Using pre-processed signals and DNN-based systems, the authors of [99] investigated planetary gear diagnostic issues. Utilizing laboratory data, which contain substantial measurement signals reflecting 15 distinct health concerns under diverse loading configurations, demonstrates the approach's strengths in comparison to comparable methodologies. Gears, as transmission mechanisms, are among the most important parts of mechanical equipment in many commercial settings. Pitting flaws in gears may cause failure, which can lead to safety and financial disasters; consequently, gears should be routinely examined, which is often done using raw vibration signals [100]. Therefore, an Augmented Deep Sparse Auto-encoder (ADSAE) was proposed in [101], which is used for gear crack defect identification with little information. Cleverly using a deep, sparse autoencoder system, this method has its effectiveness verified by looking at six different types of gear crack cases. The results reveal a highly encouraging increase in the network's generalization and resilience, with a corresponding increase in its accuracy. Both linear and nonlinear techniques were used to assess gear states by the authors of [102]. Pareto maps, biplots, and key angles are all examples of linear approaches, whereas curvilinear component analysis is an example of a nonlinear methodology, providing the manifolds in the given class are sufficiently well-differentiated and compact. A shallow neural network is used instead of a deep one for this reason. The authors' assertion is corroborated by preliminary findings, which also serve as a comparison to other published methods. In [103], a method for identifying gear loss was given using the Mel-Frequency Cepstral Coefficient (MFCC) and the Gamma Tone Cepstral Coefficient (GTCC), both of which are produced momentarily from vibration data with errors of a temporal character. As a result, a Long Short-Term Memory (LSTM) classifier is used because of its efficacy in handling time-series data. The results of ten-fold cross-validation on two datasets show that the classifier may be effectively used to detect gear problems. Nonetheless, in their work for detecting gear faults, they only consider one 1D signal type. In addition, the datasets in this research are small. Further, in [104], a novel method for identifying pitting defects in gears was presented. The presented system was built on top of dictionary learning with a sparsely encoded network of autoencoders. The diagnosis of system failures makes use of sparse dictionary coding as an extraction method. In order to find gear pitting problems, the offered technique uses a stacked auto-encoder network to perform dictionary learning for automated feature extraction from raw vibration data. Several experiments on gears in gearboxes are reported, and the results are compared to contemporary DL approaches for interpreting vibration data. In addition, X. Wang et al [105] suggested an alternative method for bearing failure diagnostics that uses 1D convolutional neural networks (CNNs) to extract characteristics from data obtained by merging vibration and sound inputs. This is done to make the system more bulletproof than it would be with a single-sensor approach. In contrast, X. Li et al [106] have used the vibration signal at varying speeds to identify early gear pitting problems under a variety of working situations. The suggested technique makes use of channel convolution in conjunction with point-by-point convolution to cut down on the required number of network parameters. The approach uses a separable convolution paired with a residual link network to determine the importance of the research in relation to similar prior efforts. In addition, Yao et al [107] reported a DL-based gear fault diagnosis strategy that uses sound signal analysis to identify gear failures. To make use of signals in both the temporal and frequency domains, a CNN may be constructed using an end-to-end design. Furthermore, the CNN may be used in conjunction with multichannel audio sensing without resorting to any extra fusion methods. In comparison to more traditional gear failure diagnostic procedures based on function engineering, the suggested methodology has substantially higher efficiency, as shown by the experimental results. For the purpose of gear malfunction diagnosis, an open-source sound signal database is also released. Yet only one kind of signal is discussed in the two research [104, 107].

2.5 Literature Review Summary

In mechanical systems, vibration caused by friction is a factor that prevents higher precision and efficiency from being achieved. Some industries have been tormented for years by friction-induced sound and vibrations, such as braking, bearing squeals, and chatter in machine tools. However, there is no explanation or remedy that is widely acknowledged for this problem. Up until fairly recently, friction-induced vibrations were seen only as a result of friction, with no consideration given to the crucial interaction of the friction force with the vibrations of the dynamical systems. This treatment was carried out without taking into account the vital interaction. There is a large amount of feedback between the friction force and the vibratory response of the system. The friction force created between two bodies in sliding contact is very much reliant on the vibrations that are produced as a consequence of the contact.

The aforementioned studies have their own set of problems and restrictions. They were all based on a single potential kind of signal. Some of them have considerable computational complexity, which is a problem for real-time applications, while others utilize datasets that are often small, resulting in unreliable techniques. Finally, most of them can only identify faults; they cannot assess fault severity.

Thus, this research focuses on vibrations caused by dry friction between meshing teeth, as well as the mechanics of friction force in relation to surface deformation, which has never been completely investigated previously. Then it will be used to modify a numerical dynamic gear model to imitate an experimental gearbox setup.

Furthermore, a robust machine learning technique will be used by combining EMD-PCA with image processing and then feeding the resultant spectrogram pictures into a 2-Dimensional convolutional neural network. Furthermore, a novel approach to utilizing the residual time domain signal in machine learning is used, in which the signal is treated as a black-and-white image, which is then entered into a 2-Dimensional convolutional neural network—and then using both models to perform a multilabel classification image processing to detect cracked teeth in spur gears by utilizing the data from the numerical model that will be developed in the first part of the study.

CHAPTER 3: THEORETICAL AND NUMERICAL DEVELOPMENTS

This chapter describes the proposed research framework for examining the vibration response of a one-stage gearbox in the presence of crack imperfections at one of the two spur gears.

3.1 Gear Modeling and Cracks Geometries

As part of this research, the stiffness of the gear mesh was determined using a finite element model. Firstly, geometry data from the MATLAB code was used to design a 3D model of the gear. The tooth was then modeled as a non-uniform beam and subjected to a "Static" study using finite element simulation in SolidWorks. Just as with the manufactured gears, the linear-elastic parameters of the underlying material were input. According to [108], a single tooth's stiffness may be determined by applying a force to one side of the tooth along the line of action, as shown in Figure 22, and then using the simulated deflections x and y to determine the direction of the force.

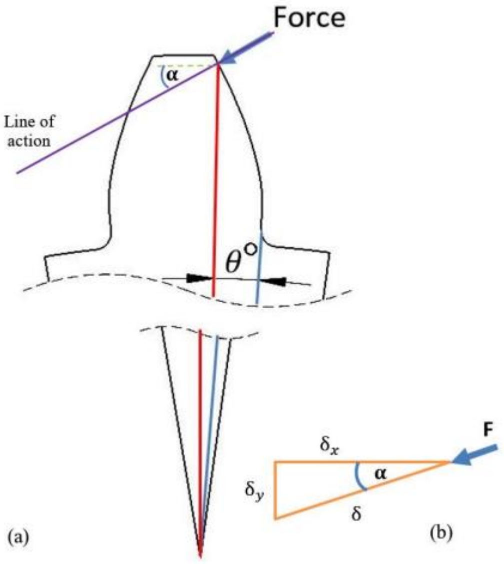

Figure 22: (a) normal to the tooth face and parallel to the line of action, and (b) resolving the displacement components of the transmitted force [109]

A parametric study of twenty-five different points on the tooth face was performed to find the maximum stiffness along the tooth involute.

Tooth deflection is measured in both the X and Y axes at each point because the force exerted on the tooth surface is split into these two components, F_x and F_y, along the X and Y axes, respectively. To determine the overall force-along-deflection, the following equations are used:

$$\delta_i = \sqrt{X_i^2 + Y_i^2} \tag{12}$$

And according to hook's law, the tooth stiffness at each angular position can be calculated from Equation (13):

$$K_i = \frac{F}{\delta_i} \tag{13}$$

The involute profile is the tooth shape that is used the vast majority of the time in modern power transmission gears. Involute gears are simple to produce, and their gearing has a characteristic that permits smooth meshing even when there is a degree of misalignment between the center distances of the gears in question. The use of involute gears resulted in a significant improvement in the quality of mechanical transmission. This improvement was essential to the ongoing increase in the operational speed and power of a variety of machines. As a result of this reason, the involute gear profile will be taken into consideration in this inquiry.

As a fracture widens and spreads further within the tooth width, usually speaking, two distinct propagation routes are taken into consideration. This is shown in Figure 23. The first potential outcome, which is shown by the color red, is a direct course in which the fracture spreads through the tooth itself, moving from one face to the other and between two different root positions. In the second potential outcome, which is shown by the blue markings, the fracture spreads through the rim at an angle of thirty-five degrees. Since CL represents the actual length of the crack, and PL represents the complete route along which the fracture has extended, Equation 14 can be used to get the CLP% as follows:

$$CLP = \frac{CL}{PL} \times 100 \tag{14}$$

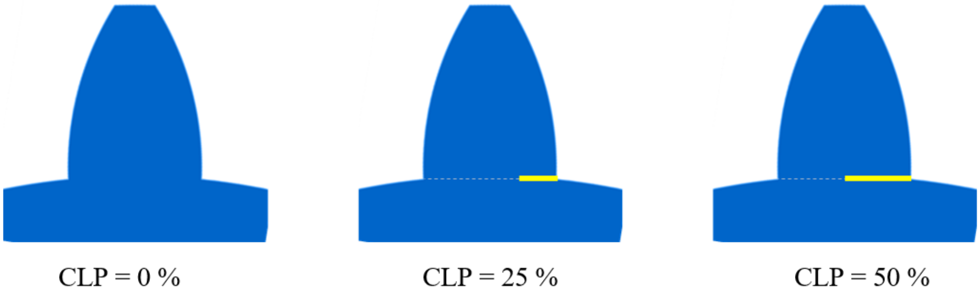
CLP = 0 %

CLP = 25 %

CLP = 50 %

Figure 23: Crack propagation details: straight and deviated paths

Figure 24 shows a scatterplot of tooth stiffness vs. the angle of the force site for both healthy and damaged gear, with both variables translated into dimensionless forms:

- The Stiffness Ratio, denoted by the notation (SR) and defined as $\left[\frac{K_i}{K_{max}}\right]$, is the relationship between K_i the stiffness at location i, and the maximum stiffness K_{max}.

- The angle ratio, denoted by the notation (AR) and defined as $\left[\frac{\theta_i}{\theta_{max}}\right]$, is the relationship between θ_i the angle at position i, and the overall angle of the tooth profile θ_{max}.

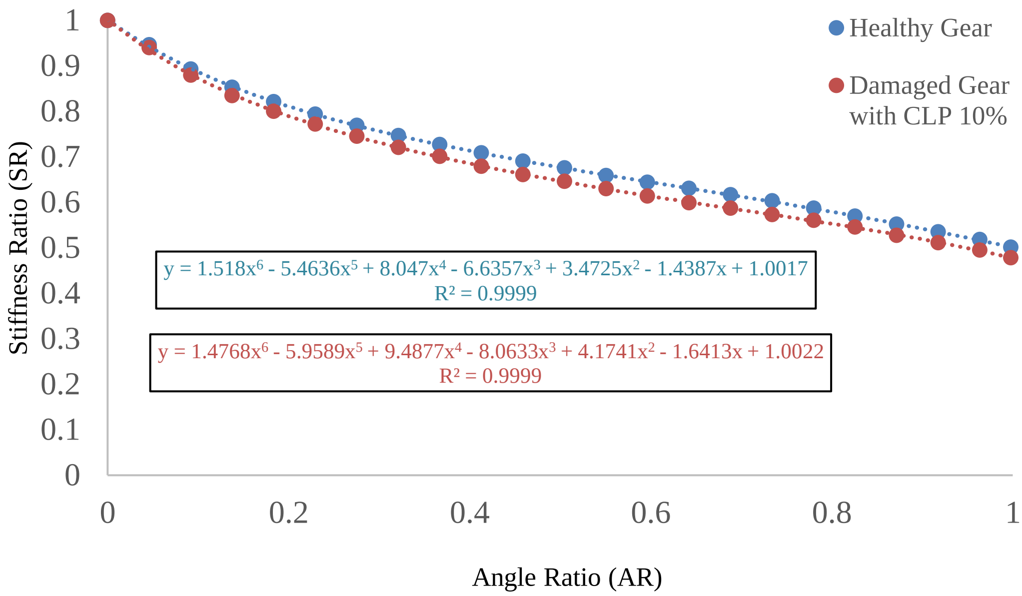

Figure 24: Stiffness Ratio (SR) vs. Angle Ratio (AR) for healthy and damaged gear with CLP = 10%

It is abundantly evident that the stiffness will decrease as the angle that exists between the contact point and the bottom point at the beginning of the involute curve increases. This occurs as a result of an increase in the distance that is measured in a perpendicular direction between the base of the tooth and the place at which the force is being applied. Depending on the number of teeth and their respective geometries, the contact nature periodically varies between one and two points in a period of gear revolution. Analysis of the contact between the teeth is an essential step in any dynamic analysis. Knowing how many points are in contact and how long the teeth are in contact is vital information for determining the gear mesh stiffness. For typical gear parameters given in Table 1, and using the polynomial equations displayed in Figure 24, a MATLAB program was developed to obtain the numerical values of the total effective mesh stiffness as a function of the gear rotation angle.

Table 1: Gear Mechanical And Physical Parameters

Parameter	Pinion	Gear
Number of teeth	20	20
Base Radii of pinion and gear (mm)	56.3816	56.3816
Masses of pinon and gear (kg)	1.7802	1.7802
Exerted torque (N.m)	50	60
Gear type	Standard involute (Full-Depth Teeth)	
Pressure angle (degree)	20	
Face width (mm)	20	
Module (mm)	6	
Elastic modulus (N/m^2)	2 x 10^{11}	
Poisson’s ratio	0.29	
Contact ratio	1.63	
Crack thickness (mm)	0.2	
Crack width (mm)	Percentage of tooth width	
Input shaft frequency (Hz)	12.5	
Meshing frequency (Hz)	250	
Coefficient of friction	0.06	
Radial stiffness of bearings (N/m)	6.65 x 10^8	
Damping coefficient of bearings (N.s/m)	1.8 x 10^3	

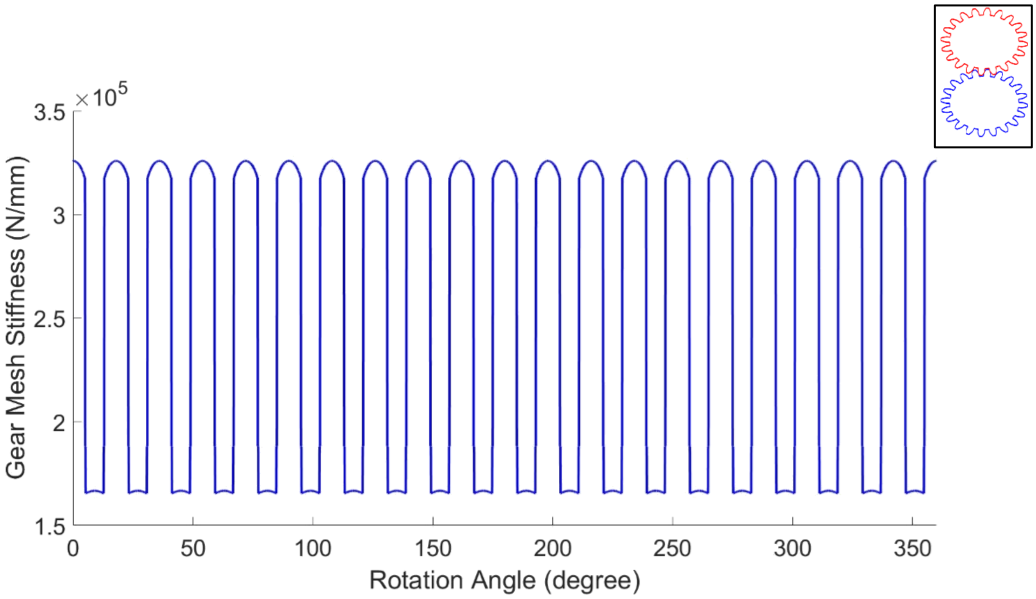

Figure 25: Time-varying mesh stiffness for a healthy gear

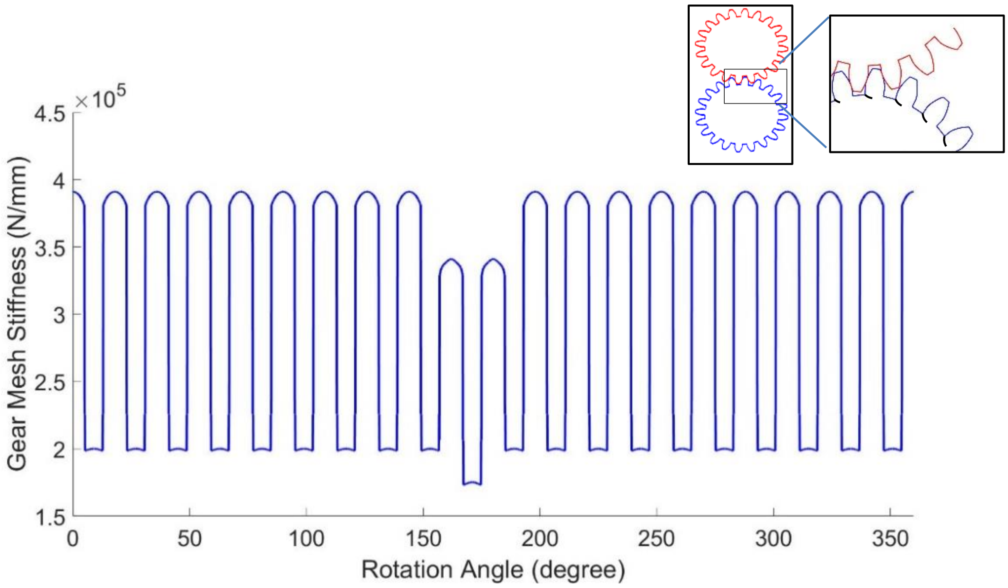

Figure 26: Gear mesh stiffness for a crack on the gear's 10th tooth of CLP = 30%

Figure 25 depicts the stiffness of a healthy pinion, while Figure 26 depicts the stiffness of a damaged gear with a crack length percentage of 30% (Tooth No.10). It is concluded that when the CLP increases, the gear mesh stiffness reduces.

3.1.1 Numerical Model Validation

A comparison was made between these findings and the literature presented in [72]. Kurtosis values (applied on the residual signal) generated by the code, as seen in Figure 27, were compared with those reported in [72] shown in Figure 28. The indicator values were normalized to the healthy signal. Figure 29 shows that the values and trends of the produced curves are quite similar to those reported in the literature, which validates the model.

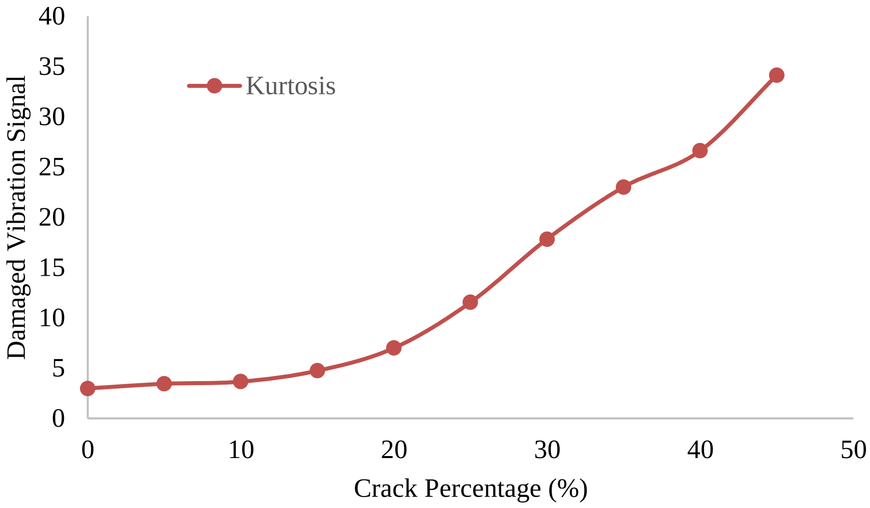

Figure 27: Kurtosis values of the model

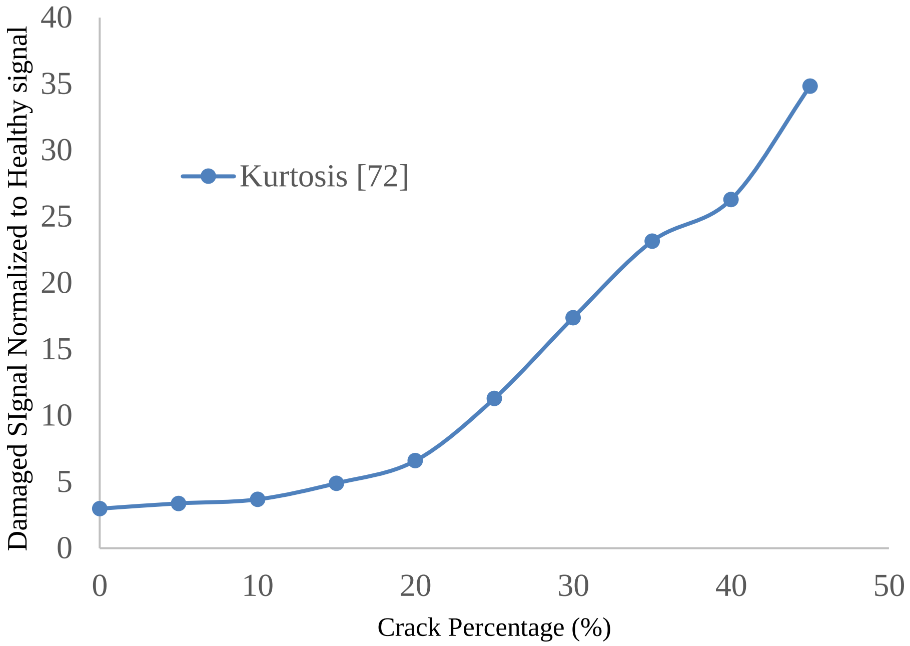

Figure 28: Kurtosis values from [72]

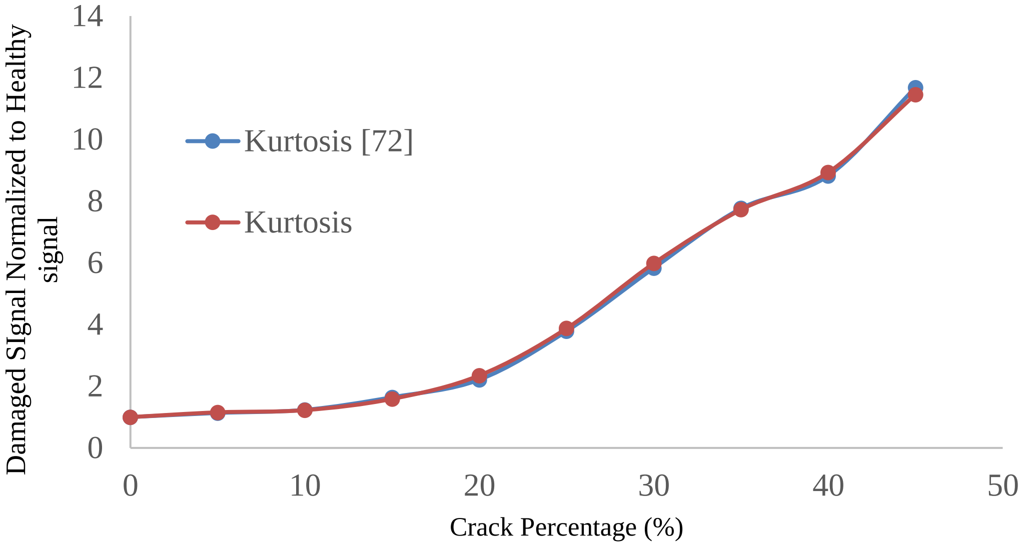

Figure 29: Comparison between normalized Kurtosis values from code and [72]

3.2 Vibration Response

The structure diagram of the gear-rotor-bearing transmission system is shown in Figure 30. This is an elementary one-stage gearbox, where two spur gears are mating together. Each one of the shafts supporting the gears is itself supported by two ball bearings. The shafts are also assumed to be short and consequently rigid enough to create any bending possibly. The lumped parameter model adopted in this paper consists of 6 degrees of freedom (DOF), which has been adopted in research [110]. It takes into consideration the torsional (θ) and lateral vibration in both the x and y directions, respectively. The coordinate system was chosen in this model such that one of the axes (the y-axis) was parallel to the line of action, whereas the x-axis was perpendicular to the line of action. The model simplifies the gear system and ignores the transmission error between gears, shaft deflection, and side deformation of the gearbox shell. The gearbox casing is supposed to be perfectly rigid.

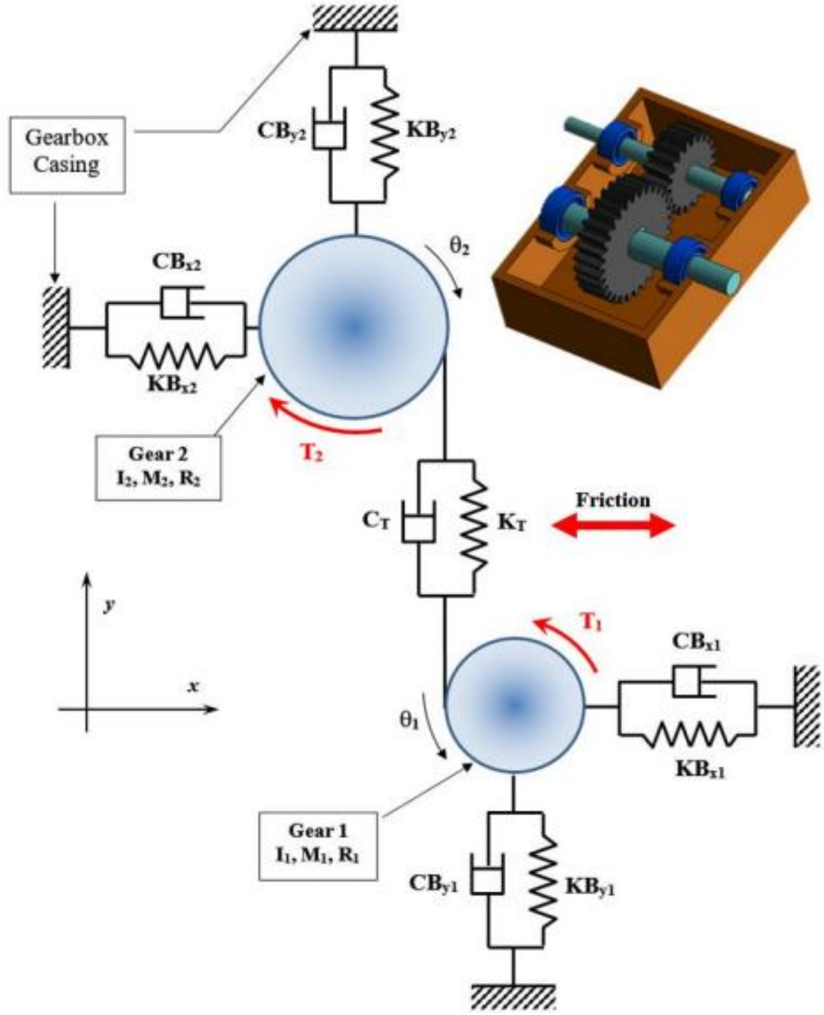

Figure 30: One-stage six DOF gearbox dynamic mode [110]

The governing differential equations of the dynamic system can be written as follows:

$$m_1\,\ddot{x}_1 = F_1 - KB_{x1}\,x_1 - CB_{x1}\,\dot{x}_1 \tag{15}$$

$$m_2\,\ddot{x}_2 = F_2 - KB_{x2}\,x_2 - CB_{x2}\,\dot{x}_2 \tag{16}$$

$$\begin{aligned} m_1\,\ddot{y}_1 = -KB_{y1}\,y_1 - CB_{y1}\,\dot{y}_1 + K_t\,(R_{b1}\,\theta_1 - R_{b2}\,\theta_2 - y_1 + y_2) \\ + C_t\left(R_{b1}\,\dot{\theta}_1 - R_{b2}\,\dot{\theta}_2 - \dot{y}_1 + \dot{y}_2\right) \end{aligned} \tag{17}$$

$$\begin{aligned} m_2\,\ddot{y}_2 = -KB_{y2}\,y_2 - CB_{y2}\,\dot{y}_2 + K_t\,(R_{b1}\,\theta_1 - R_{b2}\,\theta_2 - y_1 + y_2) \\ + C_t\left(R_{b1}\,\dot{\theta}_1 - R_{b2}\,\dot{\theta}_2 - \dot{y}_1 + \dot{y}_2\right) \end{aligned} \tag{18}$$

$$I_1\,\ddot{\theta}_1 = M_1 + T_1 - R_{b1}\,K_t\,(R_{b1}\,\theta_1 - R_{b2}\,\theta_2 - y_1 + y_2) - R_{b1}\,C_t\left(R_{b1}\,\dot{\theta}_1 - R_{b2}\,\dot{\theta}_2 - \dot{y}_1 + \dot{y}_2\right) \tag{19}$$

$$I_2\,\ddot{\theta}_2 = M_2 - T_2 + R_{b2}\,K_t\,(R_{b1}\,\theta_1 - R_{b2}\,\theta_2 - y_1 + y_2) + R_{b2}\,C_t\left(R_{b1}\,\dot{\theta}_1 - R_{b2}\,\dot{\theta}_2 - \dot{y}_1 + \dot{y}_2\right) \tag{20}$$

Table 2: Descriptions Of Variables Used In The Equations Of Motion

Variable	Description
m_1, m_2	Masses of pinion and gear
I_1, I_2	Mass moments of inertia of pinion and gear
R_{b1}, R_{b2}	Base circles radii of pinion and gear
KB_{x1}, KB_{x2}	Horizontal radial stiffnesses of input and output bearings
KB_{y1}, KB_{y2}	Vertical radial stiffnesses of input and output bearings
CB_{x1}, CB_{x2}	Horizontal radial viscous damping coefficients of input and output bearings
CB_{y1}, CB_{y2}	Vertical radial viscous damping coefficients of input and output bearings
F_1, F_2	Friction forces applied on the pinion and gear
M_1, M_2	Friction moments applied on pinion and gear
T_1, T_2	Input and Output torques
K_T	Teeth mesh stiffness
C_T	Teeth mesh damping coefficient
x_1, x_2	Linear displacements in the x-direction for pinion and gear
y_1, y_2	Linear displacements in the y-direction for pinion and gear
θ_1, θ_2	Angular displacements of pinion and gear

Symbols with one or two dots in the previous Equation (15-20) represent the first and second derivatives with respect to time. For example, $\dot{x}$ and $\ddot{x}$ Represent velocity and acceleration in the x direction, respectively. The solving of the set of previous equations was executed in MATLAB, and the ode45 function was used. This function implements a Runge-Kutta method with a variable time step for efficient computation. The method in the solving process. The duration size and the sampling frequency in solving the equations are set up as 0.08s, which is exactly one period, and 140.725k Hz, respectively. Figure 98 displays examples of the time waveform data for a healthy case.

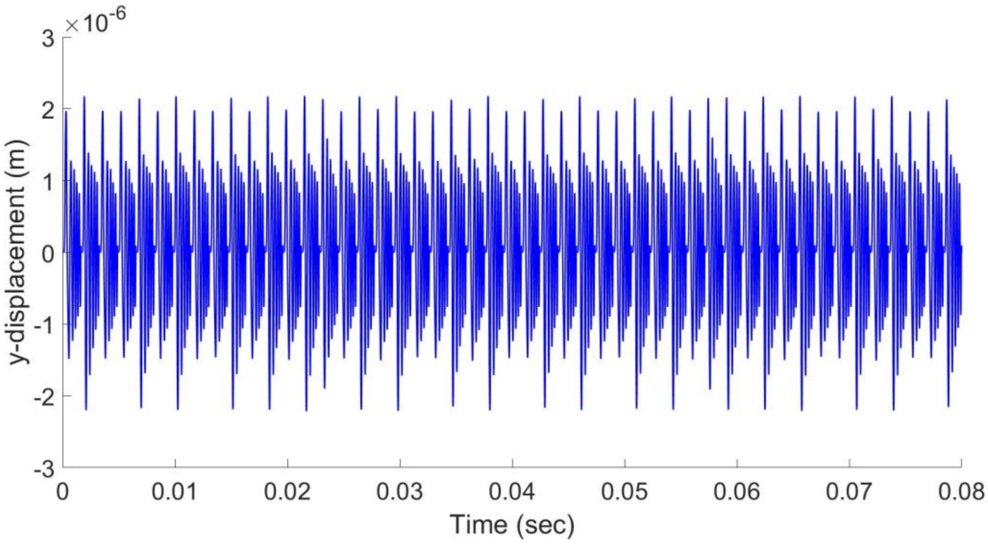

Figure 31: Time response signal for a healthy gear

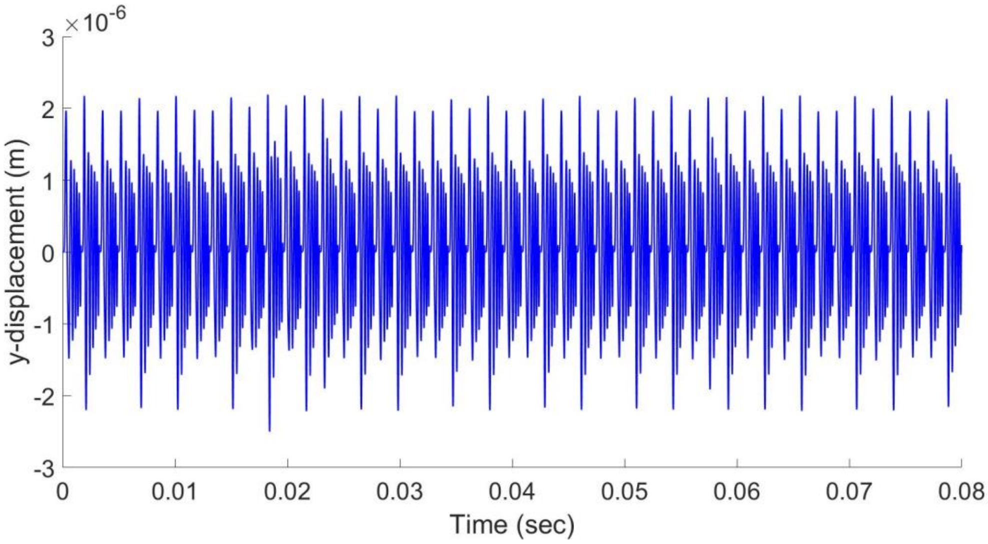

Figure 32: Time response signal for a damaged case of CLP = 10%, at tooth No. 5.

3.3 Friction-Induced Vibration Development

The complex issues in contact mechanics, tribology, and nonlinear dynamics at the nano-, micro-, and macro-scales make modeling friction-vibration interactions a difficult multi-disciplinary topic. Frequency ranges from the tens of hertz to the ultrasonic are of interest in the friction-induced vibration interaction issue, together with time-varying boundary conditions and large spatial and temporal dimensions.

Experiments and theoretical investigations have shown that friction in a working mechanical system may be the cause of vibration and AE, which are often unwelcome. In order to calculate the AE characteristics that come along with solid-on-solid contact friction, Barnov et al. [111] created a simple model. Their hypothesis states that the following equation defines the AE amplitude:

$$Amp(AE) = K_{AE}\, V^{1/2}\, P^2 \tag{21}$$

Where K_{AE} is a constant, V is the velocity of the surface sliding motion, and P is the pressure on the surface of contact asperities. Because random vibration and AE are both by-products of the same friction phenomenon, one can suppose that the friction-induced vibration generated when one tooth makes contact and rubs against another, the other one obeys similar rules with one extra term counting for the random behavior. The amplitude of such noisy-type vibrations could be expressed by a law of the form:

$$Amp(Random\,Vibration) = K_N\ V^{1/2} \left(\frac{F}{A}\right)^2 Randn(t) \tag{22}$$

Where K_N is a constant, V is the relative slip speed between mating teeth, F is the loading value transmitted between the teeth in the perpendicular direction to the contacting surface, A is the Hertzian contact surface, and Randn(t) is a function of time that generates normally distributed random numbers.

3.3.1 Line of Action Development

The line of action is the common tangent line that connects the base circles of two involute gears that are in contact with one another. Contact is made on the line of action when two involute gears are meshing with one another, and the contact point moves along the line of action. Taking two points at different locations along the line of action will allow you to calculate the equation that describes that line. As a result, when two gears are working together, the line of action will be tangent to both gears' base circles. Assuming Gear 2 is being driven while Gear 1 is rotating in the other direction, counterclockwise. Thus, to calculate the coordinates of the two points that make up the line of action, the following equations that rely on the pressure angle and the base radii of the two gears were used:

Coordinates of the first point

$$x_1 = \sin(\phi) \cdot Base\ Radius(Gear1) \tag{23}$$

$$y_1 = \cos(\phi) \cdot Base\ Radius(Gear1) \tag{24}$$

$$x_2 = -\sin(\phi) \cdot Base\ Radius(Gear2) \tag{25}$$

$$y_2 = \text{Center distance} - \cos(\phi) \cdot Base\ Radius(Gear1) \tag{26}$$

To find the equation of a line between two points

$$y = m \cdot x + c \tag{27}$$

Where m is the slope of the line and c is the y-intercept:

Since:

$$slope\ of\ the\ line, m = \frac{y_2 - y_1}{x_2 - x_1} \tag{28}$$

and,

$$y_{intercept}, c = y_1 - \left[x_1 \cdot \frac{y_2 - y_1}{x_2 - x_1}\right] \tag{29}$$

Hence, the equation of the line of action becomes:

$$y = \left(\frac{y_2 - y_1}{x_2 - x_1} \cdot x\right) + \left(y_1 - \left[x_1 \cdot \frac{y_2 - y_1}{x_2 - x_1}\right]\right) \tag{30}$$

By solving Equations (23-27) and implementing values in Equation (30), the line of action between the two meshed gears is plotted in Figure 33.

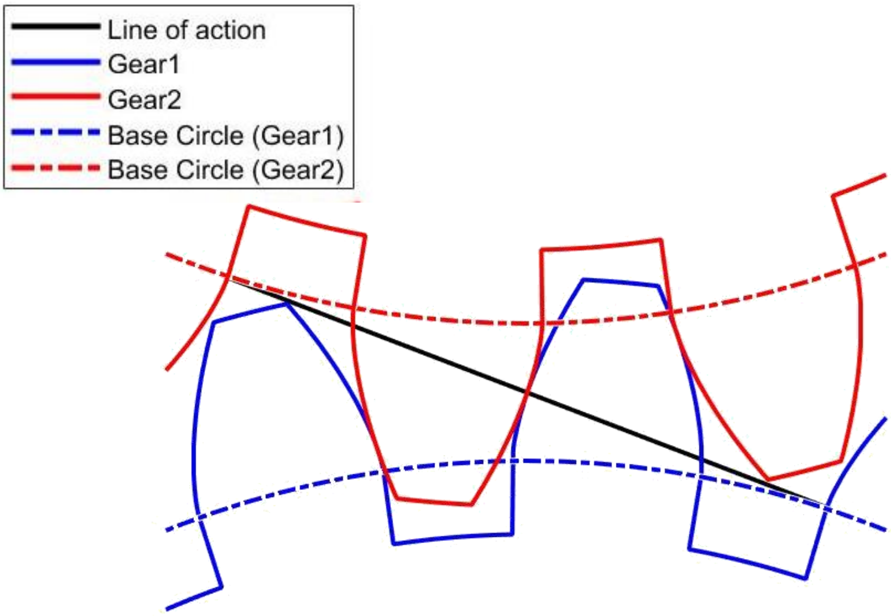

Figure 33: Line of action between two meshed gears

3.3.2 Path of Contact Development

The path of contact refers to the path that is traced by the point of contact between two teeth profiles, and it is found by the intersection points between the line of action and two vectors having one of their starting points at the center of the gears, as shown in Figure 34.

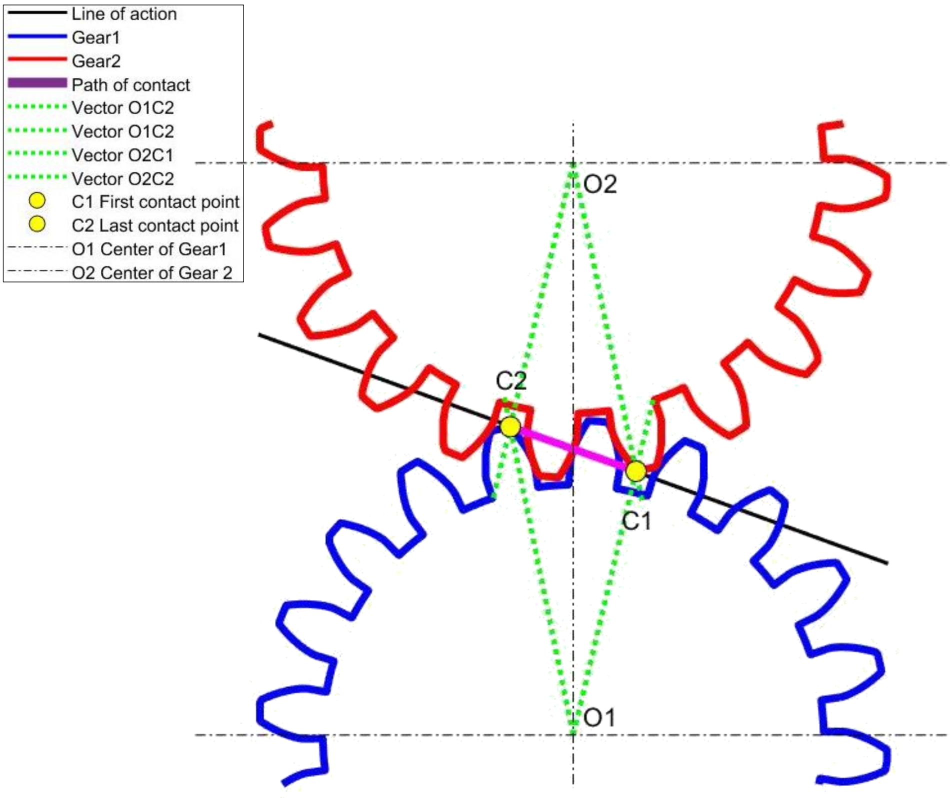

Figure 34: Path of contact engulfed by the first and last points of contact

By using Equations (23-27,30), between C1 and C2, the path of contact is found and is then divided into 392 contact points based on the geometrical limitations to construct the total number of contact points between the gears.

3.3.3 Hertzian Area of Contact Development

Under the mutual contact between two mating teeth, there is a local deformation, and its area could be estimated by the ISO 6336 standard [112]. The theory included in that standard offers mathematical formulas for the stresses and deformations that occur when curved bodies come into contact with one another. It contains the essential equations for Hertzian contact stress estimates for spur gears, as well as the methods for calculating these stresses. To approximate the contact of gear teeth flanks, two parallel cylinders with radiuses equivalent to the radius of the curvatures of the teeth flanks may be brought into touch at the contact site, shown in Figure 35.

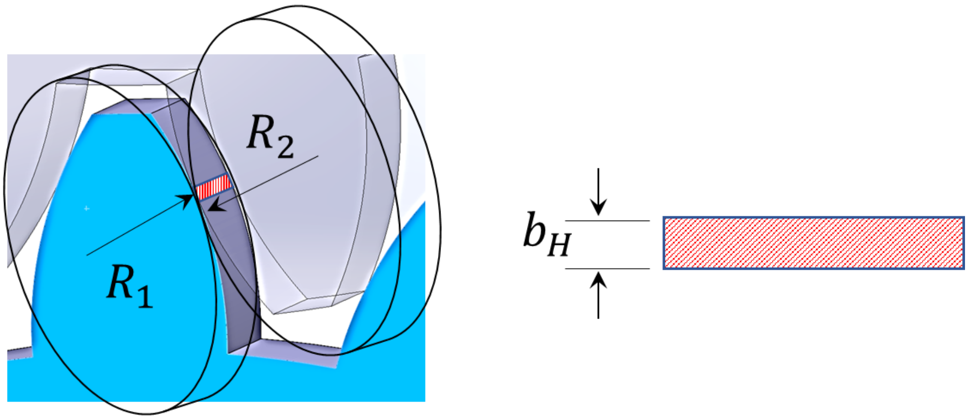

Figure 35: Explanation of the Hertzian contact region

The Hertz theory of contact requires prior knowledge of the curvature radius of each one of the bodies in contact in order to estimate the size of their mutual contact area. During teeth meshing, the location of the contact point is not the only variable. Indeed, the teeth radii of curvatures at both sides of contact are also variable. At each one of the contact points, while one curvature is increasing, the other one is decreasing, and vice versa. Therefore, a geometric circle fitting method based on the standard Lavenberg-Marquardt [113] scheme is used to estimate the curvatures by considering a set of points before, after, and around the contact point. This approach is described in Figure 36.

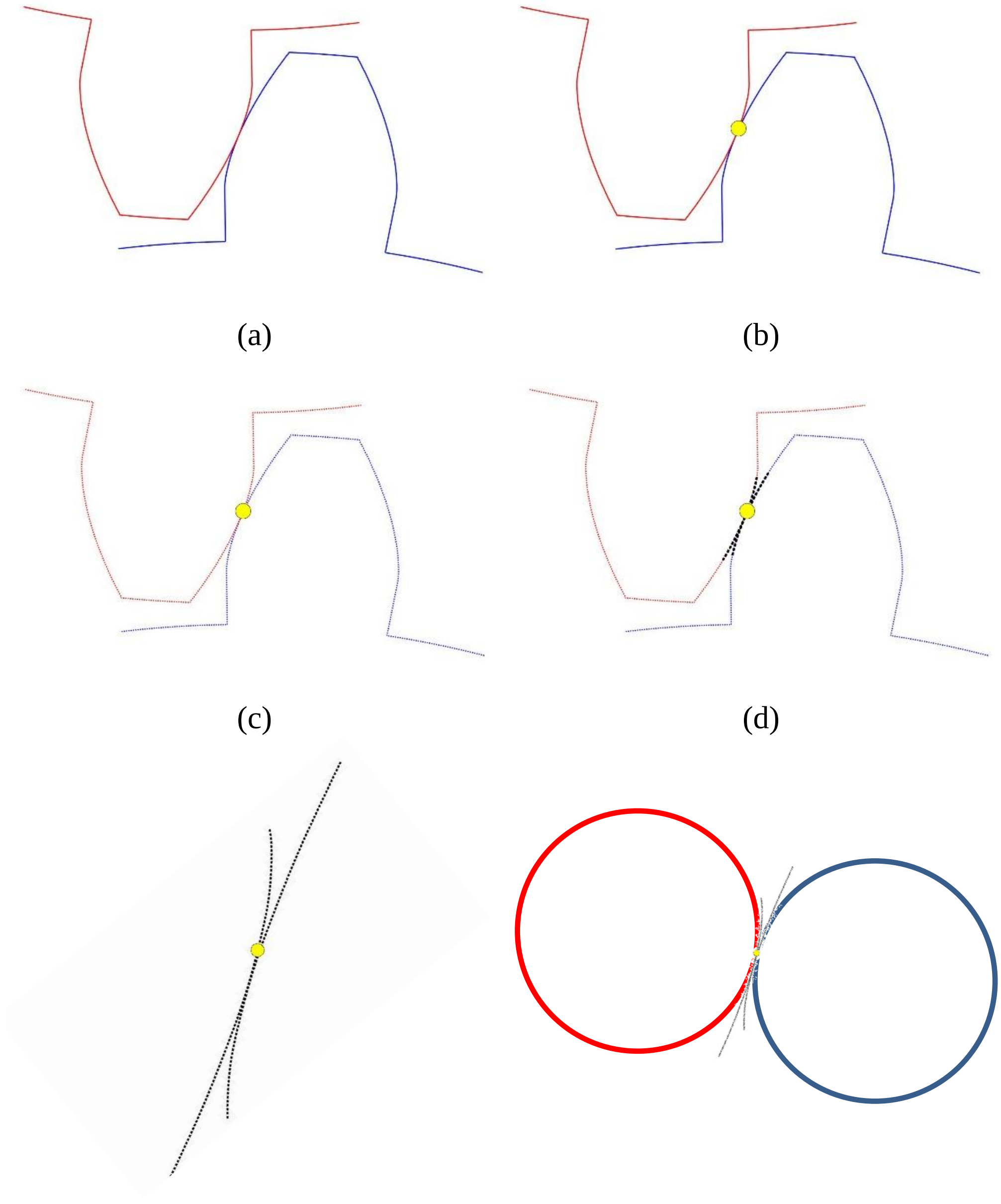

(a) (b)

(c) (d)

(e) (f)

Figure 36: Approach of finding the Hertzian curvature circles radii

The approach of approximating the Hertzian radii of the gear and pinion described in Figure 36 starts with Identifying the teeth in contact in Figure 36. a, then Figure 36. b describes finding the point of contact between the meshed teeth. Figure 36. c shows the conversion of the involute curve into separate points. Figure 36.d describes the creation of the number of points before and after the contact point. Figure 36. e shows the estimated points that will be used standard Lavenberg-Marquardt circle fitting method, and Figure 36. f shows the approximated circles found by the Lavenberg-Marquardt method.

By using the involute defining angles shown in Equations (31-37):

$$\theta_0 = 0^o \tag{31}$$

$$\theta_1 = \theta_{pitch} = \tan^{-1}\left(\frac{\sin\left(\sqrt{\frac{R_p^2}{R_b^2}-1}\right) - \sqrt{\frac{R_p^2}{R_b^2}-1}\cdot\cos\left(\sqrt{\frac{R_p^2}{R_b^2}-1}\right)}{\cos\left(\sqrt{\frac{R_p^2}{R_b^2}-1}\right) + \sqrt{\frac{R_p^2}{R_b^2}-1}\cdot\sin\left(\sqrt{\frac{R_p^2}{R_b^2}-1}\right)}\right) \tag{32}$$

$$\begin{aligned}\theta_2 &= \theta_{outer}\\ &= \tan^{-1}\left(\frac{\sin\left(\sqrt{\frac{R_{outer}^2}{R_b^2}-1}\right) - \sqrt{\frac{R_{outer}^2}{R_b^2}-1}\cdot\cos\left(\sqrt{\frac{R_{outer}^2}{R_b^2}-1}\right)}{\cos\left(\sqrt{\frac{R_{outer}^2}{R_b^2}-1}\right) + \sqrt{\frac{R_{outer}^2}{R_b^2}-1}\cdot\sin\left(\sqrt{\frac{R_{outer}^2}{R_b^2}-1}\right)}\right)\end{aligned} \tag{33}$$

$$\theta_3 = (\theta_4 - \theta_1) \tag{34}$$

$$\theta_4 = \frac{360^0}{2\cdot number\ of\ teeth} + \theta_1 \tag{35}$$

$$\theta_5 = \theta_3 + \theta_2 \tag{36}$$

$$\theta_6 = \frac{360^0}{2 \cdot number\ of\ teeth} \tag{37}$$

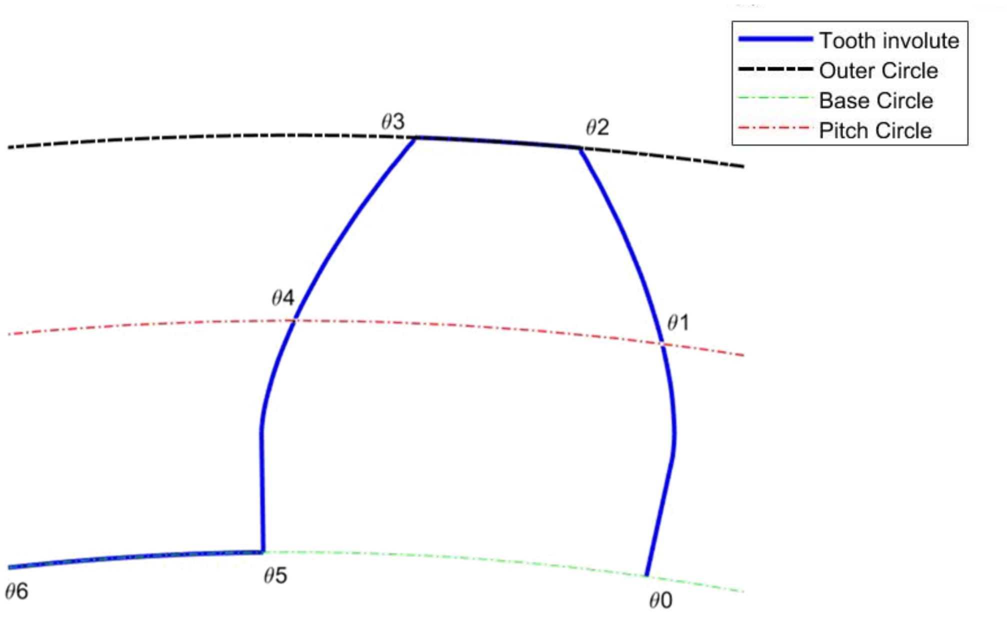

Figure 37: Defining angels of the tooth involute profile

Using the defining angles plotted in Figure 37 and the cartesian coordinates equations that depend on the involute angle, which is denoted by θ, and the radius, R, at which the involute curve makes an intersection, the points before, after, and around the contact points can be found.

Cartesian coordinates equations:

$$x\ (\theta) = R \cdot \sin\ (\theta) \tag{38}$$

$$y(\theta) = R \cdot \cos(\theta) \tag{39}$$

By creating several dotted circles between the base circle and the involute tooth circle, as shown in Figure 38, the defining angles $[\theta_0 - \theta_6]$ can be found at different intersections around the points of contact, which will then act as the arc of points shown in Figure 36. e, that can be used in the geometric circle fitting method to calculate curvature approximating circles.

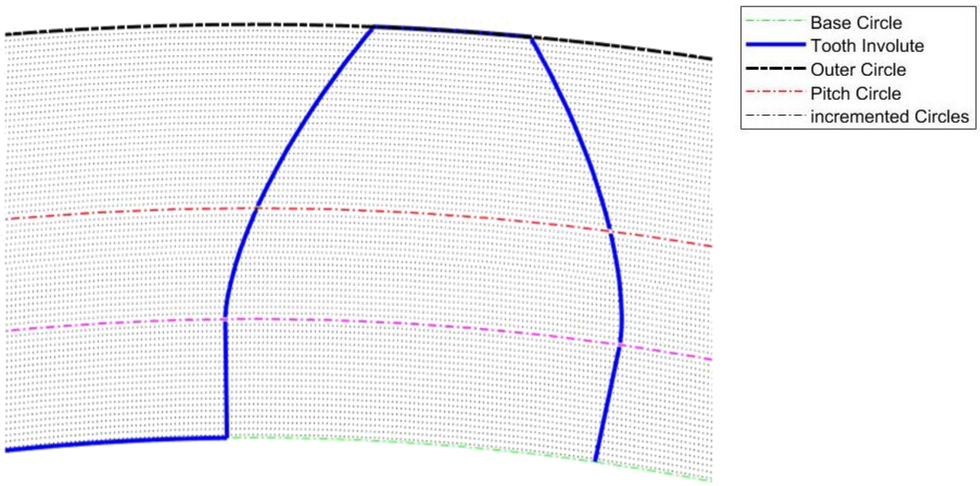

Figure 38: Development of the imaginary radii between the outer and base

Depending on how far the contact location from the intersection between the involute and the pitch circle is, the curvature identification strategy is centered, backward, or forward as seen in Figure 39. Hence, if the two teeth intersect more towards the middle of the involute, a set of 15 points before and 15 points after are considered in the circle fitting calculation process. However, as explained in Figure 39, if the contact is taking place more towards the root (end of the involute) or the head (Beginning of the involute), the points are selected based on their availability.

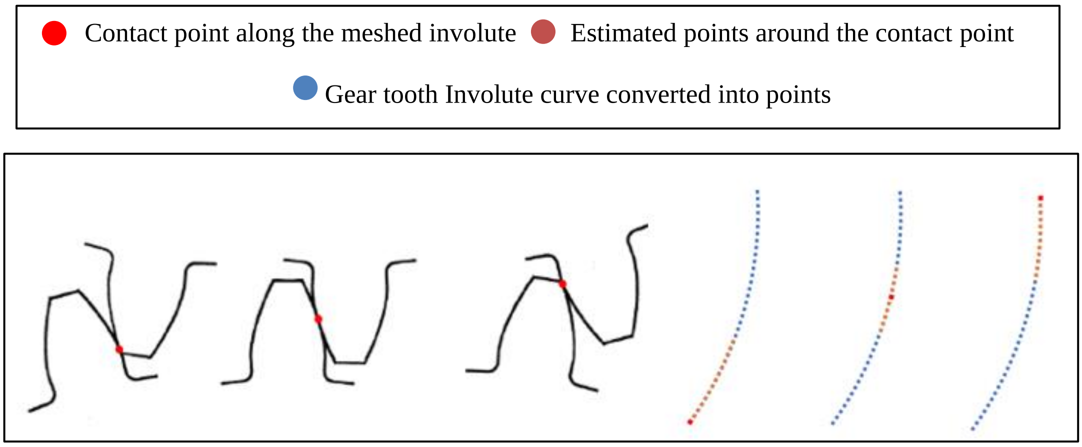

Figure 39: In-contact involute curves constructed from spherical elements at different contact points

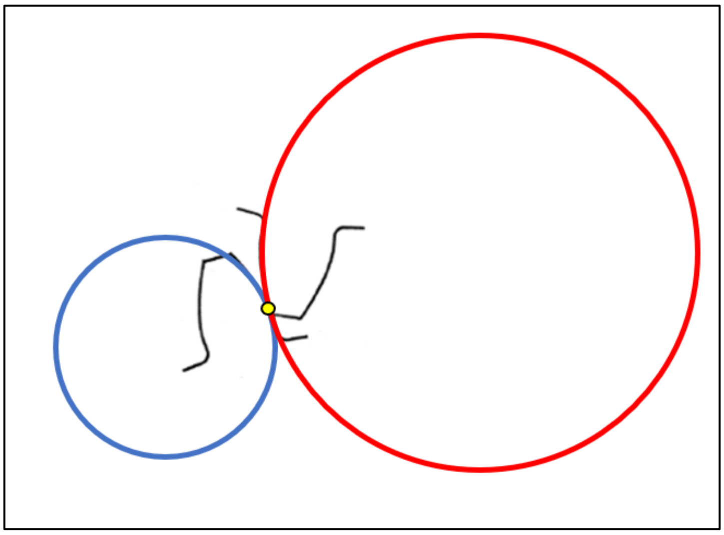

Figure 40: Approximated circles on pinion and gear at the end of contact between the meshed teeth

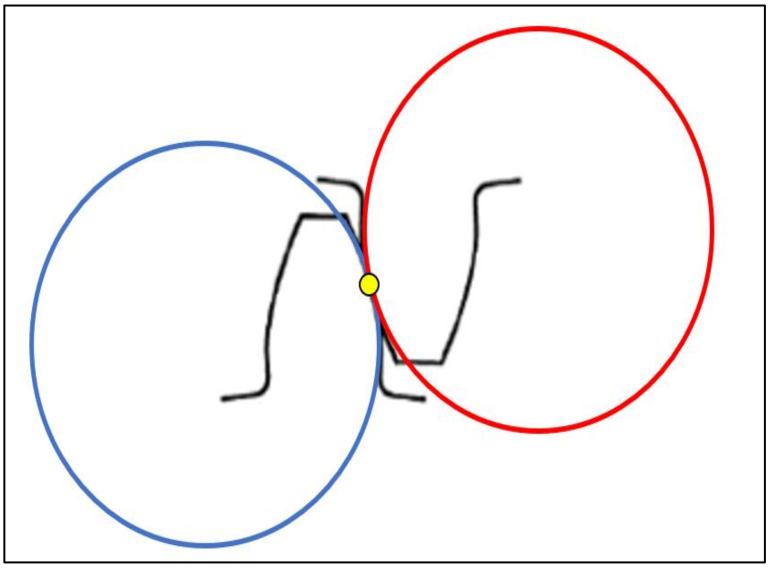

Figure 41: Approximated circles on pinion and gear at the pitch point of contact, where both approximated circles have the same radius

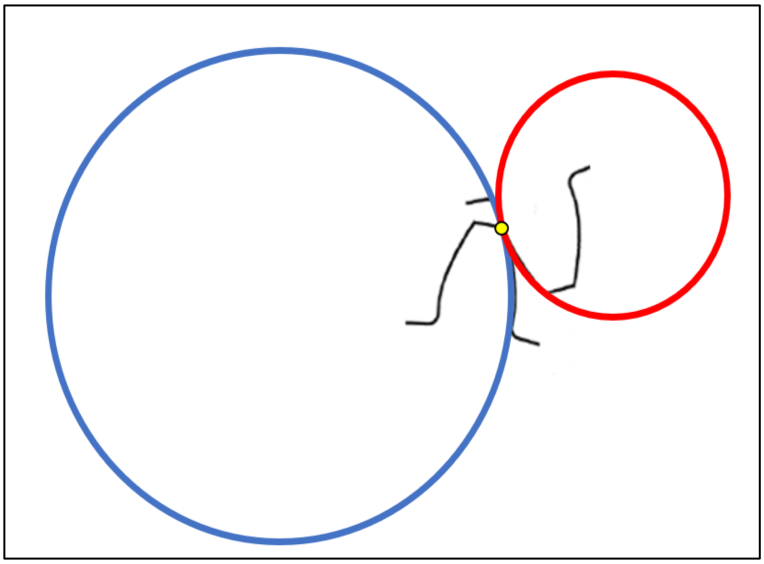

Figure 42: Approximated circles on pinion and gear at the start of contact between the meshed teeth

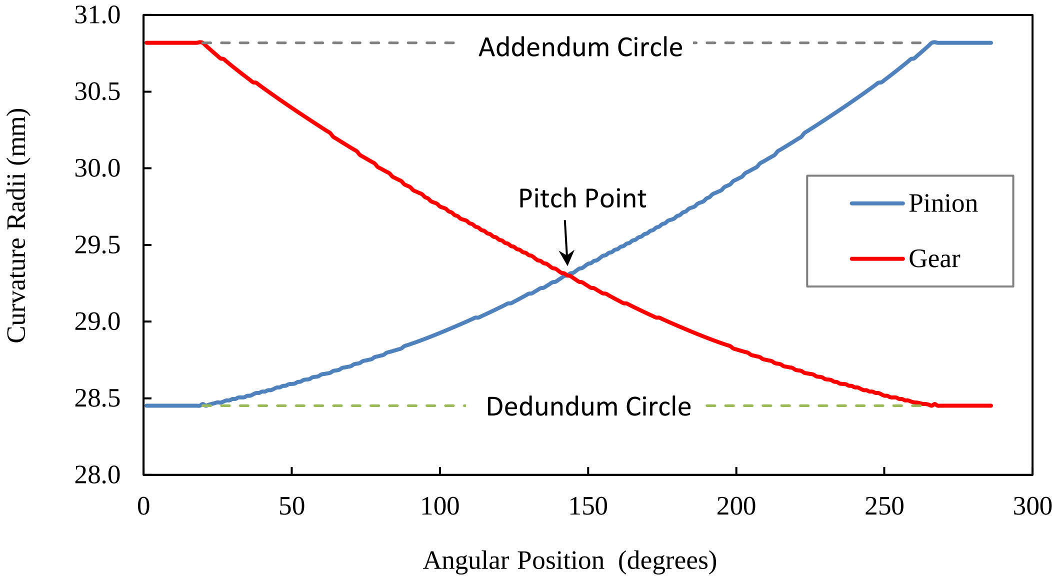

Figure 43: Variation of curvature radii along the line of action

As seen in Figures (40-42), the circles change in size depending on the location of the contact point, and that is seen in Figure 43, as when one gear has the smallest radius value, the other has the highest, and the only point where both gears have the same curvature radii is the pitch point.

3.3.3.1 Calculation of The Hertzian Area

When a basic contact between two surfaces is considered without any roughness, micro-geometry, or edge effect, HERTZ’s theory is applied. In the case of contact between two cylinders with parallel axes Figure 35, the elastically deformed width b_h is obtained according to Equation (40):

$$b_H = \sqrt{\frac{4\,F\left[\frac{1-v_1^2}{E_1}+\frac{1-v_2^2}{E_2}\right]}{\pi L\left[\frac{1}{R_1}+\frac{1}{R_2}\right]}} \tag{40}$$

Where:

R_1, R_2	Curvature radii of gear 1 and gear 2, respectively
E_1, E_2	Modulus of elasticity of gear 1 and gear 2, respectively
ν_1, ν_2	Poisson's ratios of gear 1 and gear 2, respectively
F	Normal force transmitted between teeth
L	Length of contact between teeth

Consequently, the Hertzian area and pressure are given by the following equations:

$$A_H = b_H L \tag{41}$$

$$P_H = \frac{F}{A_H} \tag{42}$$

The Hertzian contact area is shown in Figure 44.

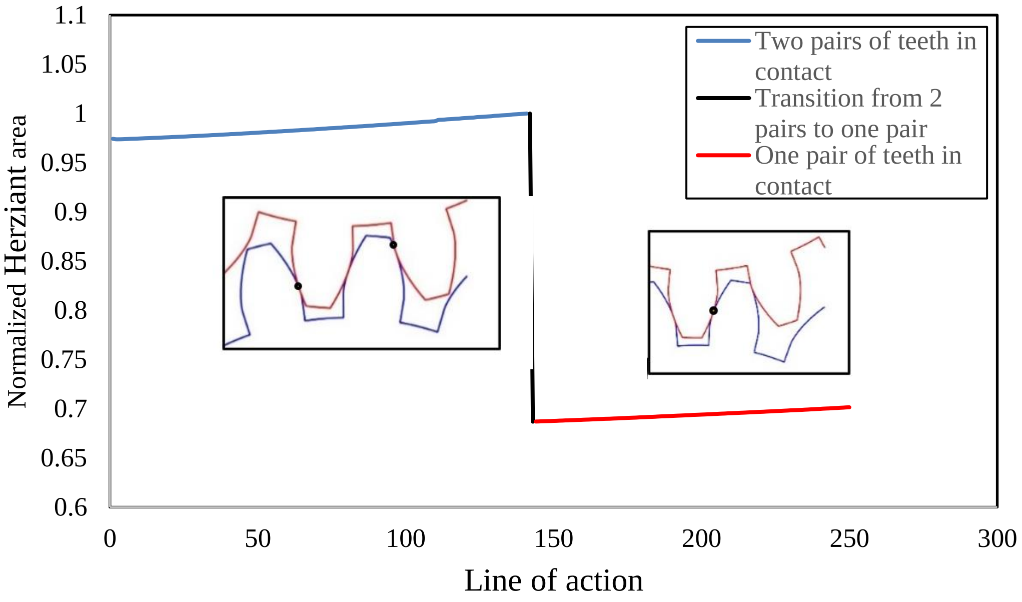

Figure 44: Variation in the Normalized HERTZ's contact area

In Figure 44, it is shown that during the meshing process between teeth belonging to pinion and gear, the elastic deformation area, commonly known as the Hertz contact area, keeps varying along the whole contact path. The sudden jump is due to the transition from single to double contact, as the total effect of the Hertzian contact area is basically the sum of all engaged teeth during

3.3.4 Sliding Velocity Development

As could be seen from previous Figure 43, during the meshing between two opposite teeth, the only position where the radii of curvature are equal is when both teeth touch each other at the junction point of the two pitch circles with the line of action. For any other position, the two radii are different, and their respective linear speeds are different. Consequently, there is a relative sliding between both surfaces. As the contact point goes farther from the pitch point, the sliding speed, defined as the difference between relative speeds, increases proportionally, as shown in Figure 46.

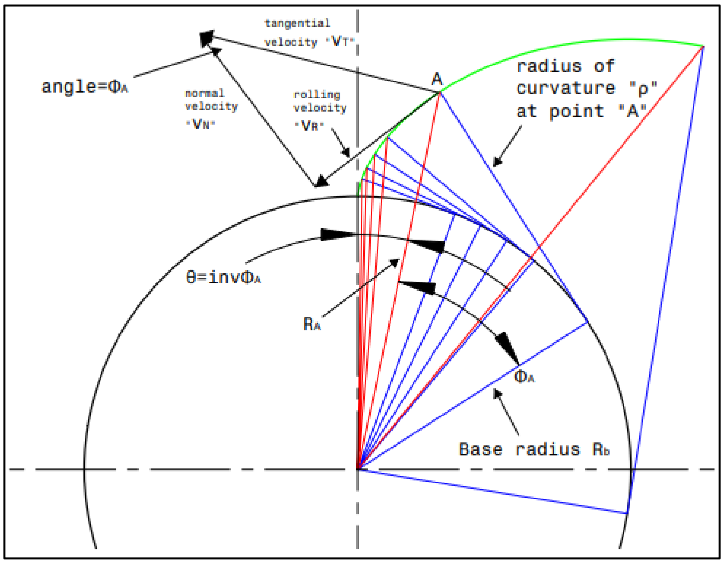

Figure 45: Vectorization of the involute of the gear tooth

As displayed in Figure 45, the velocity vector that is tangent to the circle passing by contact point A is called v_T. If point A is considered to belong both to the pinion and to the gear, both velocities are expressed as follows:

$$v_{TpA} = \frac{2\pi R_{pA}}{60} \times n_p \tag{43}$$

$$v_{TgA} = \frac{2\pi R_{gA}}{60} \times n_g \tag{44}$$

Where:

R_{pA}, R_{gA}	Radii of point A belonging to the pinion and the gear
n_p, n_g	the angular speed of pinion and gear

The rolling velocity component is tangential to the involute curve at any given position.

The angle between the tangent and rolling components at that location is exactly equal to the pressure angle. The relationship between both is expressed as

$$v_{RpA} = v_{TpA} * \sin \phi_A \tag{45}$$

$$v_{RgA} = v_{TgA} * \sin \phi_A \tag{46}$$

The sliding velocity of conjugate spur gear teeth is simply the difference between the rolling velocities of gear and pinion. It may be calculated using the following equation at any arbitrary location on the involute curve.

$$v_s = v_{RpA} - v_{RgA} \tag{47}$$

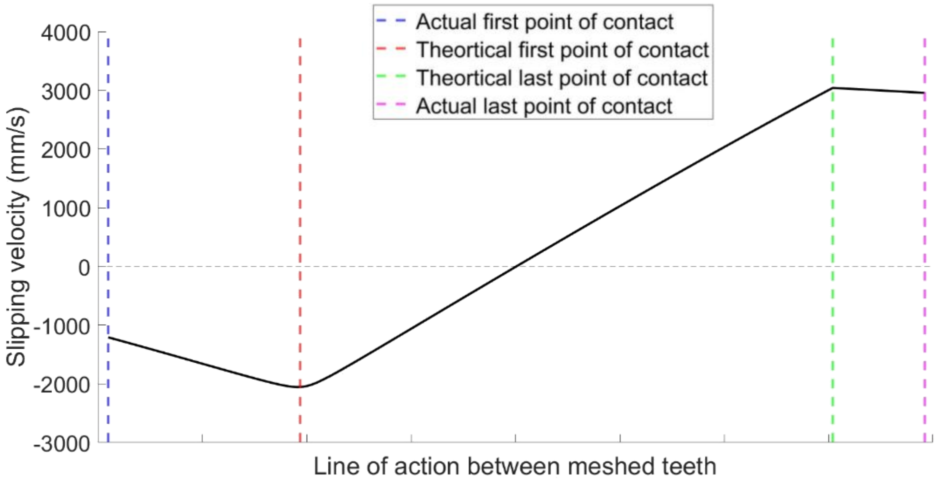

Figure 46: Behavior of the sliding velocity along the line of action

The sliding velocity in Figure 46 demonstrates that as the paired teeth come into contact, the sliding velocity changes until it reaches the pitch point where the difference between the two gears' velocities theoretically becomes zero, meaning that they both rotate at the same speed, and then it keeps increasing till the last point of theoretical contact.

3.3.5 Friction-Induced Response

As previously discussed in chapter 1, sliding one tooth over another is expected to generate a friction-induced random vibration. Such a noisy response is the sum of two components:

- The first component for which the amplitude is modulated is a direct result of the variation of the Hertz elastic contact area Equation (48); Figure 47 shows a typical example of such noise.
- A second component for which the amplitude is constant Equation (49), Figure 48 shows a typical example of such noise.

$$Noise_{modulated}(t) = K_m \times V_s(t)^{\mathbf{1/2}} \times P_H(t)^{\mathbf{2}} \times Randn(t) \qquad (48)$$

$$Noise_{constant}(t) = K_c \times Randn(t) \qquad (49)$$

Where K_m, and K_c Are constants that need to be identified after calibration of the model with experimental measurements, and Randn(t) is a function of time that generates normally distributed random numbers.

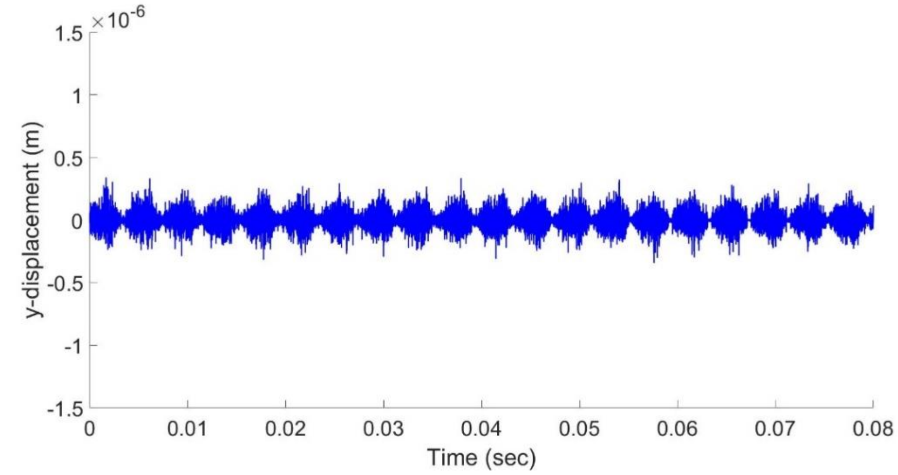

Figure 47: Modulated amplitude noise

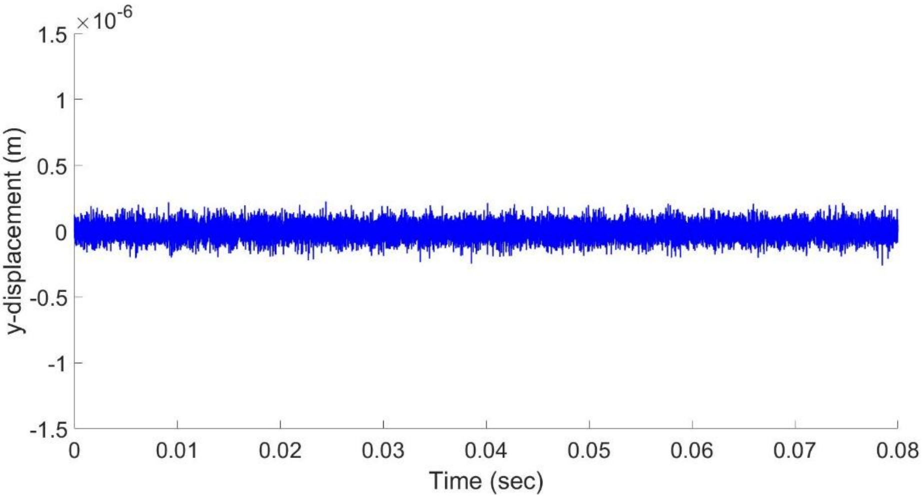

Figure 48: Constant amplitude noise

The total contribution of the noise sources is simply the weighted sum of the two previous expressions.

$$Noise_{total}(t) = \alpha \times Noise_{modulated}(t) + (1-\alpha) \times Noise_{constant}(t) \tag{50}$$

$$Noise_{mod+nor}(t) = 0.6 * Noise_{mod}(t) + 0.4 * \ Noise_{norm}(t) \tag{51}$$

Where: α is the percentage contribution of the modulated noise, and $(1-\alpha)$ is the complementary percentage contribution of the constant noise. The final determination of these contribution values is to be done after the calibration of the numerical model with the experimental measurements. Figure 49 shows a typical example of the addition of both noise contributions.

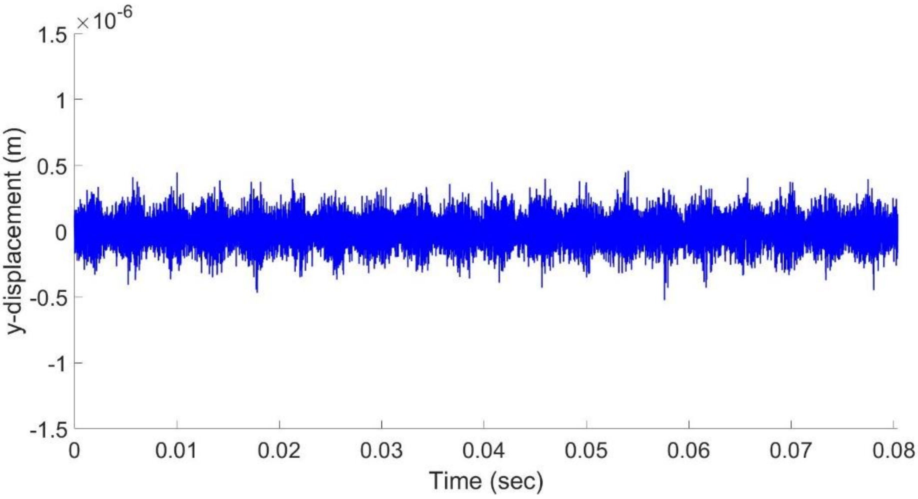

Figure 49: Total (modulated and constant) noise contributions

The modulation effect seen in Figure 49 was produced by modulating the curvature radii of both mating teeth as well as the elastic deformation area at the running sites of contact. The cyclization behavior of gear dynamics has been confirmed by such proved modulation. In terms of industrial applications, the cyclization analysis approach could provide considerable benefits in a variety of industrial contexts. The cyclization analysis can be used to detect wear causes and measure wear severity. The information gained from the cyclization provides engineers with a detailed understanding of the gearbox's current degradation status, assesses the various causes of the degradation, and then makes reliable predictive maintenance-based decisions.

To account for the noise induced by friction, two weighting parameters were developed. One of these weighting parameters is in charge of noise signal attenuation, while the other is in charge of impulsive signal attenuation. Furthermore, these two parameters were calculated by subtracting the simulated RMS and peak values from the empirically determined values. The total gear response is the sum of the periodic impulsive response and the friction-induced noisy vibration after they have been computed:

$$Total\ Response\ (t) = [\ Impulsive\ Response(t) + K_2\ \times Noise_{total}(t)\ ] \times K_1 \qquad (52)$$

Where K_1 and K_2 are weighting coefficients to be assigned when tuning the model with real experimental results. Indeed, as explained in Figure 50, these two parameters will be given appropriate values to make the model generate the same Peak and RMS amplitudes when the gear is free from any cracking defect.

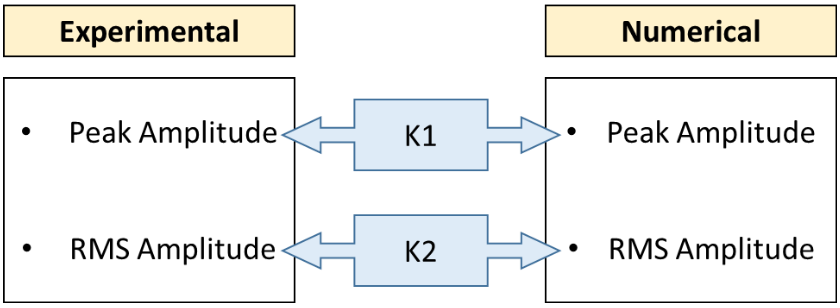

Figure 50: Parameters involved in the calibration of the model with the experimental results

CHAPTER 4: EXPERIMENTAL SET-UP

The experimental setup is broken down, and details on the test rig, data gathering system, damaged gears, and experimental vibration results are collected, as well as their veracity verified.

4.1 Test Rig Set-up

The experimental setup is shown in Figure 51. The test rig, shown in Figure 52, is the one-stage gearbox that was designed to validate the numerical results previously found. The machine structure is mainly composed of two parallel shafts; each one supports a spur gear at its right end. On the left side, the main shaft is driven by a DC motor (Dayton, USA). The secondary shaft is retractable to allow the quick and easy mounting and dismounting of the gears. A magnetic brake (Merobel, France) is installed around that second shaft on its left side to apply a resistive torque. A protective safety box made of the acrylic sheet was specially built to cover the tested bearing during the experiments and to protect the user from flying disconnected objects.

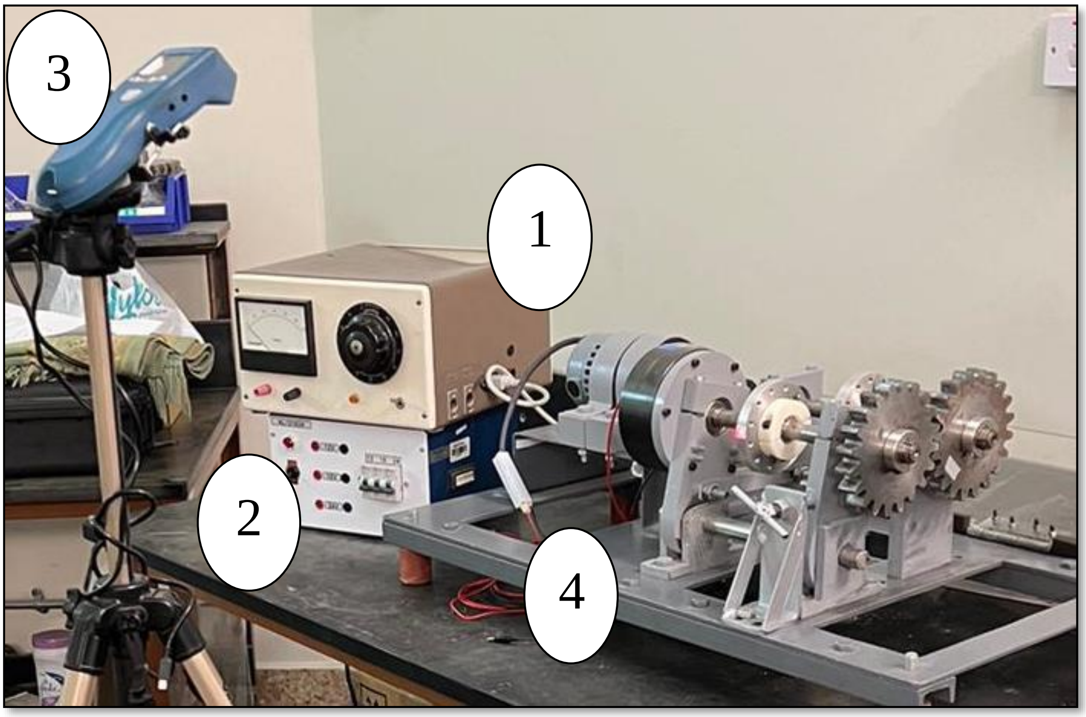

Figure 51: Experimental set-up

The vibration signal is measured by using an ICP accelerometer (from PCB Piezotronics, Model No. 352C33, 100 mV/g) directly mounted on top of the housing holding the bearings that support the shaft rotations. The data acquisition system consists of a National Instrument (NI cDAQ-9174) that allows data acquisition at a sampling rate of 51.2 kHz. A host PC is used for the control of the acquisition and the saving of the experimental data.

Table 3: Description Of Parts In The Experimental Set-Up

Part No.	Name
1	DC Power Supply (Brake)
2	DC Power Supply (Motor)
3	Tachometer
4	Test Rig
4. a	Universal DC motor
4. b	Magnetic Brake
4. c	Balancing Disks
4.d	Spur Gear

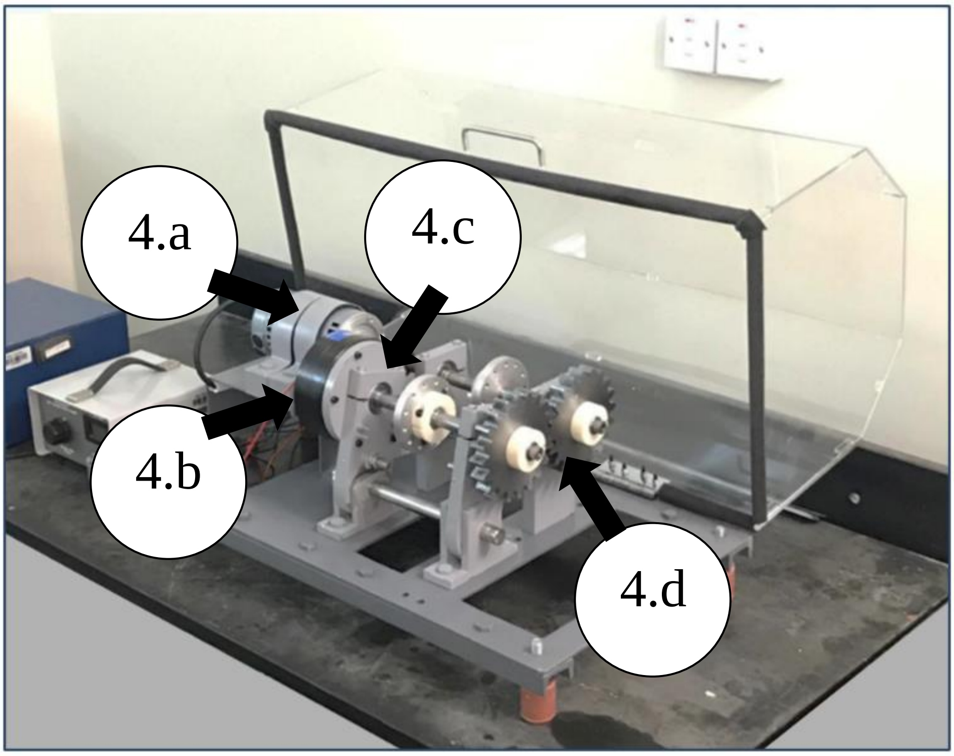

Figure 52: Experimental test-rig

As summarized in Table 4 and detailed in Figure 53, nine gears were considered in the present investigation, where the technique of Electric Discharge Machining (EDM) was used to intentionally seed artificial cracks with CLP% varying from 0% to 50%.

Table 4: Details Of Gear Cracking Cases

Gear Ref.	Case	Cracks Properties			Locations
		Number	CLP (%)	Propagation Angle (°)	
1	Healthy	0	0	0	–
2	Cracked (single)	1	10	0	On one tooth
3	Cracked (single)	1	20	0	On one tooth
4	Cracked (single)	1	30	0	On one tooth
5	Cracked (single)	1	40	0	On one tooth
6	Cracked (single)	1	50	0	On one tooth

Gear Ref.	Case	Cracks Properties			Locations
		Number	CLP (%)	Propagation Angle (°)	
7	Cracked (multiple)	2	20 and 30	0 and 0	On two teeth separated by 180 degrees
8	Cracked (multiple)	2	20 and 30	0 and 35	On two teeth separated by 90 degrees
9	Cracked (multiple)	2	20 and 30	35 and 0	On two consecutive teeth

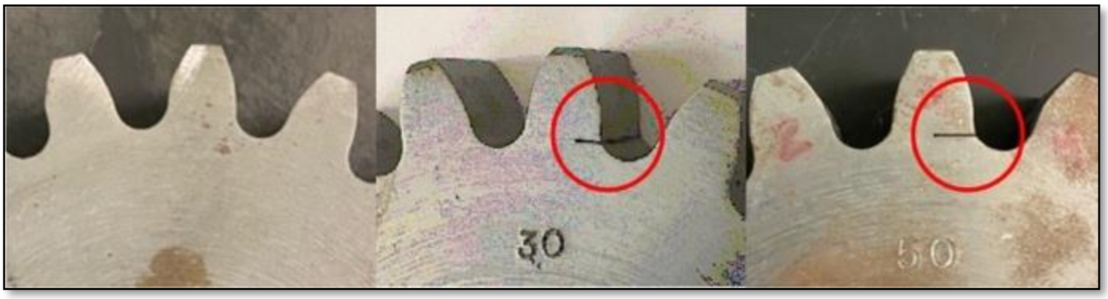

Figure 53: Three gears, one with 50% CLP, one with 30% CLP, and one is clean

4.2. Experimental Set-Up Results

Setting the rotational speed at 750 rpm and the load to a minor value that ensures good contact between teeth without creating too much internal stress in the machine, the vibration was collected for different cases of gearing. These preliminary tests were initiated with a pair of gears without cracks. Later, one healthy gear (without cracks) was kept in position, and the other one was replaced by several gears with cracks ranging from 10% to 50%. Performing a repeatability test is an essential part of estimating uncertainty in measurement. Therefore, at each one of these combinations, the floating gear was dismounted and mounted several times for the only purpose of verifying the repeatability of the measurements. For each case, five mounting-dismounting cycles were conducted. The peak values measured at each case are reported in Figure 54, together with their average values.

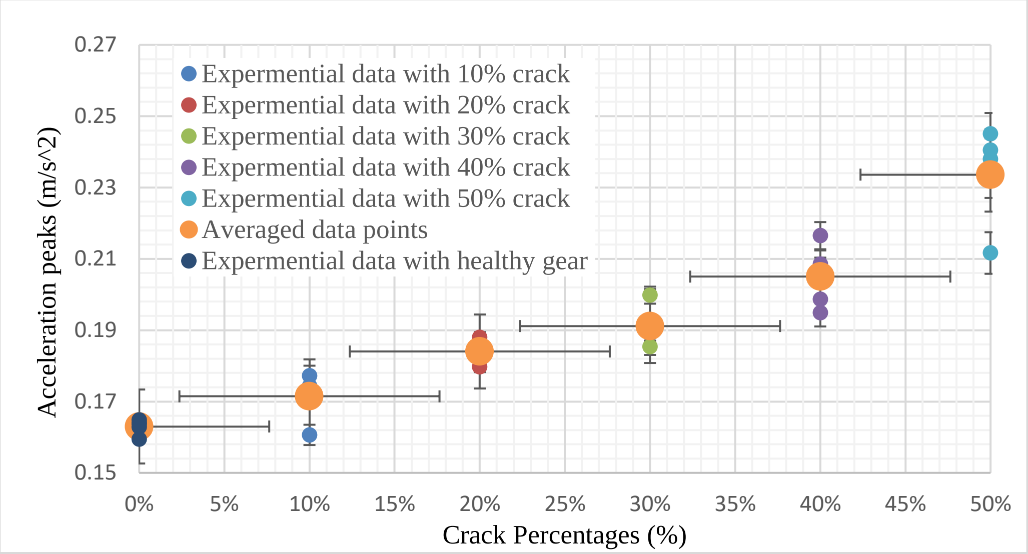

Figure 54: Repeatability tests for different sets of gearing systems

Despite the frequent mounting-dismounting cycles, the readings remained centered inside reasonable small boundaries. Such a result reassures the users about the repeatability of the readings and hence the reliability of the test rig.

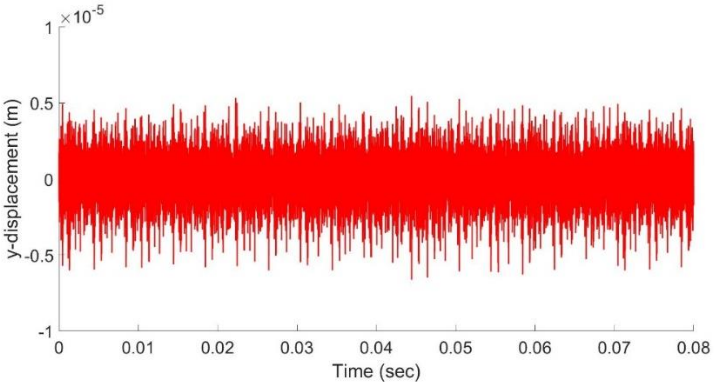

Figure 55: Experimental vibration time response of gear with CLP = 10%

CHAPTER 5: NUMERICAL MODEL VALIDATION AND COMPARISON

In this chapter, several health indicators were applied to both the numerical and experimental responses to verify the numerical model. This was done by comparing the indicators of five distinct situations, each of which was based on a different sort of noise. The data is then analyzed to determine which form of noise most closely resembles the signal generated by the actual machinery.

5,1 Health Indicators and Vibration Analysis

To properly supervise and monitor the state of a machine, investigators are required to choose a certain number of indicators in advance. An indicator is derived from a parameter that may be obtained while the machine is operating. This parameter must accurately represent the status of the machine as well as its performance. The progression of these indications through time is suggestive of the emergence of a defect or the worsening of an existing fault.

5.1.1 Time Domain Analysis

Some say that time domain analysis is the simplest and most straightforward method for assessing the vibration signal. However, there are limitations to the approach, such as in the situation of many flaws or when trying to locate a defect in a very small area of a component. Indicative of the emergence or spread of a flaw, however, is the observable change over time.

Several time-domain statistical metrics have been presented in the literature [72] for use in tracking the impact of growing fault sizes on the vibration response of gears. In most cases, the value of an indicator does not matter much. Its development over time, however, often indicates the presence or spread of a flaw. Maximum or peak value (Max or PEAK), root mean square (RMS), and kurtosis are the most popular statistical scalar characteristics used in mechanical defect diagnosis (KU). Each of these variables is defined in Table 5.

Table 5: Time Domain Indicators For Detecting Gear Vibrations

Indicator	Equation	
Peak/Max	$a_{peak} = sup_{1 \le k \le N} \lvert a_k \rvert$	(53)
Root mean square	$a_{RMS} = \sqrt{\frac{1}{N} \sum_{k=1}^{N} a_k^2}$	(54)
Kurtosis	$KU = \frac{\frac{1}{N} \sum_{K=1}^{N} (a_k - \bar{a})^4}{a_{RMS}^4}$	(55)

5.2 Numerical Model Validation and Comparison

In the first step, the test rig was set up with two undamaged gears, and vibration signals were recorded, evaluated, and saved. Signal processing attempts might make use of the retrieved time domain characteristics from the healthy vibration data. Then, a healthy gear was swapped out for a cracked one of a predetermined value on the test rig. Once again, data was collected and evaluated in the temporal domain. Whether the test gears put on the rig are healthy or broken, the device's contribution will be reflected in all the tests since the vibration signal emitted by the gear must travel through the machine to reach the sensor.

5.2.1 Results Comparisons

For the sake of comparison between numerical and experimental results, several simulations were executed and compared with the same running conditions for each of the previous experimental cases. The peak vibration values obtained from both approaches are displayed in Figure 56.

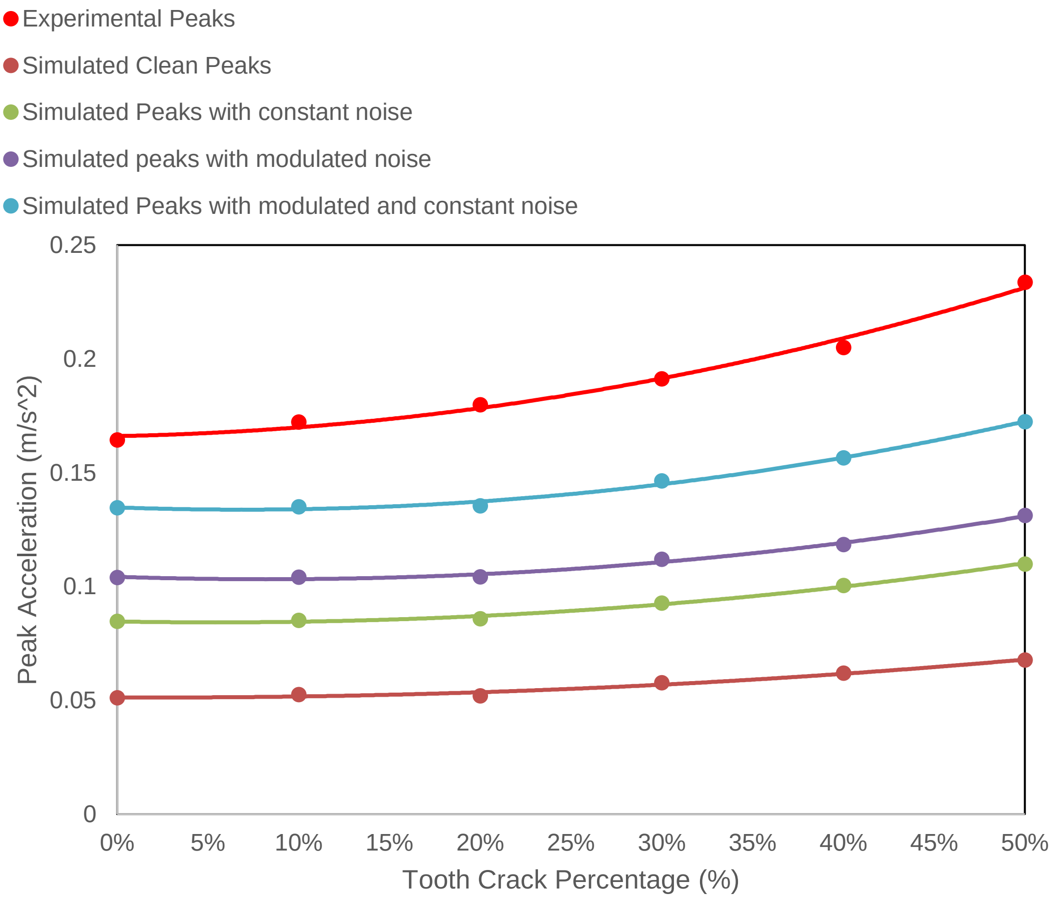

Figure 56: Comparison between raw numerical data and experimental results

From a glance at the plots of acceleration peaks in Figure 56, it is shown that the vibration sensitivity to crack width and the increasing amplitude is the common factor between all sets of results. Moreover, the addition of friction-induced vibration (of noisy type) to the impulsive periodic response in the numerical simulation of gears efficiently contributes to obtaining more truthful results. To get closer to the experimental results, the modulated noise is better than the constant one. However, a combination of both of them is even much effective. A ratio of 60% modulated noise to 40% constant noise was found to be the most appropriate combination that minimizes the difference between experimental and numerical simulations.

Such a difference is created because the numerical model focused mainly on the gears' behavior without considering the neighboring elements. However, an accelerometer placed on the housing will collect all the vibrations generated from all the machine components.

The constants K_m and K_c Introduced in Equations (48-49) should be updated to tune the model and make it quantitatively realistic. Once the two sets of results are made equal for one situation, the first one, when no cracks is considered, a sensitivity analysis is considered. The two curves displayed in Figure 57 are those obtained after normalizing the values with respect to the common first value obtained in the absence of cracks. The maximum deviation between experimental measurement and numerical simulation, for a severe case of 50% crack width, is neighboring 11%.

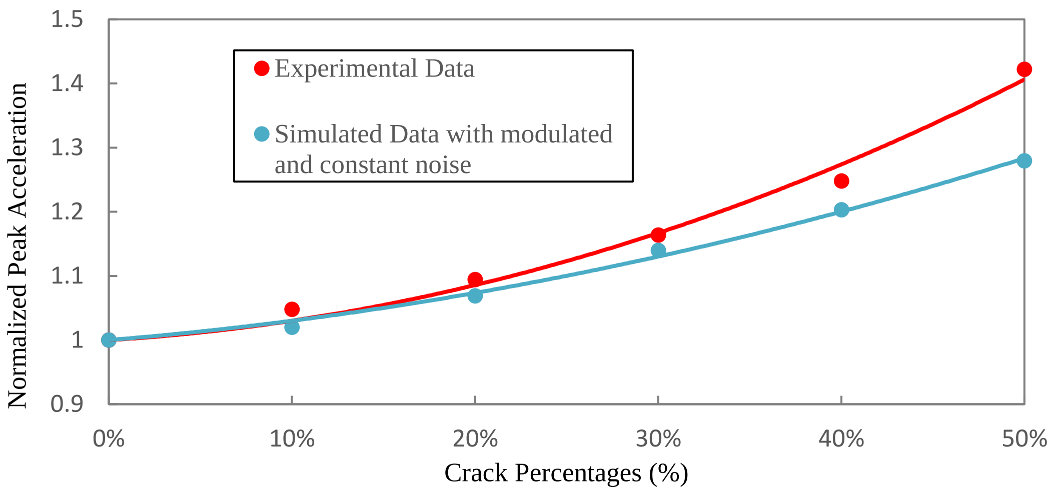

Figure 57: Sensitivity analysis for experimental and numerical results

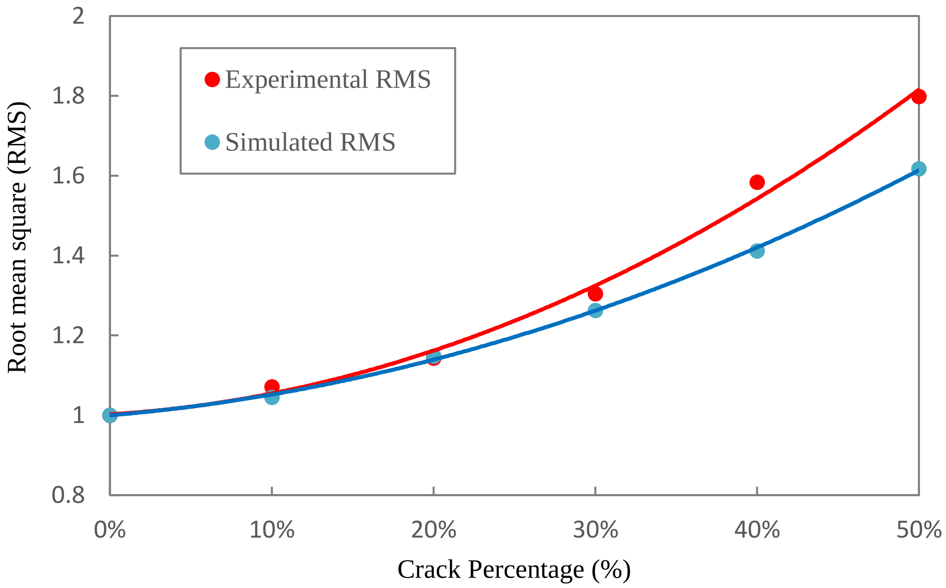

Figure 58: Root mean square values for the experimental and numerical results

The reliability of the model and its ability to produce realistic results is also checked for the RMS, an indicator related to the amount of energy present in the collected signal, and the Kurtosis, an indicator related to the peak sharpness of a frequency distribution. Both indicators were confirmed as sensitive tools for the monitoring of many damage mechanisms, including the cracks in the gears. Moreover, the Kurtosis was found to be particularly reliable and effective since it is unaffected by the operating conditions, such as load and speed.

As can be observed in Figure 58, the RMS of both experimental and numerical results were normalized to have the same starting point to confirm the sensitivity of RMS to the increase in crack width. For a crack width of 50%, there are 87% and 80% increases in the RMS values, according to the numerical and experimental readings, respectively. The maximum relative error between both sets of results is neighboring 11%.

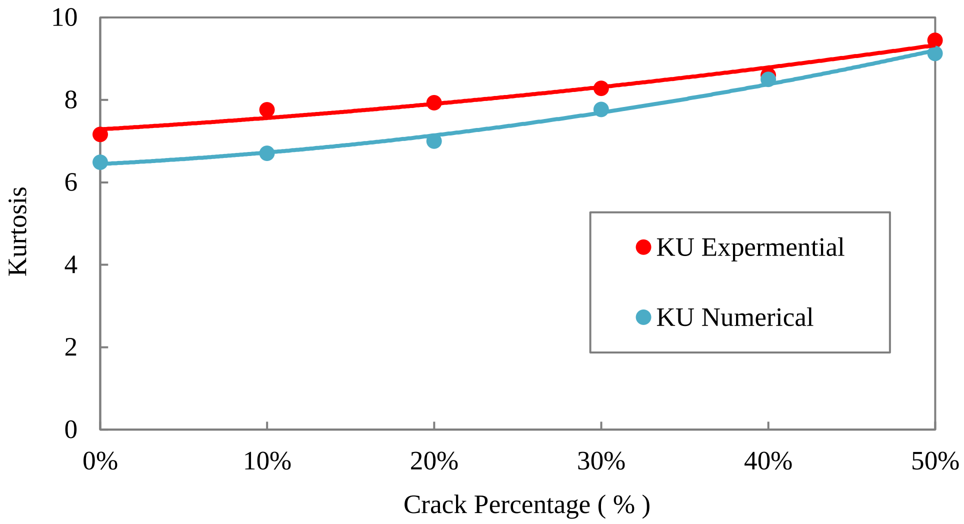

Figure 59: Kurtosis values for the experimental and numerical results

Again, the comparative investigation of the Kurtosis variation in Figure 59 shows very similar and comparable behaviors according to the experimental and numerical approaches. Within the range of investigation, the relative error is neighboring 10%.

5.2.2 Vibration Response

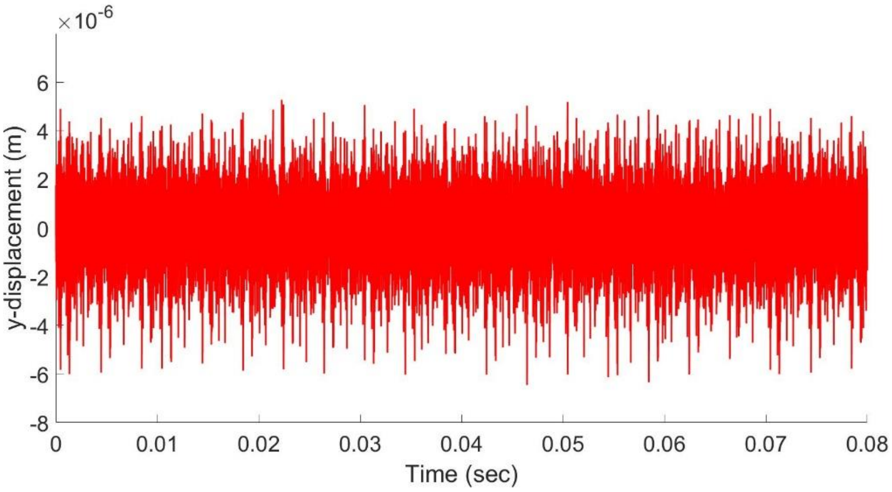

Figure 60: Experimental vibration signal of healthy gear

PEAK = 5.132E-06, RMS = 0.324 E-06 , KU = 3.2377

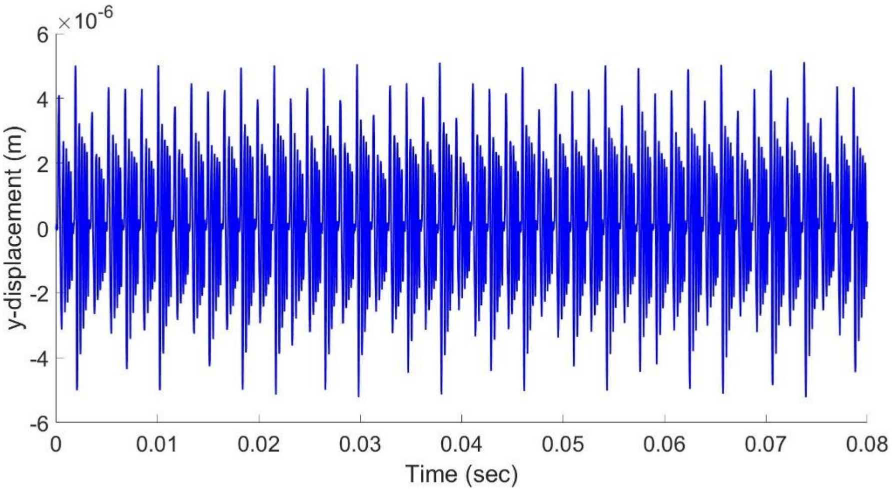

Figure 61: Numerical vibration signal of healthy gear

PEAK = 4.9435E-06 , RMS = 0.304 E-06 , KU = 3.435

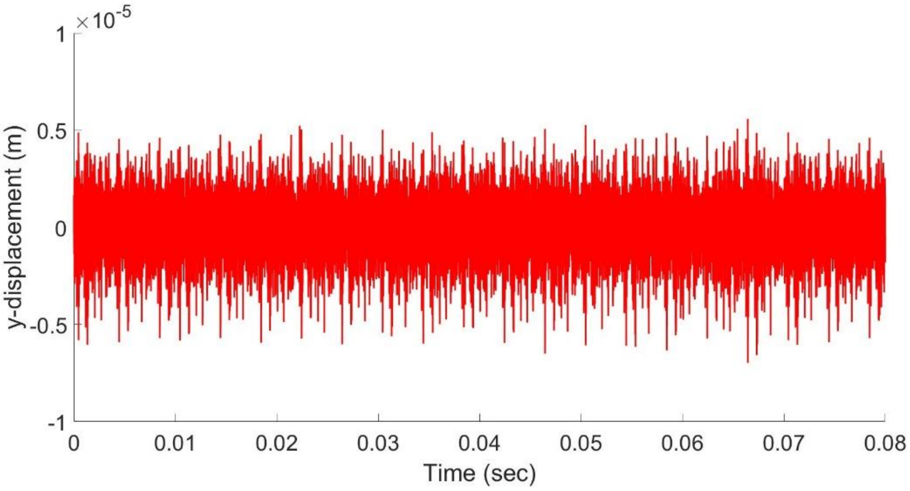

Figure 62: Experimental vibration signal of damaged gear of CLP = 10%

PEAK = 5.545E-06 , RMS = 0.352 E-06 , KU = 5.0345

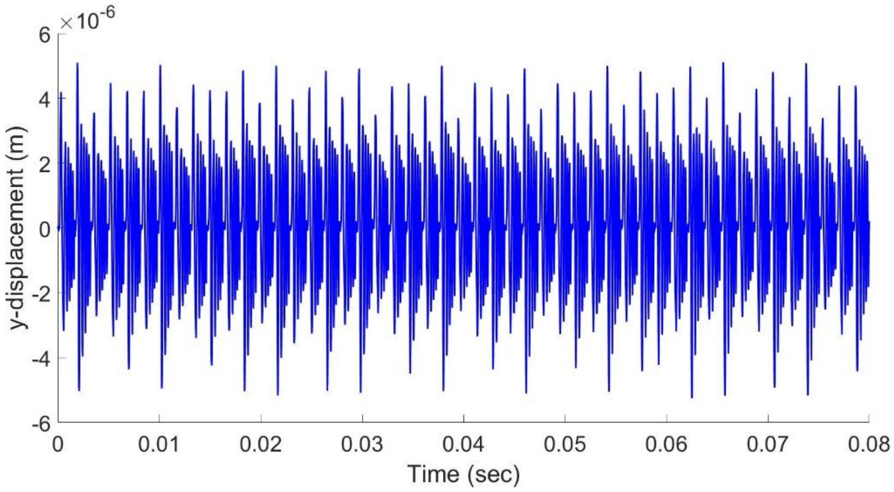

Figure 63: Numerical vibration signal of damaged gear of CLP = 10%

PEAK = 5.434E-06, RMS = 0.334 E-06 , KU = 4.847

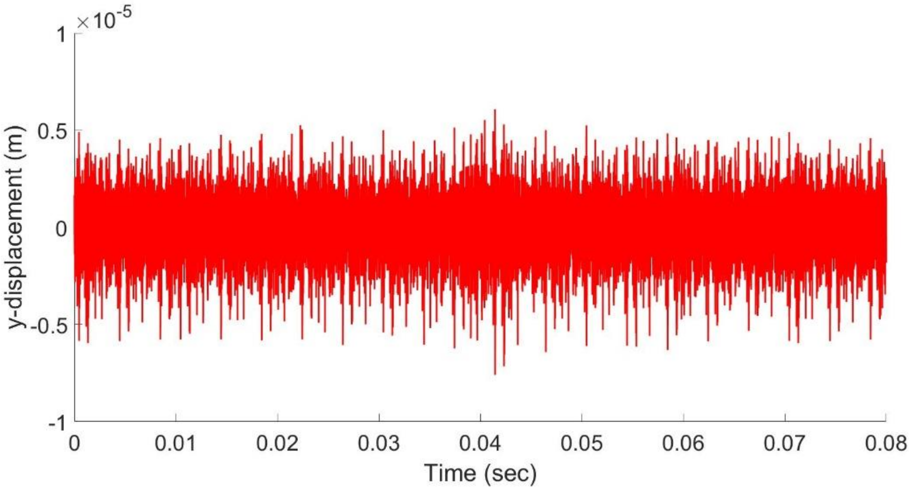

Figure 64: Experimental vibration signal of damaged gear of CLP = 20%

PEAK = 6.034E-06, RMS = 0.379 E-06 , KU = 8.0217

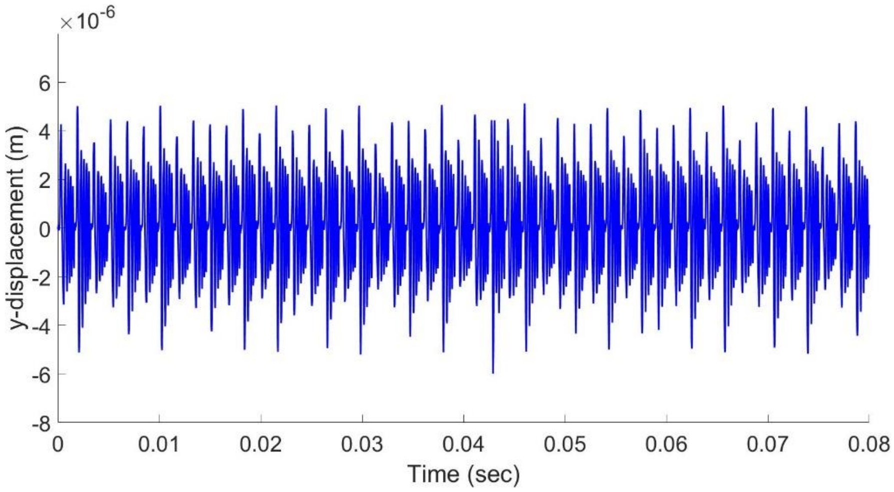

Figure 65: Numerical vibration signal of damaged gear of CLP = 20%

PEAK = 5.864E-06, RMS = 0.368 E-06 , KU = 7.652

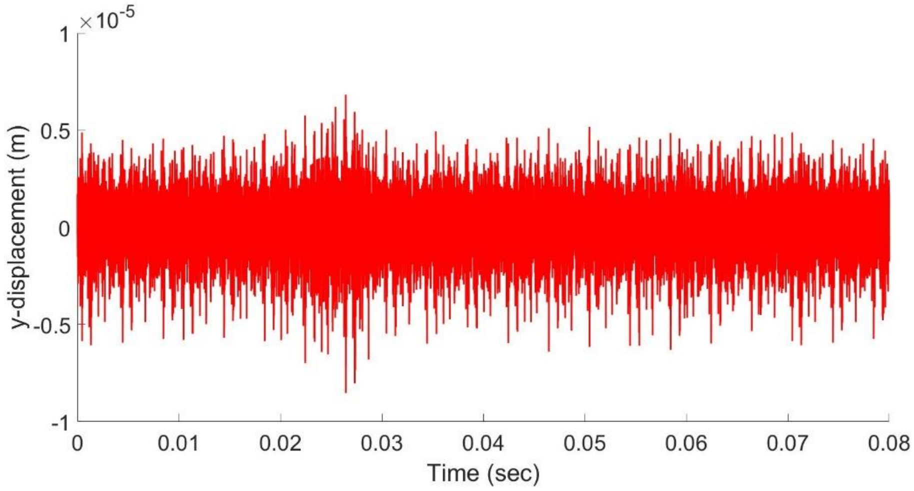

Figure 66: Experimental vibration signal of damaged gear of CLP = 30%

PEAK = 7.234E-06, RMS = 0.414 E-06 , KU = 8.145

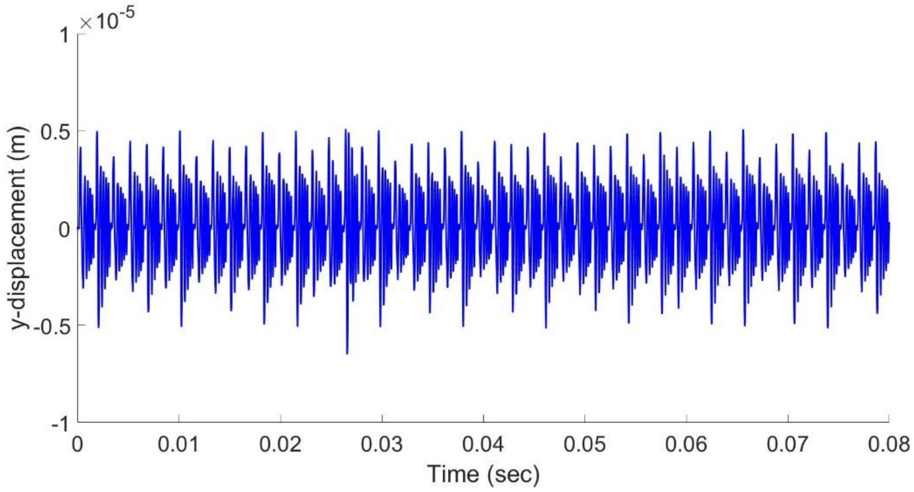

Figure 67: Numerical vibration signal of damaged gear of CLP = 30%

PEAK = 6.943E-06, RMS = 0.384 E-06 , KU = 7.854

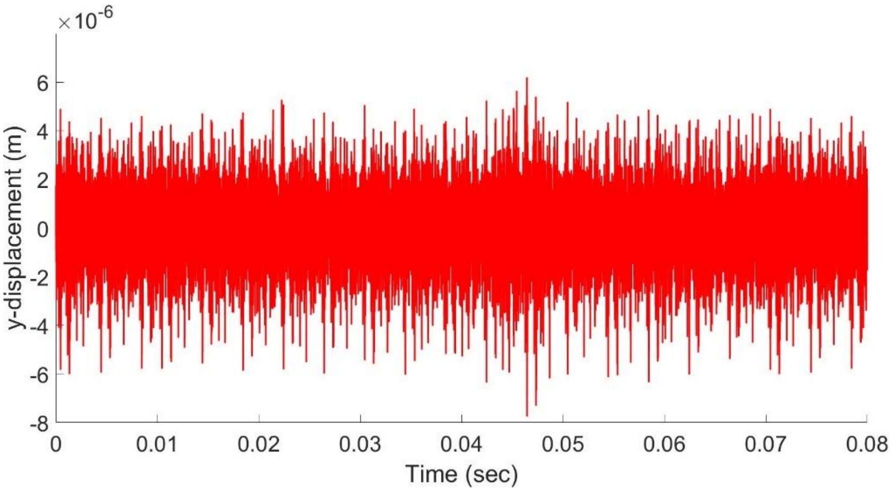

Figure 68: Experimental vibration signal of damaged gear of CLP = 40%

PEAK = 7.653E-06, RMS = 0.444 E-06 , KU = 8.377

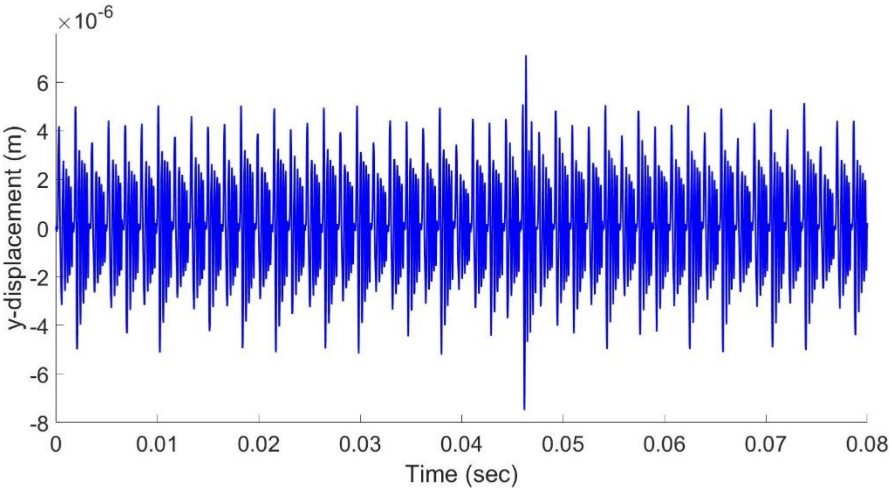

Figure 69: Numerical vibration signal of damaged gear of CLP = 40%

PEAK = 7.543E-06, RMS = 0.412 E-06 , KU = 8.5374

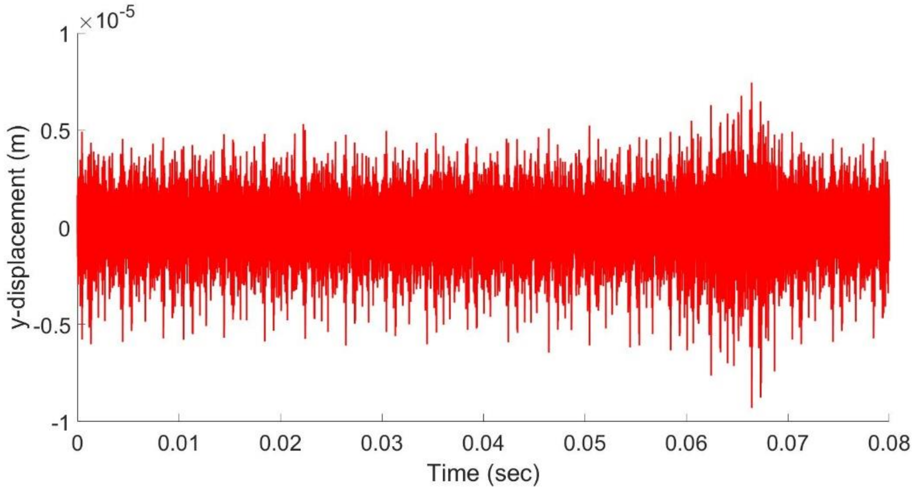

Figure 70: Experimental vibration signal of damaged gear of CLP = 50%

PEAK = 9.7123E-06, RMS = 0.624 E-06 , KU = 9.8577

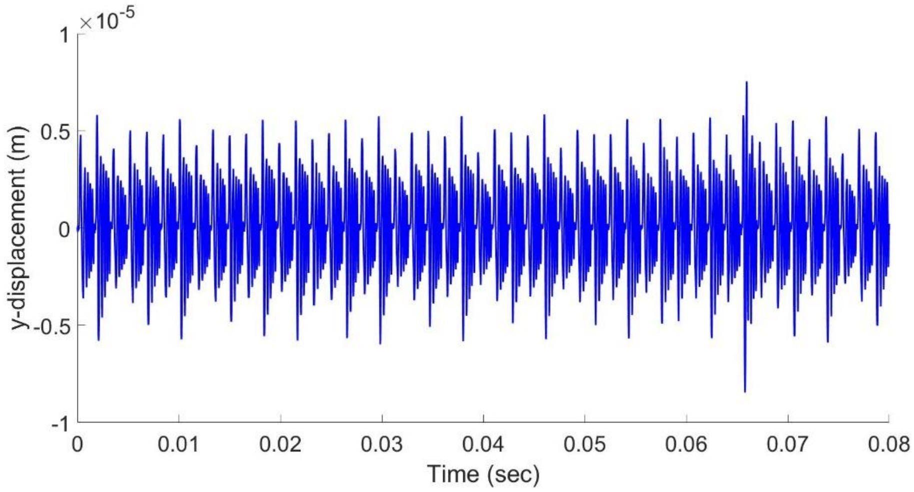

Figure 71: Numerical vibration signal of damaged gear of CLP = 50%

PEAK = 8.932E-06, RMS = 0.585 E-06 , KU = 9.5984

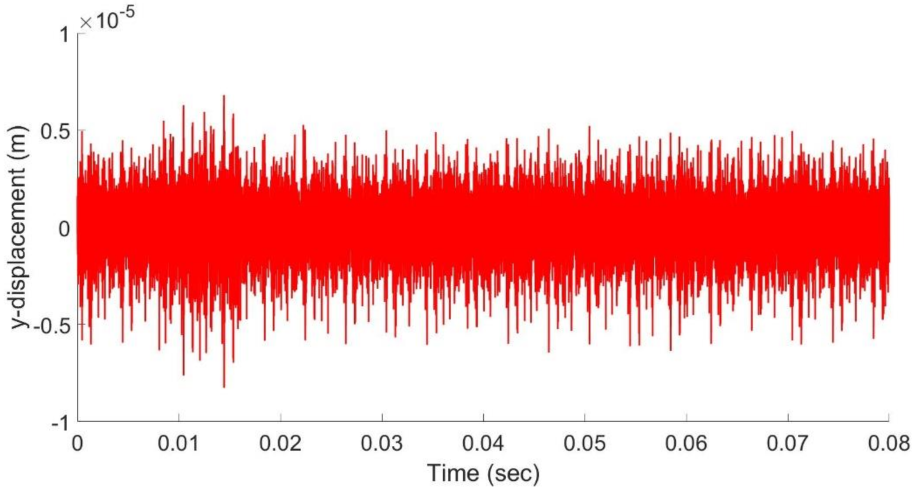

Figure 72: Experimental vibration signal of two consecutive damaged teeth of CLP = 20% and CLP = 30%

PEAK = 7.294E-06, RMS = 0.9324 E-06 , KU = 3.8472

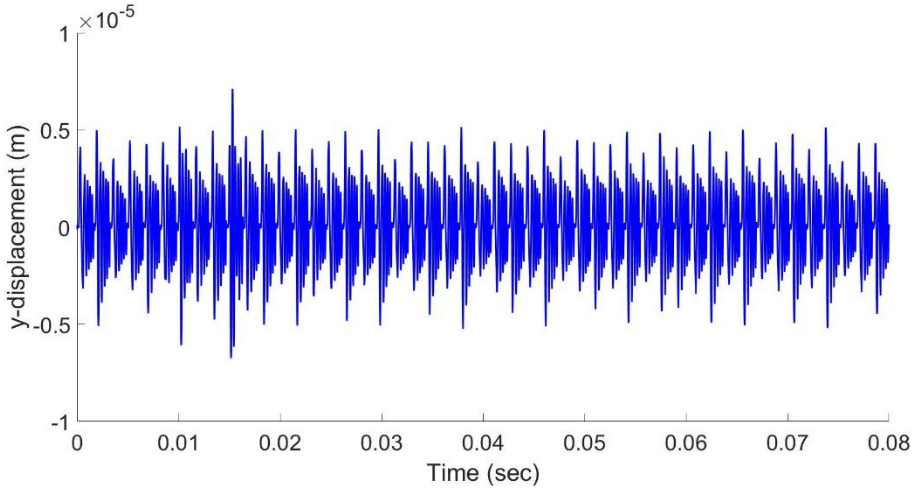

Figure 73: Numerical vibration signal of two consecutive damaged teeth of CLP = 20% and CLP = 30%,

PEAK = 7.024E-06, RMS = 0.8854 E-06 , KU = 3.6377

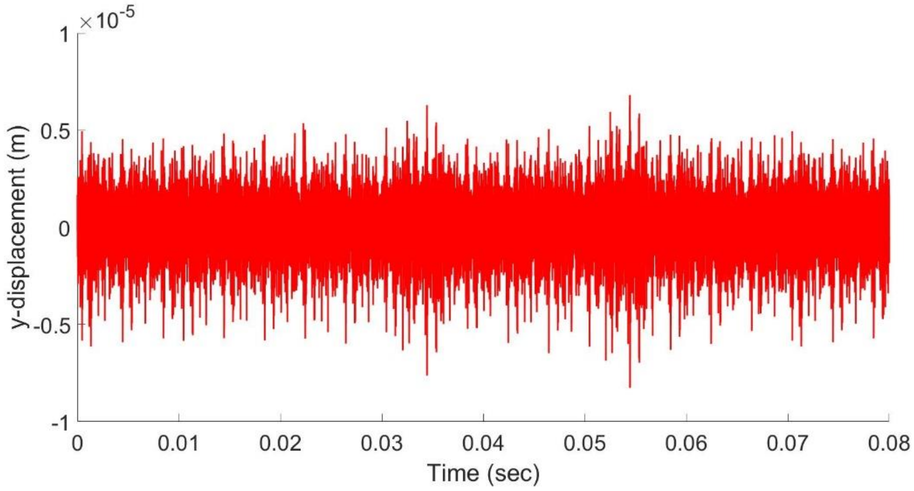

Figure 74: Experimental vibration signal of two 90 degrees apart damaged teeth of CLP = 20% and CLP = 30%,

PEAK = 7.3122-E06, RMS = 1.1324 E-06 , KU = 4.157

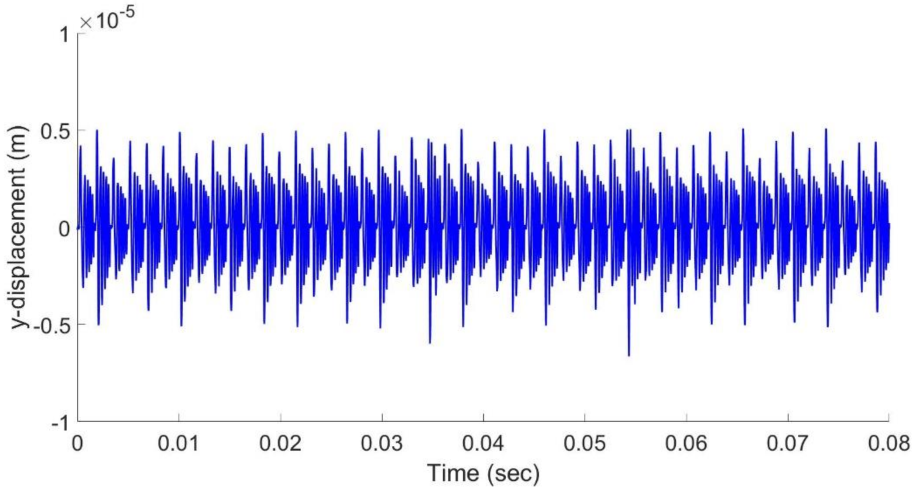

Figure 75: Numerical vibration signal of two 90 degrees apart damaged teeth of CLP = 20% and CLP = 30%

PEAK =7.1743E-06, RMS = 1.0324 E-06 , KU = 4.2117

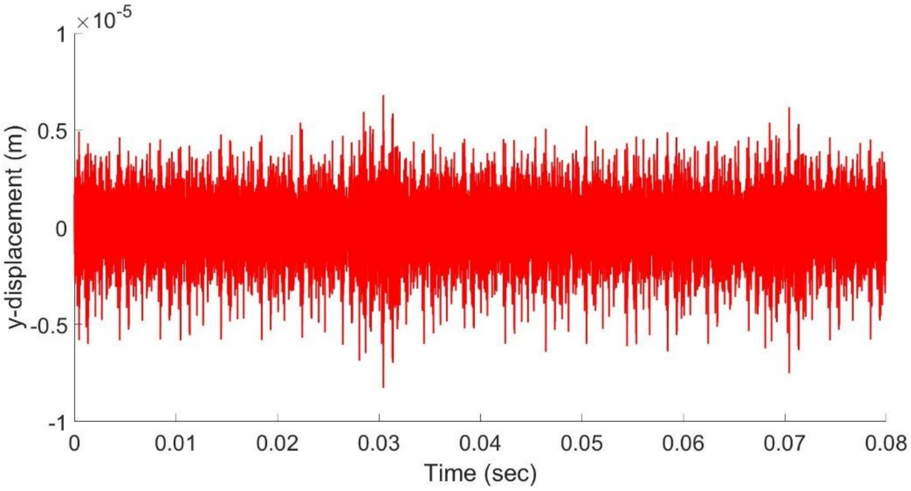

Figure 76: Experimental vibration signal of two 180 degrees apart damaged teeth of CLP = 20% and CLP = 30%,

PEAK = 7.534E-06, RMS = 1.014 E-06 , KU = 3.1287

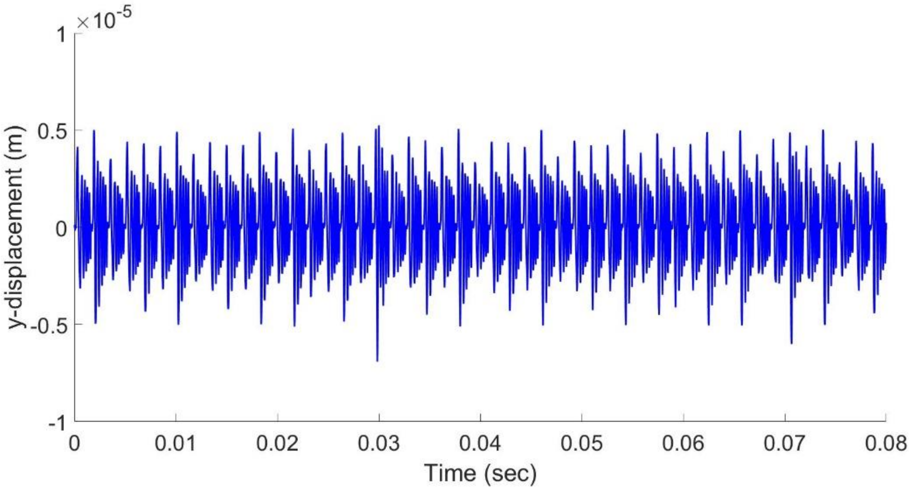

Figure 77: Numerical vibration signal of two 180 degrees apart damaged teeth of CLP = 20% and CLP = 30%,

PEAK = 7.385E-06 , RMS = 0.9644 E-06 , KU = 3.0847

CHAPTER 6: IMPLEMENTATION OF MACHINE LEARNING TECHNIQUES IN GEAR FAULT DETECTION

In this chapter, two different methods based on the type of input data are approached. The first is based on time series sequential vibration data, where it combines the conventional 1-D CNN with an LSTM network in multilabel classification. When it comes to processing Vibration signals, the CNN is employed, while the LSTM network is used to handle Residual data. In such a case, the CNN's outputs will be combined with those of the LSTM network. The second approach employs Image processing in 2D CNN Multi-label Image Classification by using time domain residual signal images and spectrograms of principal components

6.1 Combined Model of 1-Dimensional CNN and LSTM

As will be shown in this chapter, and among the approaches covered in the literature, CNNs are commonly utilized as active learning models with applications in defect detection [114]. Several academics have lately tried to identify gear failures using deep 2D CNNs. However, it should be emphasized that 2D CNNs, especially those with deep architectures or large-scale datasets, have a significant computational cost [115].

The aforementioned research has several limitations and downsides. They were all based on a single sort of signal. Some of them have considerable computational complexity, which is a barrier for real-time applications, while others utilize datasets that are often restricted in size, resulting in inaccurate approaches. Finally, the majority of them are only fault detectors and cannot determine the severity of the defect and mostly use raw vibration signals, whether in the time or frequency domain, and very few of them took into consideration using images as an input.

The suggested system's workflow entails the creation of datasets in the form of images from which various kinds of plots are derived to analyze their changing behavior in defect gear identification and diagnosis. This allows the planned facilities to operate in a safe and cost-effective manner, as well as maintain structural health.

Figure 78 depicts the overarching steps involved in the proposed technique for spur gears with cracked teeth problem diagnostics.

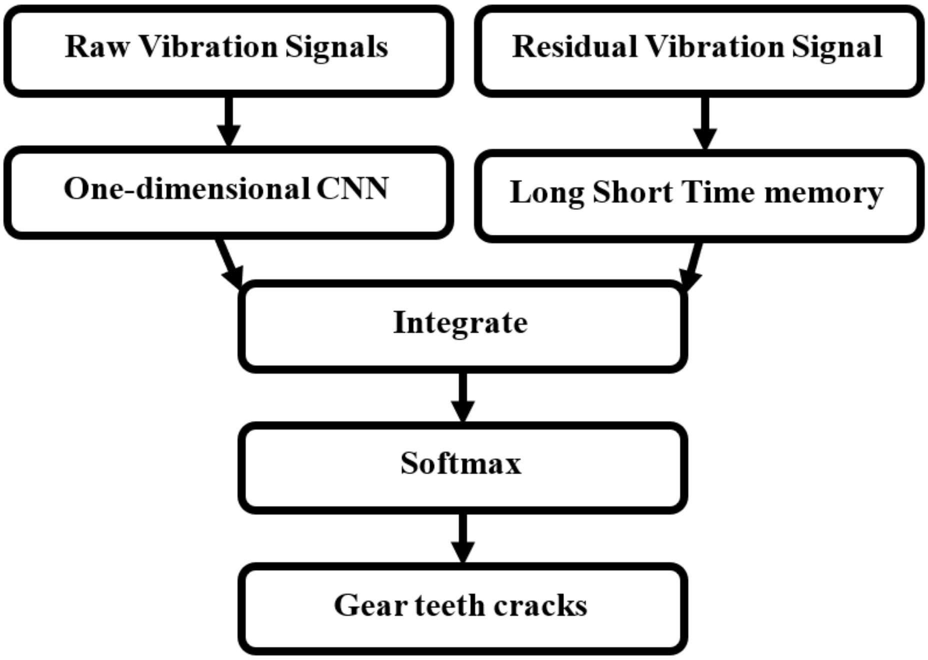

Figure 78: The general procedure of the presented method one, concatenated CNN and LSTM

6.1.1 Multi-Label Classification Using One-Dimensional Convolutional Neural Network

An input layer, an output layer, a convolution layer, and a pooling layer are typical components of a CNN [116]. The convolution layer uses the convolution kernel to extract local features from the input feature map. The pooling layer will do farther-down sampling. CNN's major characteristics are local perception, weight sharing, and pooling. The convolutional layer and the pooling layer occur alternately in CNN. In Figure 79, the one-dimensional CNN principle is depicted.

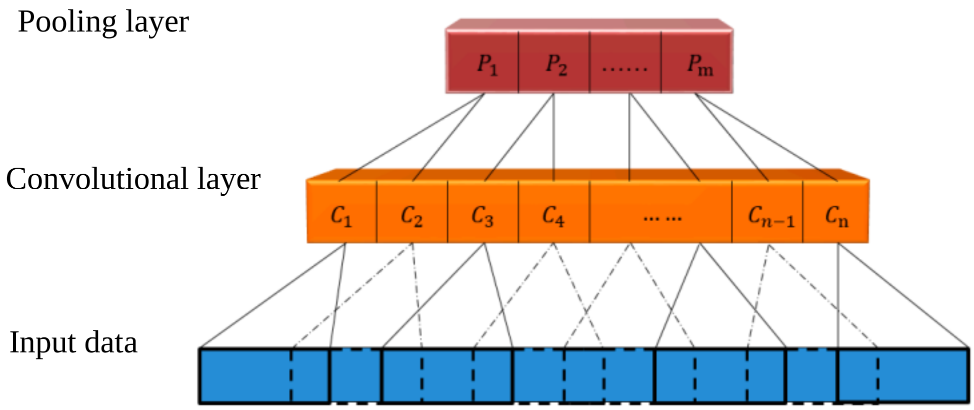

Figure 79: One-dimensional CNN schematic

The following is the mathematical formula for the one-dimensional convolutional layer, given that the initial layer is a convolutional layer:

$$x_j^l = f\left(\sum_{i=1}^{M} x_i^{l-1} * k_{ij}^l + b_j^l\right) \tag{56}$$

Where:

x_j^l: indicates the jth feature map that is included inside the lth layer.

f: denotes the activation function.

M: denotes the number of input feature maps.

x_j^{l-1}: denotes the ith feature map of the $l-1$ layer.

$*$: denotes convolution operation.

k_{ij}^{l}: denotes a trainable convolution kernel.

b_j^l: denotes the jth bias of the lth layer.

The sigmoid activation function is utilized because it is appropriate to consider both the rate of convergence and the overfitting issue and since it is a multi-label problem. This function is defined as follows:

$$\sigma\,(x) = \frac{1}{1 + e^{-x}} \tag{57}$$

Where e is Euler’s number, after the pooling layer, in Equation (57) has been linked to the convolution layer, the feature map must next undergo down-sampling in accordance with a particular pooling method in order to get a feature map with a lower resolution. The maximum pooling method is the one that is used the vast majority of the time. The number of output nodes may be cut down by maximum pooling, which also improves the network's resistance to changes in the characteristics of inputs.

$$x_j^{l+1} = f[down\left(x_j^l\right) + b_j^{l+1}\,] \tag{58}$$

6.1.2 Multi-Label Classification Using Long Short-Term Memory Recurrent Neural Network

The theory behind LSTMs is that by using a small number of gates at each time step, long-range relationships can be captured more precisely. For the classification method, the LSTM sequential model was used. An input gate i^t, a forget gate f^t, an output gate o^t, and a memory cell c^t, are used to combine with the current data X^tAt the same time, step t to update the hidden state h^{t-1}.

The aforementioned update formulae are shown below:

$$i^t = \sigma\left(W^i x^t + V^i h^{t-1} + b^i\right) \tag{59}$$

$$f^t = \sigma(W^f x^t + V^f h^{t-1} + b^f) \tag{60}$$

$$o^t = \sigma(W^o x^t + V^o h^{t-1} + b^o) \tag{61}$$

$$c^t = f^t \odot c^{t-1} + i^t \odot tanh(W^c x^t + V^c h^{t-1} + b^c) \tag{62}$$

$$h^t = o^t \odot \tanh(c^t) \tag{63}$$

Where:

Model parameters, including all $W \in \mathbb{R}^{dxk}$, $V \in \mathbb{R}^{dxk}$ and $b \in \mathbb{R}^{dxk}$ Are shared by all time steps and learned during model training.

σ : is the sigmoid activation function defined in Equation (57)

$\odot$: denotes the element-wise product,

k: is a hyper-parameter that represents the dimensionality of hidden vectors.

Firstly, the basic LSTMs are constructed to process the sequential data in time order. And the output at the terminal time step is used to predict the output by the sigmoid function, as shown in Equation (57).

Binary cross-entropy in Keras is used as a model loss when comparing the projected parameter y to the actual parameter value y during model training.

$$loss = -\frac{1}{n}\sum_{i=1}^{n} y_i \cdot \log(\hat{y_i}) + (1 - y_i) \cdot (1 - \hat{y_i}) \qquad (64)$$

Where,

n: output size, which is the number of scalar values in the model output

$\hat{y_i}$: is the ith scalar value in the model output

y_i: is the corresponding target value.

6.1.3 Dataset Creation

The experimental findings that were received from the test rig are to be preserved for testing purposes, and the validated simulated dynamic model that was detailed in the section is utilized for training the models. Raw vibration data and residual vibration data are recovered from the numerical mode and employed in CNN and RNN, respectively. Table 6 shows an example raw vibration signal of the gears. Without any preprocessing, the data is provided to the models in a sequential format (time series).

Table 6: Input Signals To The 1D CNN And LSTM

	CNN - Raw vibration signal	LSTM - Residual vibration signal
1	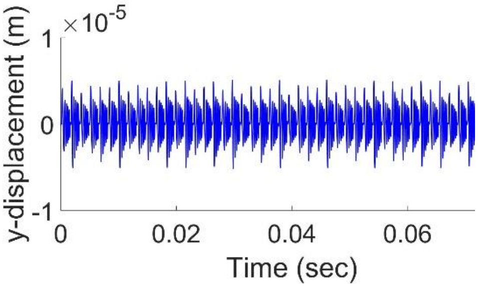	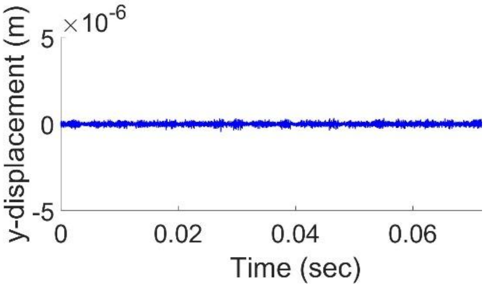

	CNN - Raw vibration signal	LSTM - Residual vibration signal
2	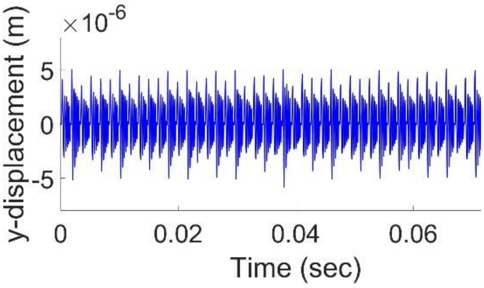	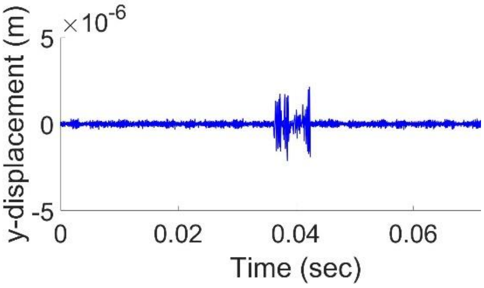
3	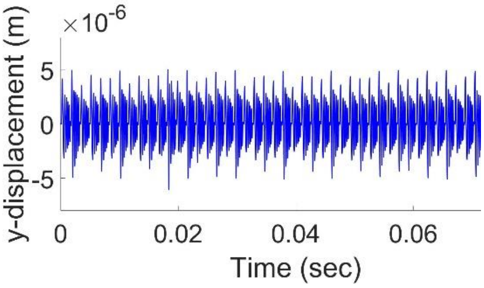	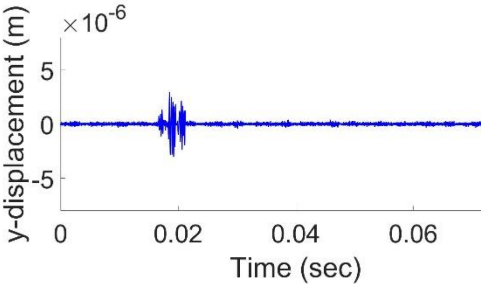

Table 6 shows 3 different residual and raw vibration signals cases of r of 1) clean 2) CLP = 20% Crack No.10, 3) CLP = 30% Crack No.=5. All signals were captured at 750 RPM at a sampling rate of 140,725 Hz for precisely 0.08s, which is one cycle of the gear set.

Based on previous experience, the CNN was built with four convolutional layers coupled together. It was decided to put 64, 128, 256, and 256 channels in each of the layers, respectively. Seven was chosen as the kernel size for each convolutional layer, while one was chosen as the stride. In order to keep the same data size, the padding required the use of the type "same padding." The size of the pool was determined to be 2 for each of the pooling levels. When it came to pooling, the strides were put to "none," and the padding was put to "valid." The raw signals that were utilized in the CNN each comprised 3072 different features.

For training, the LSTM network used six stacked LSTMs. Each LSTM layer's cell size was set to 512, 512, 256, 256, 128, and 128, correspondingly. The LSTM network uses residual vibrational signals with 916 characteristics per sample. The batch size has been set to 512. The loss function was configured to be binary cross-entropy. The optimizer was the Adam function. Except for the last layer, the ReLU function was employed as the layer activation function. A sigmoid function was employed in the final layer to categorize gear-broken teeth.

6.1.3.1 Testing Data

The experimental residual data was obtained using the following technique: a normal signal is recorded, then the smallest impulsive tooth signal is recorded and repeated over one period 20 times (the number of gear teeth), and the calculated artificial signal is then subtracted from the original vibration signal to obtain an approximation of the residual using signal subtraction.

Table 7: Experimental residual calculation method

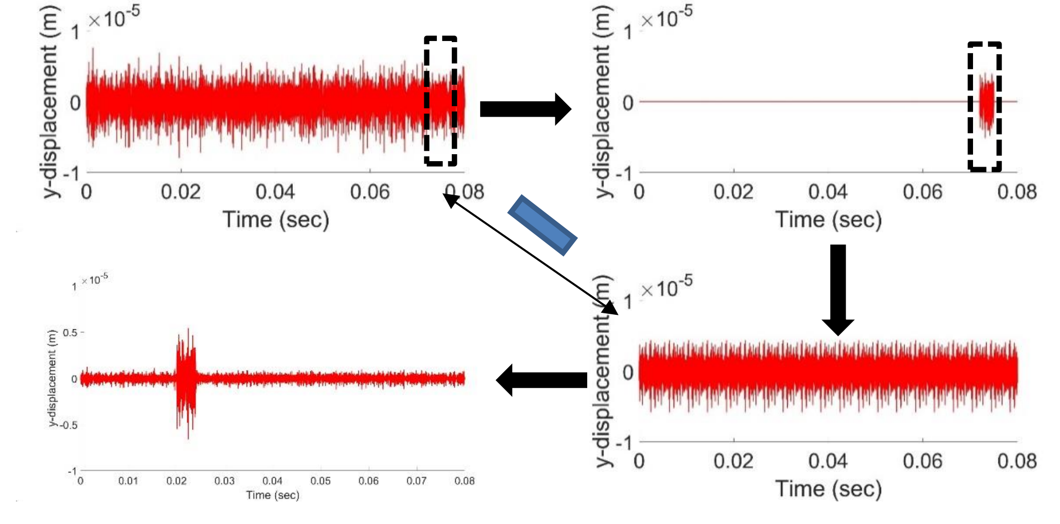

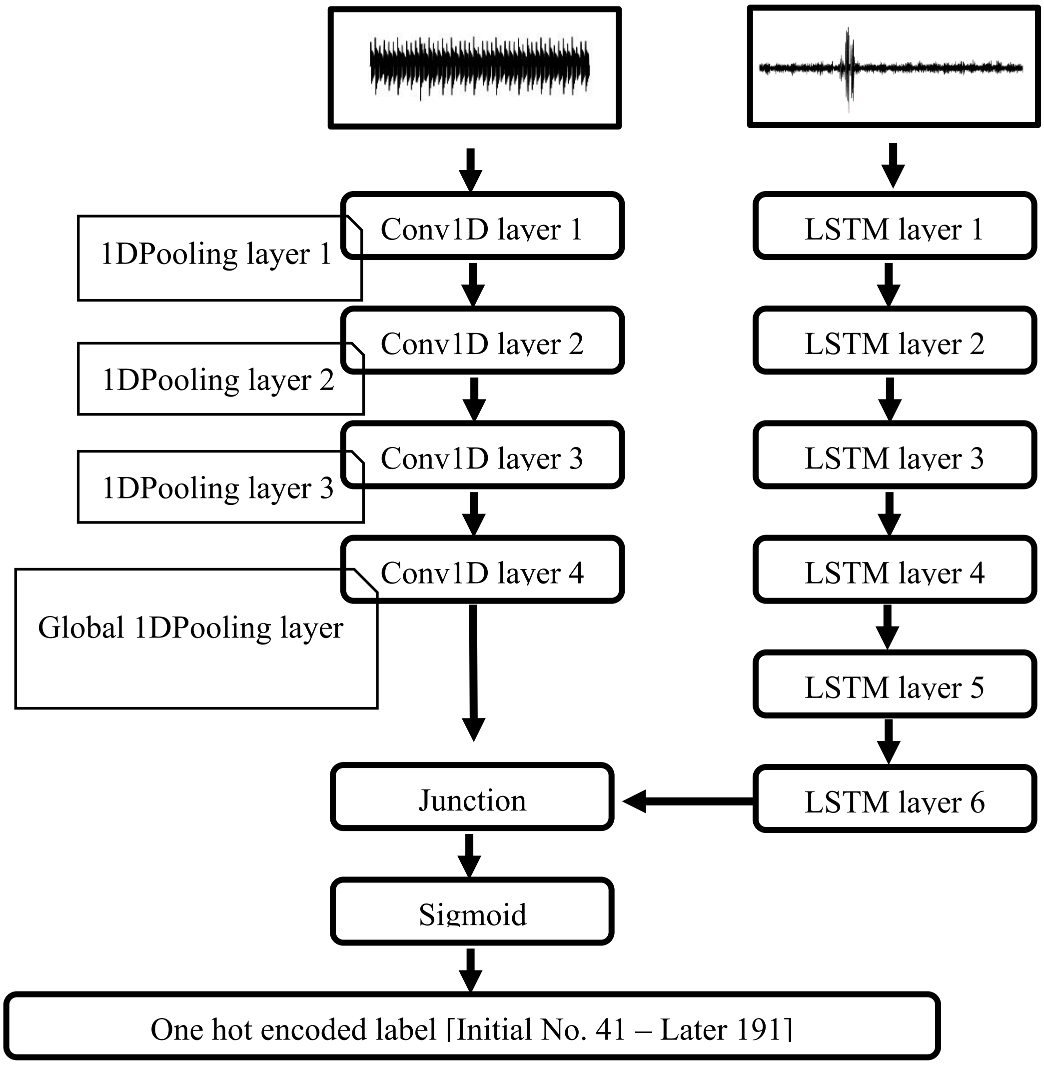

Figure 80: Adopted machine learning approach 1 scheme

6.1.4 Results and Discussion

The model was trained with only 41 unique cases, as the control over the crack location in the experimental set-up is difficult, and that is basically five different locations for each crack percentage which resulted in a total of 40 cases, and the healthy case is singular. Furthermore, for each case, 50 samples were recorded, which resulted in a 2050 sample. 70% of the total number of samples are utilized for training, with the remaining 30% used in conjunction with 45 experimental samples for the 41 different crack scenarios, as only 1 sample for each scenario was recorded to validate and test the model. After the validation, the model was retrained with 190 unique cases for the damaged gear and 1 case for the healthy; each case was recorded 300 times, yielding a total of 57,300 samples. 70% of the total number of samples are utilized for training, with the remaining 30% used in conjunction with 900 unknown experimental samples for the nine unique cases. Additionally, initially, 41 dense layers were used and then 191 based on the number of labels, and the epoch in both methods was set to 512.

The metrics that are used to evaluate the results are accuracy, precision, and recall. The overall accuracy, precision, and recall are calculated as in:

$$Accuracy = \frac{\sum_i^k TP_{class_i} + \sum_i^k TN_{class_i}}{\sum_i^k S_{class_i}} \tag{65}$$

$$Precision = \frac{\sum_i^k TP_{class_i}}{\sum_i^k TP_{class_i} + \sum_i^k FP_{class_i}} \tag{66}$$

$$Recall = \frac{\sum_i^k TP_{class_i}}{\sum_i^k TP_{class_i} + \sum_i^k FN_{class_i}} \tag{67}$$

Where:

TP: True positives

FP: False positives

TN: True negatives

FN: False negatives

S: sum of $TP, FP, TN\ and FN$

Results are shown in Table 8

Table 8: Results Of The Multilabel Regression For Different Models Run #1, 2050 Samples

Method	Validation Accuracy	Testing Accuracy	Average Precision	Average Recall
1D CNN +LSTM	98.554	90.664	90.14	90.2
1D CNN	71.133	65.453	67.83	53.32
LSTM	67.45	59.653	60.48	61.08
LSTM (Parameters)	84.521	83.453	79.5	80.23
CNN (Parameters)	58.75	61.5833	50.822	59.5

The outcomes of the validation are shown in Table 8, and it can be seen that when the CNN with residual signals was used to detect gear teeth fracture faults, the method suffered from a significant underfitting phenomenon. As a direct result of this, the testing accuracy might drop to as low as 61.5833%. Both precision and recall may be seen as indicators of the level of quality and level of quantity, respectively. When an algorithm has higher precision, it indicates that it returns more relevant results than it does irrelevant ones. When an algorithm has a high recall, it means that it returns most of the relevant results (whether or not irrelevant ones are also produced), and in this case, only the first model in Table 8 showed good quality.

On the other hand, the CNN with vibration signals and LSTMs with residual signals generated significant testing and verification results, but they also got correct broken tooth detection rates of 90.664% for testing. This was accomplished by utilizing both sets of signals with the CNN and by only using small samples. The findings imply that the technique offered in this research gives more accurate diagnostic results when compared to other ways. Furthermore, the two models were trained using preprocessed data with three parameters, the Peak, Root Mean Square values, and Kurtosis, and the results showed poor accuracies. The reason behind this could be the small sample size and the parameters not being sensitive to all cases, such as multiple cracks, as the peak and kurtosis parameters are not very sensitive to numerous cracks with different percentages, which was the case in this study.

Table 9: Results Of The Multilabel Regression For Different Models Run #2, 57300 Samples

Method	Validation Accuracy	Testing Accuracy	Average Precision	Average Recall
1D CNN + LSTM	97.434	93.084	91.64	94.43
1D CNN	84.221	82.233	80.76	83.92
LSTM	97.05	91.098	90.08	91.56
LSTM (Parameters)	99.34	90.653	97.034	99.2
CNN (Parameters)	98.23	89.923	96.012	98.04

After retraining the model with a much larger sample size, the results increased substantially, particularly the testing accuracy, since, in the first trial, the cases for the testing data were known but not in the second training session, indicating that the model was validated. The large discrepancy in testing accuracy was caused by the original use of a relatively tiny testing sample. However, the accuracies for models trained using parameters as training data are lower than those for raw and residual data, as previously mentioned. Regarding recall and precision, all models in the second trial showed good results except for the standalone CNN.

6.2 Time-Frequency Analysis Using Spectrogram

A sequential model was used in this 2D CNN, and four convolutional layers were included, with two dense layers and one output layer, because dealing with images requires three or more convolutional layers for best results. The ReLU activation function is used in all convolutional and dense layers except the last output layer, which has the sigmoid function. In addition, each convolutional layer has a pooling layer of the same size as the previous one-dimensional CNN. The kernel size, however, was set to 5. Furthermore, since the pictures are 2-D and must be in 1-D before entering the dense layers, the data is flattened before entering the dense layers, with 32, 64, 128, and 128 channels in each layer, with a dropout of 0.2, while the dropout in the dense layers was set to 0.5. Furthermore, the output layer comprises 41 dense layers, which will be increased to 191 later to verify the model first since regulating the fracture position in the test rig is challenging. The metrics and loss functions are binary cross-entropy and accuracy, respectively. Finally, the epoch is set at 128. The model is shown in Figure 81.

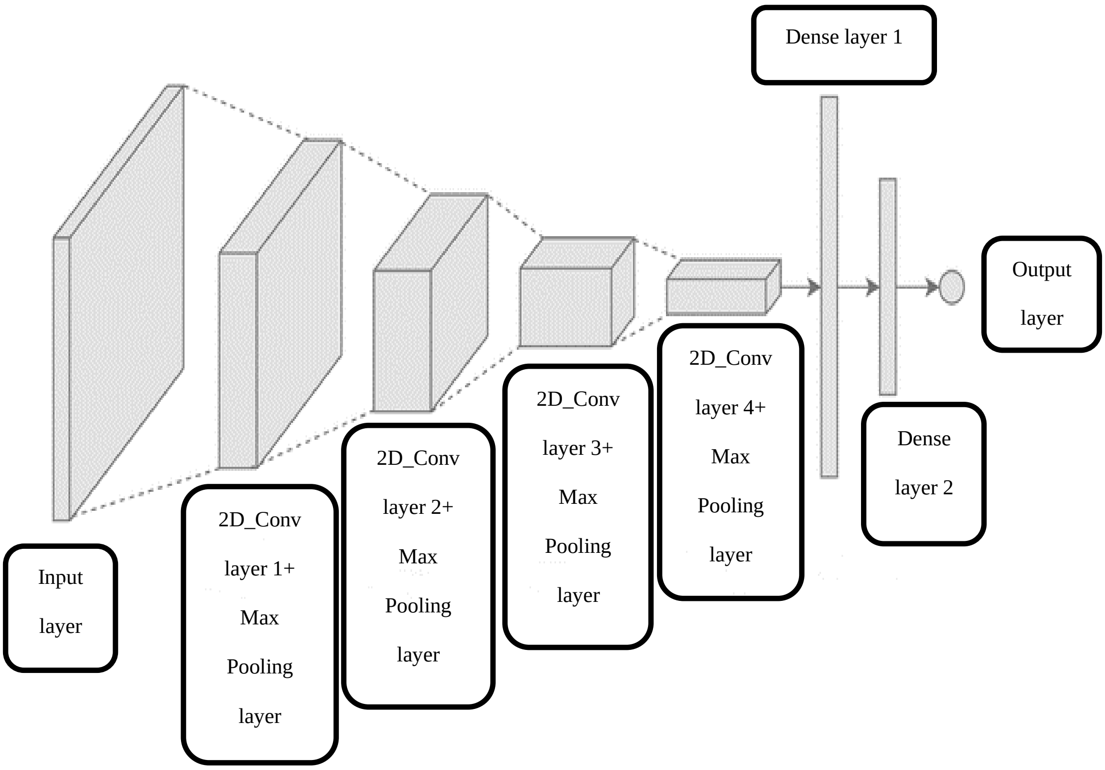

Figure 81: Two-dimensional CNN schematic

6.2.1 Time Domain Analysis Approach

The training, validating, and testing sets are obtained from the developed numerical model and the experimental setup described in chapters 4 & 5. However, the data in this approach will not be used as a time series. Instead, it will be inputted as an image. Firstly, using the time domain signal as an image has not been done previously, and to be able to maximize the training of the model, only the residual signal will be taken into consideration to help in easing the training process. Additionally, the signal will be plotted without an axis and only in colors black and white to minimize the computing time and processing power. Samples of the image input are shown in Figure 82.

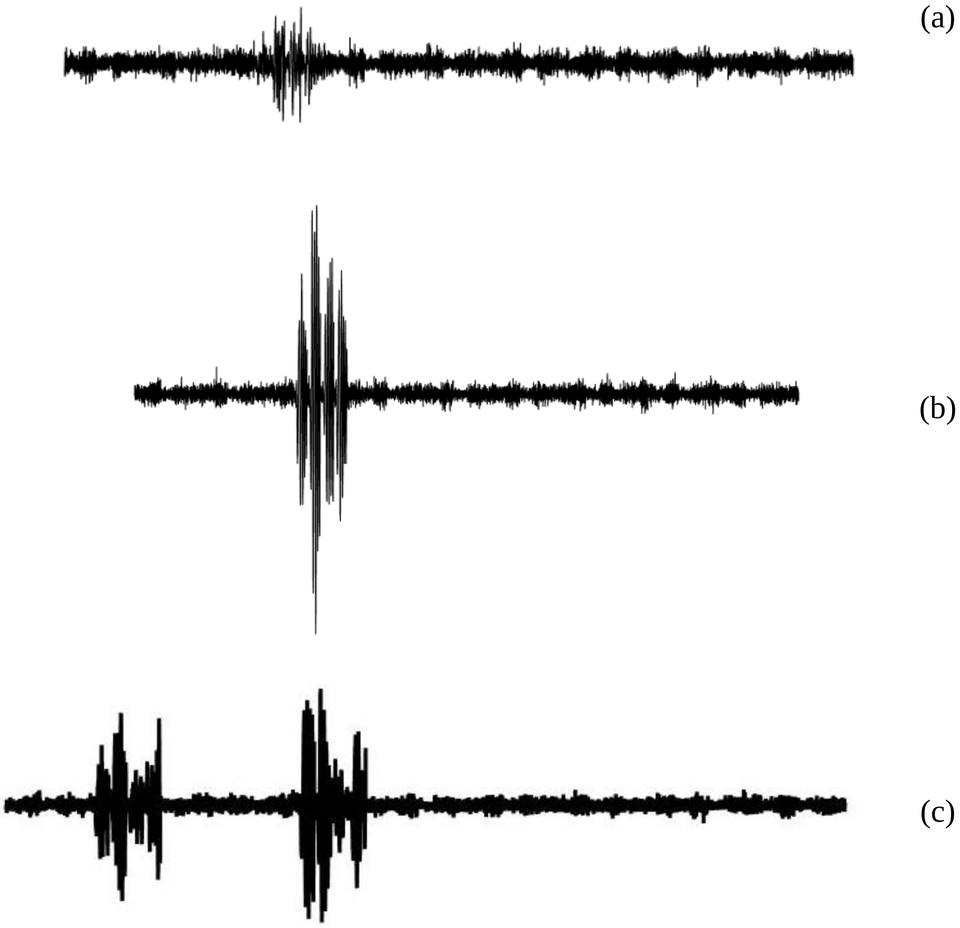

Figure 82: 2D CNN time domain residual signals input

As seen in Figure 82, the data set consists of residual images of the vibration signal. Figure 82. a depicts the residual signal of a damaged gear tooth with a CLP of 20% at the 7th tooth, whereas Figure 82. b depicts the residual signal of a damaged gear tooth with a CLP of 50% at the 5th tooth, and Figure 82. c depicts the residual signal of a damaged gear tooth with a CLP of 20% at the 3rd tooth and CLP of 30% at the 8th tooth.

Table 10: Results For 2D CNN With Residual Vibration Signal As Input, No. Samples Per Case = 75

Method	Validation Accuracy	Testing Accuracy	Average Precision	Average Recall
2D CNN	97.54	95.65	98.14	93.26

Table 11: Results For 2D CNN With Residual Vibration Signal As Input, No. Samples Per Case = 150

Method	Validation Accuracy	Testing Accuracy	Average Precision	Average Recall
2D CNN	98.34	97.77	99.02	94.45

As can be seen in Table 10, the number of input pictures is rather simple, which helps the accuracy of both the validation and testing sets, and the residual signal can be easily investigated and processed. In addition, as can be seen in Table 11, the accuracy increased as a result of the larger data set; however, overfitting was observed when more than 200 samples per case were used during training; as a result, the accuracy dropped significantly as seen in Table 12, and this is because a sample of 300 samples per case (190 cases) was used. The recall and precision values in the first two runs were fine, which indicates that the model is of high quality.

Table 12: Results For 2D CNN With Residual Vibration Signal As Input, No. Samples Per Case = 300

Method	Validation Accuracy	Testing Accuracy	Average Precision	Average Recall
2D CNN	68.294	57.0432	60.66	43.65

The best-recorded accuracy was for the case of 125 samples per case (191 cases), which is archived in Table 11

6.2.2 Time-Frequency Analysis Technique

Using the built-in spectrogram function in MATLAB, the frequency-time signal was obtained for the vibration signal of healthy and damaged gears, and then the mesh function created a mesh plot, which is a three-dimensional surface that has solid edge colors and no face colors the time-frequency signal was obtained as observed in Figure 83.

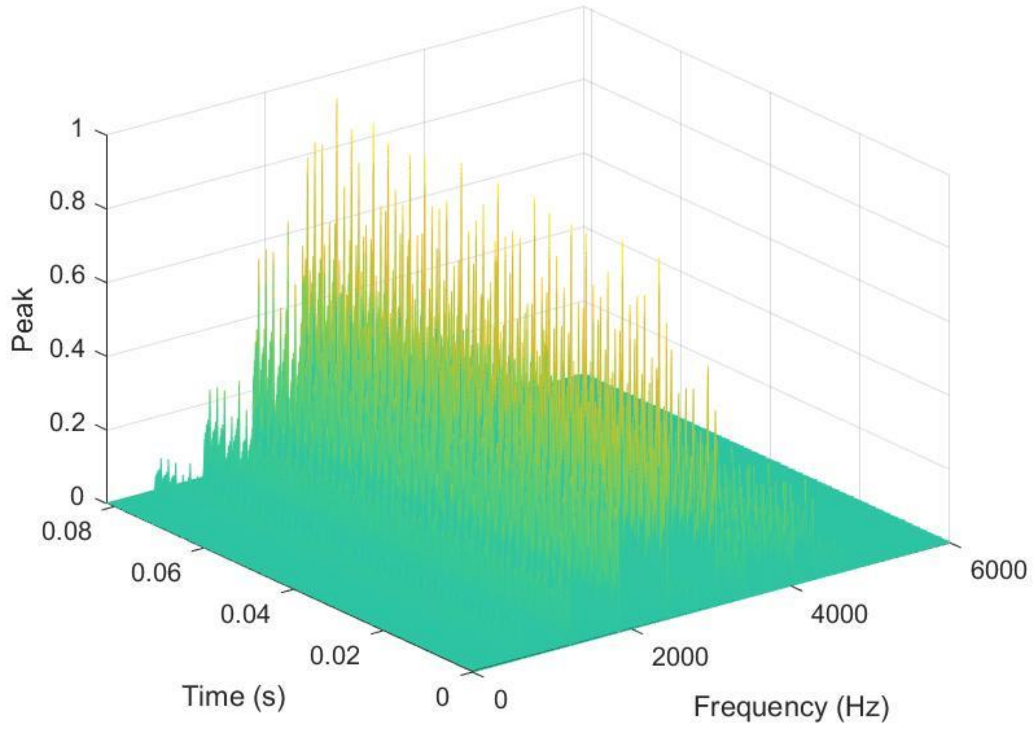

Figure 83: Frequency-Time 3D plot

The time and frequency domains may be obtained immediately from the 3D plot by modifying the view angle as observed in Figure 84 and Figure 85, implying that this is a useful way for analyzing vibration data that contains indications in both time and frequency domains, particularly in the case of gear problems.

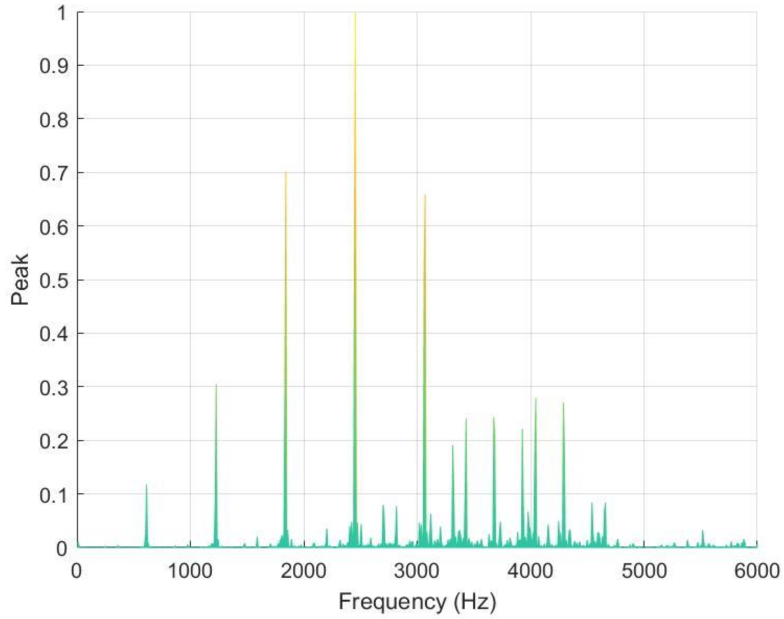

Figure 84: Frequency domain of vibration signal obtained from 3D spectrogram plot

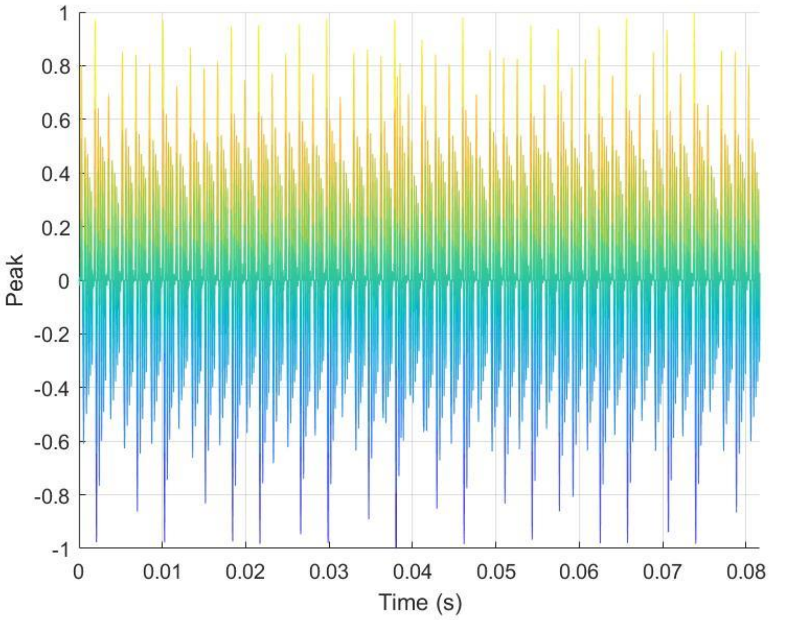

Figure 85: Time domain of vibration signal obtained from 3D spectrogram plot

Although this approach has good potential, implying it in this research seemed almost impossible as the computing power that this method requires is significant, as the computing machines used in this research aren’t of that level. The approach described previously is impossible to adopt with the current computational set-up for this research as image processing requires a much more powerful computer, so another approach was adopted by using image processing and frequency-time analysis.

The proposed Empirical mode Decomposition – Principal Component Analysis (EMD-PCA) technique integrates EMD, which adaptively decomposes signals into several time scales, with PCA, which offers a mechanism to extract informative features from a signal while simultaneously decreasing the number of variables that requires less computational power.

Non-stationary signals acquired from non-linear systems, as is common in actual systems that make use of rotary components, lend themselves well to analysis using the EMD method. In addition, it is well suited for the processing of signals with non-linear properties owing to its adaptive empirical nature. The first stage of the described method involves using the EMD algorithm to break down the vibration signal into the IMFs. In Figure 86, the extracted IMFs for a signal decomposition situation are seen, but the residual is not since it won't be used in the following phase. Each column in the matrix represents an individual IMF, and each row represents a discrete point in time. The residual is subtracted from this total. The subsequent PCA analysis makes use of this matrix. In the second stage, Principal Components Analysis (PCA) creates a new space to represent the IMFs matrix (PCs). The PCs computed from the IMFs shown in Figure 86 are displayed in Figure 87. A spectrogram is used to see each PC as a separate signal in the time-frequency plane. The spectrogram is recorded and then utilized to provide visual information about the computer. As can be seen in Figure 88, the time-frequency connection of the original signal may be shown by computing the spectrograms of all the PCs. Image data is often filtered to retain just that which may be used to distinguish between signals with varying defects. Since the method requires the same number of features for each observation and this research only obtains 9 PCs, the optimal number of PCs is determined by evaluating the accuracy throughout the whole dataset and selecting the same number of photos for each signal.

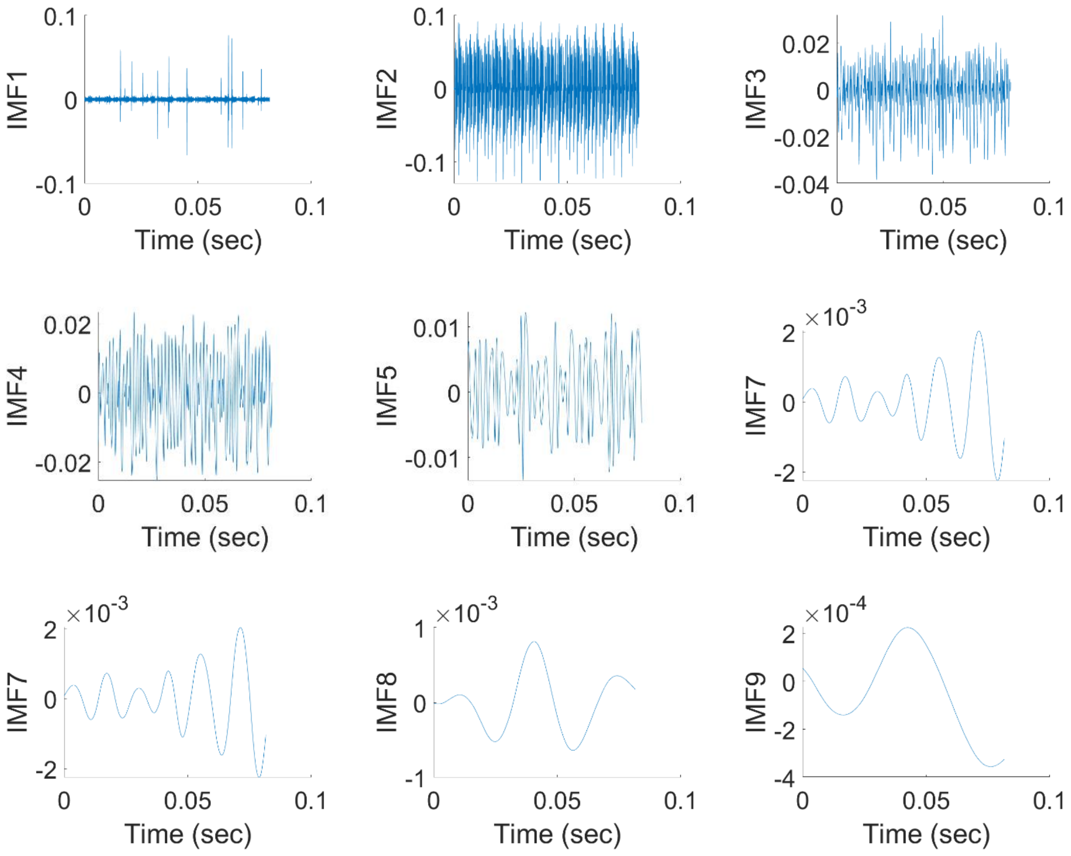

Figure 86: IMFs of gear vibration signal

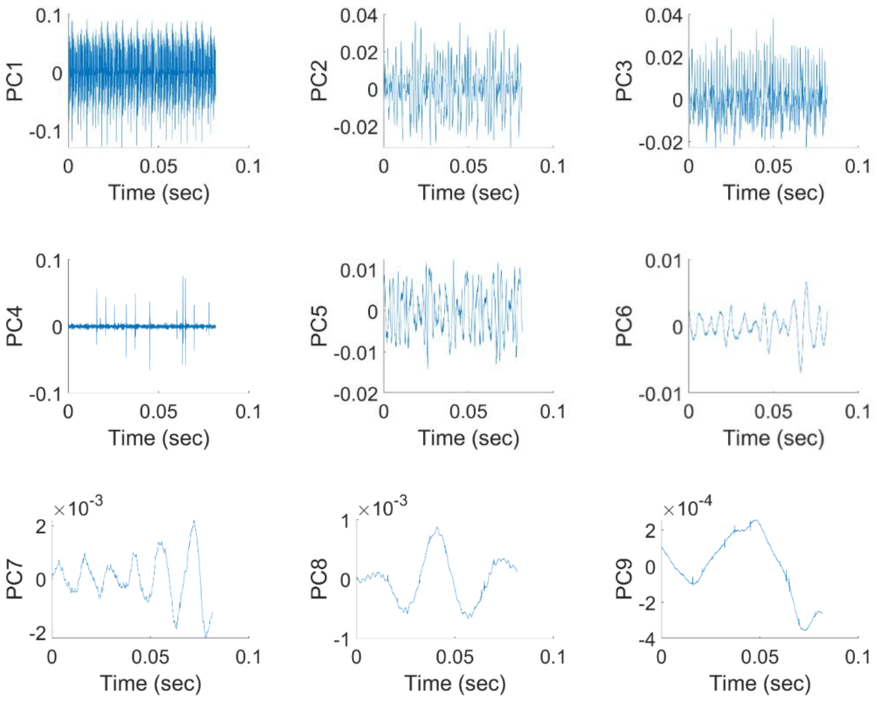

Figure 87: Principal components of IMFs after performing EMD on the vibration signal

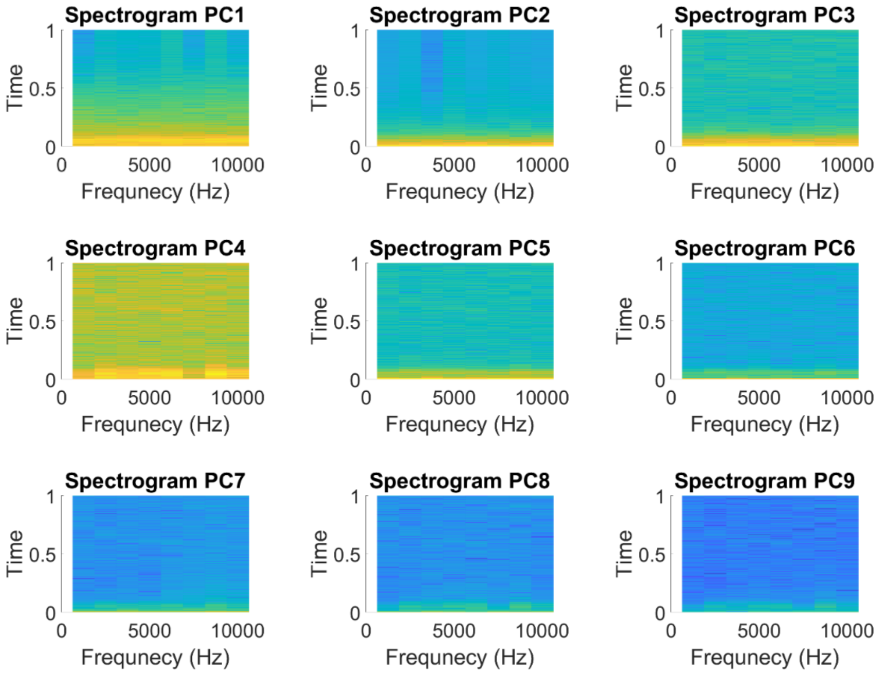

Figure 88: Spectrograms of the PCs

The spectrograms of the PCs are found for each sample and then fed to the model three times, once taking the first three, then the first six, and finally all the spectrograms to check the model's accuracy based on the number of given features. The overall data set consists of 41 unique cases, and only ten samples of each case are initially recorded, giving a total of 410 readings, each reading is composed of 9 images, and the images are kept in packages of 3,6, and 9. The model has the same characteristics as the previous algorithm. The model has then trained again after the validation with 150 samples for each case, and for the total number of possible cases, which is 191, again 70% is fed as training data, 30% as validating data, and testing data consist of 1000 data samples for the nine unique gears.

Table 13: Results Of The Pcs Spectrogram Multilabel Classification Using 2D CNN

Number of samples	Number of PCs		
	3	6	9
5	24.45	30.66	36.11
10	53.56	59.44	67.00
40	81.56	82.97	89.543
60	82.79	83.81	93.95
75	83.01	83.32	94.13
100	83.43	83.91	94.65

Testing Accuracy

As observed from Table 13, the number of samples plays a significant role in the accuracy of the results, as it was noticed that below ten samples per case, the accuracy is very low, but as the number of samples exceeds 50 per case, the accuracy starts to reach an acceptable level, but the increase starts to become lower till it reaches a constant state, as observed in Figure 89.

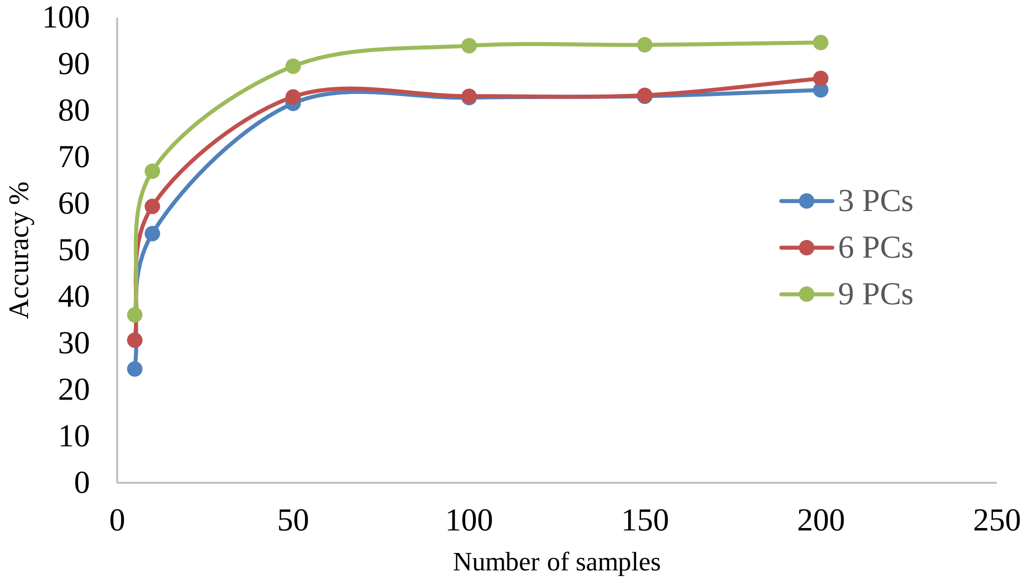

Figure 89: The growth of accuracy as a function of the total number of observations and the number of principal components

The accuracy of this strategy is promising since it is dependent on the number of PCs and the samples per case, which has been demonstrated to be extremely trustworthy, as this approach does not need a large number of samples to deliver excellent results, unlike previously explored ways that did.

Table 14: Overall Comparison Between All Approaches

Method	Type of data	Overall Testing Accuracy
1D CNN and LSTM	Time series [Raw / Residual]	93.084
2D CNN	Image [Vibration Residual]	97.77
2D CNN	Image processing [PCs Spectrogram]	94.65

Based on the accuracy values of the three different machine learning approaches that were

performed, the best accuracy is for the 2D CNN with residual vibration data, which is based on a robust data entry, where the time series vibration signal is entered in the residual form but in the shape of an image, which facilities the image processing and helps in giving a more accurate result, which was a test with experimental data, one reason behind the good accuracy could be the approach that was used to find the residual of the experimental vibration signal as it is an approximation and it takes a lot from the real-life signal and error.

CHAPTER 7: CONCLUSIONS AND FUTURE WORK

The key results from the construction of a real-life emulating dynamic gear set numerical model, employing friction-generated vibration, and the comparison of the two distinct machine learning algorithms explored are presented and addressed in this chapter. The research's future path was then addressed, and some extra study was recommended.

7.1 Conclusions

From the literature review of vibration feature-based gear wear monitoring, it was noticed that most existing research works focus on tracking the impulsive response generated from the periodic variation of gear-mesh stiffness. On the contrary, friction-induced vibration has received less attention mainly due to the domination of the impulsive response and to the low contribution of the noisy-based vibration in the presence of lubrication. In the presence of dry mechanisms or poor lubrication, the friction-induced vibration could not be ignored anymore.

This study investigated, both numerically and experimentally, the dynamic response of a spur gear set in the presence of an impulsive response generated from the periodic variation of gear-mesh stiffness and the friction-induced vibration generated from the mutual rubbing of mating teeth during their relative sliding and then a comparative examination of ML-based approaches for facility condition monitoring using the obtained dynamic response results are presented. First, the impulsive response was derived from a six-degree of freedom dynamic model, which comprehensively considers the existence of single cracks with different width values at the roots of one particular tooth. The contribution of friction-based vibration was then added to the impulsive main response to account for the rubbing of teeth on each other. Three different forms of noisy friction-based vibration were considered: constant amplitude normalized noise, modulated amplitude noise, and a combination of both of them. The modulation was retrieved by analyzing the variation of curvature radii and the area of elastic deformation by utilizing Hertz's theory of contact. The efficacy of the present approach is demonstrated by a comparison with experimental results collected from a test rig specially developed for this purpose.

Based on the present investigation, the usefulness of adding friction-based noisy vibration to the impulsive periodic component was confirmed. Such a noisy component was considered a combination of constant amplitude noise and modulated amplitude noise. The modulation effect was created by the continuous variation of the curvature radii of both mating teeth and the elastic deformation area at the running points of contact. Such proven modulation has confirmed the cyclization behavior of gears' dynamics. Furthermore, by validating the numerical model with the experimental set-up, a real-life data-generating algorithm was produced, which acts as a data mining model for machine learning algorithms. The model was then used to generate numerous types of data, varying from time domain signal to color-mapped graphs, which then were implemented along with the experimental data in 2 different ML approaches. The first one is based on time series sequential vibration data, and it combines the standard 1-D CNN with an LSTM network in order to do multilabel classification. This method was chosen since it is applicable to the sort of data that is being input. When it comes to processing vibration signals, the CNN is utilized, while the LSTM network is used to handle residual data. Both of these networks are described below. In this scenario, the results from the CNN and the LSTM network will be integrated into a single set of results. The time domain residual signal pictures and spectrograms of principle components are used in the second method, which is known as image processing in 2D CNN multi-label image classification. In contrast to conventional fully connected neural networks, CNNs drastically reduce network parameters via local connection and the exchange of weights in convolutional layers, which are made up of a collection of kernels with a restricted receptive field. Furthermore, in order to get a sufficient generalization capability, training deep 2D CNNs with sequential data necessitates prolonged training. As a result, the computing complexity is usually rather high, especially when dealing with large-scale datasets. As a result, gear tooth crack defects may be diagnosed using a method that is based on one-dimensional CNN and LSTM. This combination of 1D convolutional neural networks and recurrent neural networks was developed with the goal of overcoming these drawbacks while also obtaining better levels of accuracy and more computing efficiency on 1D data. The findings demonstrated that the provided technique had greater diagnostic accuracy for gear fracture problems when compared with CNN or LSTM network alone. This was determined by comparing the networks to themselves. In addition, the approach may reach an accuracy of more than 93.664% with just a limited number of training samples, which is evidence that the method that has been provided is successful. Additionally, the results showed great performance by the adopted combined method compared to traditional separate models, and it showed good computing time and power

Nevertheless, the novel residual vibration signal 2D CNN image processing for defected spur gear cracks diagnosis showed a decrease in complexity and network depth required by 2DD CNNs in many challenging problems. In addition, by proposing the EMD-PCA method, the demanding 3D image processing of the frequency-time domain plot issue was solved by the provided novel approach that creates a time-frequency representation of vibration signals by using Empirical Mode Decomposition and Principal Component Analysis. This technique is based on the analysis of pictures of spectrograms, and it was developed recently. A method that is based on 2D CNN image processing is utilized for the classification, and the image moments are extracted from the spectrograms and used as features for the algorithm. The approach that has been provided is adaptable to a wide variety of rotational speeds and load situations. The created approach has been successful, producing accurate findings 94.65% of the time. Finally, by making use of both novel outcomes of this research robust trained system was developed, which could be used in an actual health monitoring environment.

7.2 Future Work

The following suggestions are proposed as future work for this research, which may corroborate the given results while also adding to this knowledge field of gear tooth crack detection through machine learning techniques:

- Studying the effect of having two defective spur gears (one or multiple cracks on each gear).
- Studying the breathing phenomenon of gear cracks, where the force applied on the gear tooth is in the opposite direction of the crack propagation.
- Developing an IoT network that could integrate the condition monitoring data recording with the trained machine learning model.
- Studying other input data from the experimental set-up, such as sound and current signals to improve the machine-learning models.

REFERENCES

[1] Maitra, G. M. (1994). *Handbook of gear design*. Tata McGraw-Hill Education.

[2] A. Belsak and J. Flasker, "Detecting cracks in the tooth root of gears," Engineering Failure Analysis, vol. 14, pp. 1466-1475, 2007.

[3] P. J. L. Fernandes, "Tooth bending fatigue failures in gears," Engineering Failure Analysis, vol. 3, pp. 219-225, 1996.

[4] S. Pehan, J. Kramberger, J. Flašker, and B. Zafošnik, "Investigation of crack propagation scatter in a gear tooth's root," Engineering Fracture Mechanics, vol. 75, pp. 1266-1283, 2008.

[5] C. Hu, W. A. Smith, R. B. Randall, and Z. Peng, "Development of a gear vibration indicator and its application in gear wear monitoring," Mechanical Systems and Signal Processing, 2016.

[6] H. J. Decker, J. M. Certo, R. F. Handschuh, and T. L. Krantz, "Development of a new single gear tooth bending fatigue test capability," in 62nd American Helicopter Society International Annual Forum Phoenix, AZ, 2006, pp. 704-707.

[7] K. M. Satoshi ODA, Takao KOIDE Toshiaki Fuji, "Dynamic Behavior of Thinrimmed Spur Gear with Various Web Arrangements," Bulletin of JSME, vol. 29, pp. 247-235, 1986.

[8] S. Li, "Effect of addendum on contact strength, bending strength and basic performance parameters of a pair of spur gears," Mechanism and Machine Theory, vol. 43, pp. 1557-1584, 2008.

[9] G. Marunić, "Effects of rim and web thickness on gear tooth root, rim and web stresses," in Key Engineering Materials vol. 385-387, ed, 2008, pp. 117-120.

[10] E. E. Shipley, "Gear Failure," in Machine Design, ed Cleveland, Ohio: The Penton

Publishing co., 1967.

[11] S. Glodež, S. Pehan, and J. Flašker, "Experimental results of the fatigue crack growth in a gear tooth root," International Journal of Fatigue, vol. 20, pp. 669-675, 1998.

[12] J. Kramberger, M. Šraml, I. Potrč, and J. Flašker, "Numerical calculation of bending fatigue life of thin-rim spur gears," Engineering Fracture Mechanics, vol. 71, pp. 647- 656, 2004

[13] Aziz, I. A. A., Idris, D. M. N. D., & Ghazali, W. M. (2017). Investigating bending strength of spur gear: A review. In *MATEC web of conferences* (Vol. 90, p. 01037). EDP Sciences.

[14] Q. J. Yang, "Fatigue test and reliability design of gears," International Journal of Fatigue, vol. 18, pp. 171-177, 1996.

[15] Pimsarn, M., Kazerounian, K., 2002. Efficient evaluation of spur gear tooth mesh load using pseudo-interference stiffness estimation method. Mech. Mach. Th. 37, 769–786.

[16] Wang, J., 2003. Numerical and experimental analysis of spur gears in mesh. PhD, Curtin University of Technology.

[17] Sirichai, S., 1999. Torsional properties of spur gears in mesh using nonlinear finite element analysis. PhD, Curtin: University of Technology.

[18] Weber, C., 1949. The deformation of loaded gears and the effect on their loadcarrying capacity. Sponsored research (Germany). British Dept. of Sci. and Ind. Res. Report No. 3.

[19] Ruxton, K., Chakraborty, A. L., Johnstone, W., Lengden, M., Stewart, G., & Duffin, K. (2010). Tunable diode laser spectroscopy with wavelength modulation eliminates residual amplitude modulation in a phasor decomposition approach. Sensors

and Actuators B: Chemical, 150(1), 367-375.

[20] Mohanty, S. C. (2003). Tooth load sharing and contact stress analysis of high contact ratio spur gears in mesh. Journal of the Institution of Engineers(India), Part MC, Mechanical Engineering Division, 84, 66-70.

[21] Sainsot and, P., Velex, P., & Duverger, O. (2004). Contribution of gear body to tooth deflections—a new bidimensional analytical formula. J. Mech. Des., 126(4), 748-752.

[22] Attia, Y., 1963. Deflection of spur gear teeth cut in thin rims. ASME paper 63-WA-14, 1963.

[23] Cornell, R.W., 1981. Compliance and stress sensitivity of spur gear teeth. ASME J. Mech. Des. 103, 447–459

[24] Huang, N. E., Shen, Z., Long, S. R., Wu, M. C., Shih, H. H., Zheng, Q., ... & Liu, H. H. (1998). The empirical mode decomposition and the Hilbert spectrum for nonlinear and non-stationary time series analysis. Proceedings of the Royal Society of London. Series A: mathematical, physical and engineering sciences, 454(1971), 903-995.

[25] Hotelling, H. (1933). Analysis of a complex of statistical variables into principal components. Journal of educational psychology, 24(6), 417.

[26] M. Hamadache, J. H. Jung, J. Park, and B. D. Youn, “A comprehensive review of artificial intelligence-based approaches for rolling element bearing PHM: shallow and deep learning,” JMST Adv., vol. 1, no. 1, pp. 125–151, Jun. 2019, doi: 10.1007/s42791-019-0016.

[27] Hüsken, M., & Stagge, P. (2003). Recurrent neural networks for time series classification. Neurocomputing, 50, 223-235.

[28] X. Chen, F. Kopsaftopoulos, Q. Wu, H. Ren, and F.-K. Chang, “A Self-Adaptive

1D Convolutional Neural Network for Flight-State Identification," Sensors, vol. 19, no. 2, Art. no. 2, Jan. 2019, doi: 10.3390/s19020275.

[29] O'Shea, K., & Nash, R. (2015). An introduction to convolutional neural networks. arXiv preprint arXiv:1511.08458.

[30] Gulli A, Pal S. Deep learning with Keras. Packt Publishing Ltd; 2017.

[31] Wu, H., & Prasad, S. (2017). Convolutional recurrent neural networks for hyperspectral data classification. Remote Sensing, 9(3), 298.

[32] Simão, M., Neto, P., & Gibaru, O. (2019). EMG-based online classification of gestures with recurrent neural networks. Pattern Recognition Letters, 128, 45-51.

[33] Wu, X. (2004, September). Data mining: artificial intelligence in data analysis. In Proceedings. IEEE/WIC/ACM International Conference on Intelligent Agent Technology (IAT 2004) (pp. 7-7). IEEE Computer Society.

[34] Parey, A., & Tandon, N. (2010). Fault detection of spur gears using vibration monitoring. *Lambert, Saarbrucken, Germany*.

[35] Mohammed, O. D. (2015). *Dynamic modelling and vibration analysis for gear tooth crack detection* (Doctoral dissertation, Luleå tekniska universitet).

[36] Randall, R. B. (2021). *Vibration-based condition monitoring: industrial, automotive and aerospace applications*. John Wiley & Sons.

[37] Samuel, P. D., & Pines, D. J. (2005). A review of vibration-based techniques for helicopter transmission diagnostics. *Journal of sound and vibration*, *282*(1-2), 475-508.

[38] Jardine, A. K., Lin, D., & Banjevic, D. (2006). A review on machinery diagnostics and prognostics implementing condition-based maintenance. *Mechanical systems and signal processing*, *20*(7), 1483-1510.

[39] Barszcz, T., & Randall, R. B. (2009). Application of spectral kurtosis for detection

of a tooth crack in the planetary gear of a wind turbine. *Mechanical systems and signal processing*, *23*(4), 1352-1365.

[40] Wang, W. (2001). Early detection of gear tooth cracking using the resonance demodulation technique. *Mechanical Systems and Signal Processing*, *15*(5), 887-903.

[41] Assaad, B., Eltabach, M., & Antoni, J. (2014). Vibration based condition monitoring of a multistage epicyclic gearbox in lifting cranes. *Mechanical Systems and Signal Processing*, *42*(1-2), 351-367.

[42] Ricci, R., & Pennacchi, P. (2011). Diagnostics of gear faults based on EMD and automatic selection of intrinsic mode functions. *Mechanical Systems and Signal Processing*, *25*(3), 821-838.

[43] Sawalhi, N., & Randall, R. B. (2014). Gear parameter identification in a wind turbine gearbox using vibration signals. *Mechanical Systems and Signal Processing*, *42*(1-2), 368-376.

[44] Mohammed, O. D., & Rantatalo, M. (2020). Gear fault models and dynamics-based modelling for gear fault detection–A review. *Engineering Failure Analysis*, *117*, 104798.

[45] Liang, X., Zuo, M. J., & Feng, Z. (2018). Dynamic modeling of gearbox faults: A review. *Mechanical Systems and Signal Processing*, *98*, 852-876.

[46] Chaari, F., Bartelmus, W., Zimroz, R., Fakhfakh, T., & Haddar, M. (2012). Gearbox vibration signal amplitude and frequency modulation. *Shock and Vibration*, *19*(4), 635-652.

[47] Randall, R. B. (1982). A new method of modeling gear faults.

[48] McFadden, P. D., & Smith, J. D. (1985). An explanation for the asymmetry of the modulation sidebands about the tooth meshing frequency in epicyclic gear vibration. *Proceedings of the Institution of Mechanical Engineers, Part C: Journal of*

Mechanical Engineering Science, *199*(1), 65-70.

[49] McFadden, P. D. (1986). Detecting fatigue cracks in gears by amplitude and phase demodulation of the meshing vibration.

[50] Inalpolat, M., & Kahraman, A. (2009). A theoretical and experimental investigation of modulation sidebands of planetary gear sets. *Journal of sound and vibration*, *323*(3-5), 677-696.

[51] Feng, Z., & Zuo, M. J. (2012). Vibration signal models for fault diagnosis of planetary gearboxes. *Journal of Sound and Vibration*, *331*(22), 4919-4939.

[52] Patrick, R., Ferri, A., & Vachtsevanos, G. (2012). Effect of planetary gear carrier-plate cracks on vibration spectrum. *Journal of vibration and acoustics*, *134*(6).

[52] Bartelmus, W. (2001). Mathematical modelling and computer simulations as an aid to gearbox diagnostics. *Mechanical Systems and Signal Processing*, *15*(5), 855-871.

[53] Parey, A., & Tandon, N. (2003). Spur gear dynamic models including defects: A review. *The Shock and Vibration Digest*, *35*(6), 465-478.

[54] El Badaoui, M., Cahouet, V., Guillet, F., Daniere, J., & Velex, P. (2001). Modeling and detection of localized tooth defects in geared systems. *J. Mech. Des.*, *123*(3), 422-430.

[55] Parey, A., El Badaoui, M., Guillet, F., & Tandon, N. (2006). Dynamic modelling of spur gear pair and application of empirical mode decomposition-based statistical analysis for early detection of localized tooth defect. *Journal of sound and vibration*, *294*(3), 547-561.

[56] Tian, X. (2004). Dynamic simulation for system response of gearbox including localized gear faults.

[57] Wu, S., Zuo, M. J., & Parey, A. (2008). Simulation of spur gear dynamics and estimation of fault growth. *Journal of Sound and Vibration*, *317*(3-5), 608-624.

[58] Chen, Z., & Shao, Y. (2011). Dynamic simulation of spur gear with tooth root crack propagating along tooth width and crack depth. *Engineering failure analysis*, *18*(8), 2149-2164.

[59] Siyu, C., Jinyuan, T., Caiwang, L., & Qibo, W. (2011). Nonlinear dynamic characteristics of geared rotor bearing systems with dynamic backlash and friction. *Mechanism and machine theory*, *46*(4), 466-478.

[60] He, S., Cho, S., & Singh, R. (2008). Prediction of dynamic friction forces in spur gears using alternate sliding friction formulations. *Journal of Sound and Vibration*, *309*(3-5), 843-851.

[61] He, S., Gunda, R., & Singh, R. (2007). Effect of sliding friction on the dynamics of spur gear pair with realistic time-varying stiffness. *Journal of Sound and Vibration*, *301*(3-5), 927-949.

[62] Howard, I., Jia, S., & Wang, J. (2001). The dynamic modelling of a spur gear in mesh including friction and a crack. *Mechanical systems and signal processing*, *15*(5), 831-853.

[63] Zhou, X., Shao, Y., Lei, Y., & Zuo, M. (2012). Time-varying meshing stiffness calculation and vibration analysis for a 16DOF dynamic model with linear crack growth in a pinion. *Journal of Vibration and Acoustics*, *134*(1).

[64] Mohammed, O. D., Rantatalo, M., & Aidanpää, J. O. (2015). Dynamic modelling of a one-stage spur gear system and vibration-based tooth crack detection analysis. *Mechanical Systems and Signal Processing*, *54*, 293-305.

[65] Mohammed, O. D., Rantatalo, M., & Aidanpää, J. O. (2015). Dynamic modelling of gear system with gyroscopic effect and crack detection analysis. In *Proceedings of the 9th IFToMM International Conference on Rotor Dynamics* (pp. 1303-1314). Springer, Cham.

[66] Yuksel, C., & Kahraman, A. (2004). Dynamic tooth loads of planetary gear sets having tooth profile wear. *Mechanism and Machine Theory*, *39*(7), 695-715.

[67] Ding, H. (2007). Dynamic wear models for gear systems. ProQuest.

[68] Parker, R. G., Agashe, V., & Vijayakar, S. M. (2000). Dynamic response of a planetary gear system using a finite element/contact mechanics model. J. Mech. Des., 122(3), 304-310.

[69] Tamminana, V. K., Kahraman, A., & Vijayakar, S. (2007). A study of the relationship between the dynamic factors and the dynamic transmission error of spur gear pairs.

[70] Parker, R. G., Vijayakar, S. M., & Imajo, T. (2000). Non-linear dynamic response of a spur gear pair: modelling and experimental comparisons. *Journal of Sound and vibration*, *237*(3), 435-455.

[71] Liang, X., Zuo, M. J., Feng, Z., & Liu, L. (2016, October). A mesh stiffness evaluation model to reflect tooth pitting growth of a pair of external spur gears. In *2016 Prognostics and System Health Management Conference (PHM-Chengdu)* (pp. 1-6). IEEE.

[72] Mohamed, A., Sassi, S., & Paurobally, M. R. (2017). Numerical simulation of one-stage gearbox dynamics in the presence of simultaneous tooth crack. *Proceedings of the ICSV24*.

[73] Mohamed, A. S., Sassi, S., & Roshun Paurobally, M. (2018). Model-based analysis of spur gears' dynamic behavior in the presence of multiple cracks. *Shock and Vibration*, *2018*.

[74] Chen, Z., Zhai, W., Shao, Y., Wang, K., & Sun, G. (2016). Analytical model for mesh stiffness calculation of spur gear pair with non-uniformly distributed tooth root crack. *Engineering Failure Analysis*, *66*, 502-514.

[75] Wu, S. (2007). *Gearbox Dynamic Simulation and Estimation of Fault* (Doctoral dissertation, University of Alberta).

[76] Chen ZG, Shao YM. Dynamic simulation of spur gear with tooth root crack propagating along tooth width and crack depth. Eng Fail Anal 2011; 18:2149–64.

[77] Loutridis SJ. Damage detection in gear systems using empirical mode decomposition. Eng Struct 2004; 26:1833–41.

[78] Forrester BD. Analysis of gear vibration in the time-frequency domain. In: Proceedings of the 44th meeting of mechanical failures prevention group of the vibration institute, Virginia Beach, VA; 3–5 April, 1989.

[79] Allgood G. Detection of gear wear on the 757/767 internal drive generator using higher order statistics and wavelets. In: 15th International modalanalysis conference, Florida; 1997.

[80] Huang NE, Shen Z, Long SR, et al. The empirical mode decomposition and Hilbert spectrum for nonlinear and nonstationary time series analysis. Proc R Soc London Ser 1998; 454:903–95.

[81] Loutridis S. Instantaneous energy density as a feature for gear fault detection. Mech Syst Signal Process 2006; 20:1239–53.

[82] S. Vijayarangan and N. Ganesan, "Static contact stress analysis of a spur gear tooth using the finite element method, including frictional effects," Computers and Structures, vol. 51, no. 6, pp. 765–770, 1994.

[83] B. Rebbechi, F. B. Oswald, and D. P. Townsend, Measurement of Gear Tooth Dynamic Friction, vol. 88, American Society of Mechanical Engineers, Design Engineering Division, 1996.

[84] P. Velex and P. Sainsot, "An analytical study of tooth friction excitations in errorless spur and helical gears," Mechanism and Machine Theory, vol. 37, no. 7, pp.

641–658, 2002.

[85] A. Mihalidis, V. Bakolas, K. Panagiotidis, and N. Drivakos, “Prediction of the friction coefficient of spur gear pairs,” VDI Berichte, vol. 2, no. 1665, pp. 705–719, 2002.

[86] S. Kim and R. Singh, “Gear surface roughness induced noise prediction based on a linear time-varying model with sliding friction,” JVC/Journal of Vibration and Control, vol. 13, no. 7, pp. 1045–1063, 2007.

[87] S. He, R. Gunda, and R. Singh, “Inclusion of sliding friction in contact dynamics model for helical gears,” Journal of Mechanical Design, vol. 129, no. 1, pp. 48–57, 2007.

[88] Fan Y, Fengshou G, Ball A. Modelling acoustic emissions generated by sliding friction. Wear 2010; 268:811–5.

[89] Kanakarajan P, Sundaram S, Kumaravel A, Rajasekar R, Kumar PS. Acoustic emission testing of surface roughness and wear caused by grinding of ceramic materials. Materials Testing 2015; 57:337–42.

[90] Amarnath M, Lee SK. Assessment of surface contact fatigue failure in a spur geared system based on the tribological and vibration parameter analysis. Measurement 2015;76:32–44. http://dx.doi.org/10.1016/j.measurement.2015.08.020 .

[91] Eftekharnejad B, Carrasco MR, Charnley B, Mba D. The application of spectral kurtosis on Acoustic Emission and vibrations from a defective bearing. Mech Syst Signal Process 2011; 25(1):266–84. https://doi.org/10.1016/j.ymssp.2010.06.010 .

[92] Hamel M, Addali A, Mba D. Investigation of the influence of oil film thickness on helical gear defect detection using Acoustic Emission. Appl Acoust 2014; 79:42–6.

[93] McFadden, P. D. (1987). Examination of a technique for the early detection of failure in gears by signal processing of the time domain average of the meshing

vibration. *Mechanical systems and signal processing*, *1*(2), 173-183.

[94] O. D. Mohammed, M. Rantatalo, J. O. Aidanpää, and U. Kumar, “Vibration signal analysis for gear fault diagnosis with various crack progression 132 scenarios,” Mech. Syst. Signal Process., vol. 41, no. 1–2, pp. 176–195, 2013.

[95] Pachaud C, Salvetat R, Fray C (1997) Crest factor and kurtosis contributions to identify defects inducing periodical impulsive forces. Mech Syst Signal Process 11(6):903–916

[96] Boulenger A, Pachaud C (1998) Diagnostic vibratoire en maintenance préventive. Dunod, Paris.

[97] Z. Qiao, Y. Lei, and N. Li, “Applications of stochastic resonance to machinery fault detection: A review and tutorial,” Mech. Syst. Signal Process., vol. 122, pp. 502–536, May 2019, doi: 10.1016/j.ymssp.2018.12.032.

[98] P. Cao, S. Zhang, and J. Tang, “Preprocessing-Free Gear Fault Diagnosis Using Small Datasets With Deep Convolutional Neural Network-Based Transfer Learning,” IEEE Access, vol. 6, pp. 26241–26253, 2018, doi: 10.1109/ACCESS.2018.2837621.

[99] F. Li, X. Pang, and Z. Yang, “Motor current signal analysis using deep neural networks for planetary gear fault diagnosis,” Measurement, vol. 145, pp. 45–54, Oct. 2019, doi: 10.1016/j.measurement.2019.05.074.

[100] X. Li, J. Li, D. He, and Y. Qu, “Gear pitting fault diagnosis using raw acoustic 64 emission signal based on deep learning,” Eksploat. Niezawodn., vol. Vol. 21, no. 3, 2019, doi: 10.17531/ein.2019.3.6.

[101] X. Li, J. Li, Y. Qu, and D. He, “Semi-supervised gear fault diagnosis using raw vibration signal based on deep learning,” Chin. J. Aeronaut., vol. 33, no. 2, pp. 418–426, Feb. 2020, doi: 10.1016/j.cja.2019.04.018.

[102] G. Cirrincione, R. R. Kumar, A. Mohammadi, S. H. Kia, P. Barbiero, and J. Ferretti, “Shallow Versus Deep Neural Networks in Gear Fault Diagnosis,” IEEE Trans. Energy Convers., vol. 35, no. 3, pp. 1338–1347, Sep. 2020, doi: 10.1109/TEC.2020.2978155.

[103] Z. K. Abdul, A. K. Al-Talabani, and D. O. Ramadan, “A Hybrid Temporal Feature for Gear Fault Diagnosis Using the Long Short Term Memory,” IEEE Sens. J., vol. 20, no. 23, pp. 14444–14452, Dec. 2020, doi: 10.1109/JSEN.2020.3007262.

[104] Y. Qu, M. He, J. Deutsch, and D. He, “Detection of Pitting in Gears Using a Deep Sparse Autoencoder,” Appl. Sci., vol. 7, no. 5, Art. no. 5, May 2017, doi: 10.3390/app7050515.

[105] X. Wang, D. Mao, and X. Li, “Bearing fault diagnosis based on vibro-acoustic data fusion and 1D-CNN network,” Measurement, vol. 173, p. 108518, Mar. 2021, doi: 10.1016/j.measurement.2020.108518.

[106] X. Li, J. Li, C. Zhao, Y. Qu, and D. He, “Gear pitting fault diagnosis with mixed operating conditions based on adaptive 1D separable convolution with residual connection,” Mechanical Systems and Signal Processing, vol. 142, p. 106740, Aug. 2020, doi: 10.1016/j.ymssp.2020.106740.

[107] Y. Yao et al., “End-To-End Convolutional Neural Network Model for Gear Fault Diagnosis Based on Sound Signals,” Appl. Sci., vol. 8, no. 9, Art. no. 9, Sep. 2018, doi: 10.3390/app8091584.

[108] Dadon, I., Koren, N., Klein, R., & Bortman, J. (2018). A realistic dynamic model for gear fault diagnosis. *Engineering Failure Analysis, 84,* 77-100.

[109] Chen, Z., Shao, Y., & Su, D. (2013). Dynamic simulation of planetary gear set with flexible spur ring gear. *Journal of sound and vibration*, *332*(26), 7191-7204.

[110] Yu, W. (2017). *Dynamic modelling of gear transmission systems with and*

without localized tooth defects (Doctoral dissertation, Queen's University (Canada)).

[111] Barnov, V. M., Kudryavstev, E. M., and Sarychev, G. A., 1997, "Modelling of the parameters of acoustic emission under sliding friction of solids," Journal of Wear 202(2), 125–133.

[112] Retrieved from: https://www.iso.org/standard/63819.html.

[113] He, Y., Hernandez, I. D., Vaz, M. A., & Caire, M. (2020). Estimation of flexible riser curvature distribution and bend stiffener polyurethane behavior using the Levenberg-Marquardt algorithm in full scale bending-tension tests. Ocean Engineering, 216, 108018.

[114] Chen, X., Kopsaftopoulos, F., Wu, Q., Ren, H., & Chang, F. K. (2019). A self-adaptive 1D convolutional neural network for flight-state identification. Sensors, 19(2), 275.

[115] Abdeljaber, O., Sassi, S., Avci, O., Kiranyaz, S., Ibrahim, A. A., & Gabbouj, M. (2018). Fault detection and severity identification of ball bearings by online condition monitoring. IEEE Transactions on Industrial Electronics, 66(10), 8136-8147.

[116] Yesilyurt, I., Gu, F., Adrew, D.B., 2003. Gear tooth stiffness reduction measurement using modal analysis and its use in wear fault severity assessment of spur gear. Nondestructive Testing and Evaluation International 36, 357–372.